Lancaster University

Type-II GaSb/GaAs Quantum Ring Intermediate Band Solar Cell

Denise Montesdeoca Cárdenes

Supervisor: Prof. Anthony Krier

Co-supervisor: Dr. Peter James Carrington

A thesis presented for the degree of Doctor of Philosophy (PhD)

April 2019

NELSON MANDELA UNIVERSITY

Tyndall National Institute

UNIVERSITY OF SURREY

POLITÉCNICA Instituto de Energía Solar

PROMIS

A Marie Skłodowska-Curie Initial Training Network

Postgraduate Research on Dilute Metamorphic Nanostructures and Metamaterials in Semiconductor Photonics

MARIE CURIE ACTIONS

Declaration of authorship

I declare that the contents of this thesis, titled '*Type-II GaSb/GaAs Quantum Ring Intermediate Band Solar Cell'*, are the result of my own independent work. Where I have consulted the published work of others this is acknowledged by explicit references. I confirm that this work has not been submitted in whole or in any part for any other degree or qualification at this university or at any other academic institution.

Denise Montesdeoca Cárdenes

April 2019

Type-II GaSb/GaAs Quantum Ring

Intermediate Band Solar Cell

Denise Montesdeoca Cárdenes

April 2019

Abstract

There is considerable interest in the development of high efficiency cost-effective solar cells for renewable energy generation. Multi-junction cells based on III-V compound semiconductors currently hold a strong position because they are well suited to solar concentrator systems. However, high efficiency can be also be achieved by exploiting two photon photocurrent relying on the *intermediate band* concept. This thesis reports on an in-depth investigation of solar cells containing type-II GaSb/GaAs quantum ring (QR) nanostructures, systematically studying their electrical and optical performance under different test conditions. The aim is to understand the potential and limitations of this system, working as an intermediate band solar cell (IBSC), towards improving the efficiency of the conventional GaAs single junction solar cell. Two different approaches were developed and investigated to enhance solar cell performance; (i) increasing the number of QR layers and (ii) decreasing the overall thickness of the QR stack.

High density stacks of type-II GaSb/GaAs QR of high crystalline quality were successfully grown and characterized as QRSC for the first time. The stacks consisted of up to 40 QR layers with a linear density of 0.17 nm^{-1} along the growth direction, which is the highest reported to date for a type-II IBSC. By increasing the number of QR layers from 10 to 40, both the efficiency and the electroluminescence of the WL and QR transitions were enhanced by a factor of 4. Electroluminescence and open-circuit

voltage (V_{OC}) reciprocity was demonstrated experimentally, showing that QR radiative recombination limits V_{OC}. Hole transport through the intrinsic region of the cell was improved by decreasing the QR stack thickness from 400 to 60 nm, which resulted in an enhancement of 15% in short-circuit current and 30% in conversion efficiency. However, the open-circuit voltage drops when adding QR to the GaAs matrix preventing high efficiency from being obtained.

Two-photon photocurrent was studied in type-II QRSC using two-colour spectroscopy at 17 K and trapping was identified as the mechanism controlling QR (hole) charging. Above 100 K thermionic emission of holes was found to dominate QR discharging over optical emission. The non-radiative and radiative decay times of the QR were measured for first time at 10 K to be 10-100 ns, equivalent to rates of 10^{8}-10^{7} s^{-1}, under a peak flux of 10^{17} $cm^{-2}s^{-1}$. As illumination increases SRH is overtaken by radiative band-to-band recombination in high density QR stack SC. Partial V_{OC} recovery (up to 56%) under high solar concentration of 4000 suns was demonstrated in type-II QRSC at room temperature, analysing current versus voltage characteristic for first time. Full recovery of V_{OC} is prevented by the thermal coupling between the QR intermediate band and the valence band. In addition, hydrostatic pressure was applied to IBSC for the first time, to characterize type-II GaSb/GaAs QRSC. Under 8 kbar at room temperature the bandgap increased by 100 meV without modifying the carrier thermal energy and resulting in a V_{OC} increase of 15%.

En realidad competimos con nosotr@s mism@s, nosotr@s no tenenem@s control sobre el rendimiento de otr@s.

Peter Cashmor

Acknowledgements

I would like to begin with the funding source, the PROMIS project funded by EU Horizon 2020 Marie Sklodowska-Curie Actions, giving thanks to the director of the project as well as to all the professors that took part in it.

I want to thank everybody that has contributed to my research output. Thanks to my supervisor Prof. Anthony Krier for his support and his long lasting patience, even when everything seemed to not be working he always knew how to look forward. Thanks to my co-supervisor Dr. Peter Carrington from whom I have learnt almost everything and without whom this would be a poorer thesis.

The content of this thesis is the result of a wide collaboration between different research centres and institutes, to which I sincerely give thanks to all for the support. Thanks to our main collaborator, Prof. Magnus C. Wagener from Nelson Mandela University in South Africa, who performed the two-photon photocurrent and electroluminescence measurements as well as the theoretical derivations presented in this thesis. This thesis also includes time-resolved photoluminescence measurements done by the PhD student Shumithira Gandan at Tyndall National Institute (Cork) supervised by Dr. Tomasz Ochalski. I thank also my collaborators at Instituto de Energia Solar in Universidad Politecnica de Madrid, Prof. Pablo G. Linares and Dr. Juan Villa, for the light concentration experimental setup. I also have to thank to Dr. Igor Marko and Prof. Stephen Sweeney at Advanced Technological Institute in Surrey University for hydrostatic pressure measurements.

At the physics department at Lancaster University there were a bunch of people that have contributed to this research indirectly - Dr. Andrew Marshall and Dr. Adam Craig who managed the MBE system and taught me to be an independent user; Prof. Magnus Hayne and Dr. Peter Hodgson running the photoluminescence lab and discussing with

me about GaSb/GaAs QR properties; Dr. Qi Lu in charge of the labs of our research group and giving me training in device fabrication; and finally the last but not the least, Dr. Kunal Lulla, the cleanroom manager that apart from his strong friendship collaborated closely with me during the first months building and improving the recipe for fabricating the devices presented in this thesis.

Now I move to thank to all the people who work every day in the department, the people behind the scenes, without whom the physics department will not be what it is. In the low temperature lab, special thanks to Alan Stokes for making the day more fun with his jokes and being always so kind. In the electrical workshop, thanks to Stephen Holt, Ashley Wilson and John Statter for their outstanding work. In the mechanical workshop, special thanks to Graham Chapman for his understanding and accuracy in his work. Also thanks to Dr. Christopher Somerton the cleanroom technician, Robin Lewsey IT engineer, Shonah Ion responsible for safety and security in the working areas, and to Stephen Holden storekeeper, known to most as Stevie store, thanks for his tips in northern English making the day more enjoyable when you need to buy something from the store.

Following on to all the people for gave a warm welcome at my arrival at Lancaster - Nathan Woollett, Jean Spiece who most know as Juanito, Maxime Lucas, Simon Malzard, and Will Gibby. Thanks to all the people that were with me from the very beginning until the end. My dear friend Eva Repiso Menendez, yes the Spanish people have two unpronounceable surnames, that has shared with me not just the “bumpy roads” as she described but who has shared with me her joy for life and from whom I have learnt to be more brave. To James Keen that since the very beginning has been at my side supporting me in a way I cannot describe. James Eldholm, that always will be Jedholm, my office mate that become a very close friend and my personal cycling coach! Thanks to all those whom I met during these years and that have become a very

especial part of the journey - Marjan, Veronica, Ryan, Emiliano, Charlotte, Laura and Ofogh, and all the Spanish community, making me feel like at home building a small family: Marta, Ramon, Elena, Charalambos, Vanesa, and Kunal and Eva as I have already mentioned.

I have had the opportunity not just to share the PhD experience with my colleagues at Lancaster but also with an amazing group of people from all the world. PROMIS is not just an international network for academic training it has definitely been much more than that. Very special thanks to all of you for making from our training trips an extremely fun time: Davide, Lucas, Shumithira, Atif, Shalini, Julie, Stefano, Flavio, Mario, Mayank, Salman, Emma, Reza and Saed.

And I want to end with all the people that always have been there in the distance, but I have felt very close. Moving to another country, another language and another culture is exciting but without the emotional support of all my friends will not have been possible. Special thanks to my best friend Esther, and my close circle of friends that I met during my time in Madrid: Marta, Oriana, Héctor, Carmen, David, Maria, Jose, Laura, Fran, Nerea, Laura and Dani. Returning to Madrid for work or fun is always a pleasure having all of you there.

And from further in the distance but even closer to my heart, my friends from Canary Islands, Chema, Cecilia, Masabel and Amalia. As always, the best is left for the very end, my mother, whom without her infinite support in all the possible ways I will not be the person I am, she has always supported me to go higher and further, and here I am completing the PhD in United Kingdom. Also thanks to my brother and sister in law for their support and love.

Publications

1. J. Tournet, S. Parola, A. Vauthelin, D. Montesdeoca, S. Soresi, F. Martinez, Q. Lu, Y. Cuminal, P.J. Carrington, J. Décobert, A. Krier, Y. Rouillard and E. Tournié. 'GaSb-based solar cells for multi-junction integration on Si substrates', *Solar Energy Materials and Solar Cells*, 191 (2019) 444-450.

2. Q. Lu, R. Beanland, D. Montesdeoca, P. Carrington, A.R.J. Marshall, and A. Krier. 'Low bandgap GaInAsSb thermophotovoltaic cells on GaAs substrate with advanced metamorphic buffer layer', *Solar Energy Materials and Solar Cells*, 191 (2018) 406-412.

3. M. C. Wagener, D. Montesdeoca, J. R. Botha, A. Krier, and P. J. Carrington. 'Hole capture and emission dynamics of type-II GaSb/GaAs quantum ring solar cells', *Solar Energy Materials and Solar Cells*, 189 (2019) 233-238.

4. D. Montesdeoca, P. J. Carrington, I. Markov, M. C. Wagener, S.J. Sweeney, and A. Krier. 'Open circuit voltage increase of GaSb/GaAs quantum ring solar cells under high hydrostatic pressure', *Solar Energy Materials and Solar Cells* 187 (2018) 227-232.

5. D. Montesdeoca, P.D. Hodgson, P.J. Carrington, A. Marshall, and A. Krier. 'Coupling study in type II GaSb/GaAs quantum ring solar cells' *Proceedings of WOCSDICE* (2018) 52-53, 2 p.

6. P.J. Carrington, D. Montesdeoca, H. Fujita, J. S. James Asirvatham, M. C. Wagener, J. R. Botha, A. Marshall and A. Krier. 'Type II GaSb/GaAs quantum rings with extended photoresponse for efficient solar cells' *Proceedings of SPIE* 9937 (2015) 993708, 7 p.

7. M. C. Wagener, D. Montesdeoca, P.D. Hodgson, Q. Lu, J. R. Botha, P.J. Carrington, A. Marshall, and A. Krier. 'Electroluminescence and solar concentration correspondence in GaSb/GaAs Intermediate Band Solar Cell '. – paper under preparation.

8. D. Montesdeoca, E. Delli, M. C. Wagener, P.D. Hodgson, Q. Lu, A. Marshall, A. Krier, J. R. Botha, and P.J. Carrington. "Integration into Silicon substrates for GaSb/GaAs quantun ring solar cell". – paper under preparation.

Conference Presentations

1. D. Montesdeoca, P. J. Carrington, I. Markov, M. C. Wagener, S.J. Sweeney, A. Krier. 'Open circuit voltage increase of GaSb/GaAs quantum ring solar cells under hydrostatic pressure'. **MBE 2018**, Shanghai, China. (Talk)

2. D. Montesdeoca, P. J. Carrington, I. Markov, M. C. Wagener, S.J. Sweeney, A. Krier. 'Hydrostatic effect on open-circuit voltage in GaSb/GaAs quantum ring solar cells'. **HPSP 2018 & WHS 2**, Barcelona, Spain. (Talk)

3. D. Montesdeoca, P.D. Hodgson, P.J. Carrington, A. Marshall and A. Krier. 'Coupling study in type II GaSb/GaAs quantum ring solar cells' **WOCSDICE 2018**, Bucharest, Romania. (Talk)

4. S. Gandan, D. Montesdeoca, P.D. Hodgson, P.J. Carrington, A. Marshall, A. Krier, J.S.D. Morales, T.J. Ochalski. 'Carrier dynamics of type-II GaSb/GaAs quantum rings for solar cells' **SPIE Photonics West 2018**, San Francisco, USA. (Talk).

5. D. Montesdeoca, P.D. Hodgson, P.J. Carrington, A. Marshall and A. Krier. 'Increasing stack density in type II GaSb/GaAs quantum ring intermediate band solar cells', **Royal Society of Chemistry seminar 2018**- Next Generation Materials for Photovoltaics, London, UK. (Talk)

6. D. Montesdeoca, P.D. Hodgson, P.J. Carrington, A. Marshall and A. Krier. 'Growth and characterization of GaSb/GaAs quantum ring solar cells'. **Christmas conference 2017**, Lancaster, UK. (Talk)

7. D. Montesdeoca, P.D. Hodgson, P.J. Carrington, A. Marshall and A. Krier. 'Type II GaSb/GaAs quantum ring intermediate band solar cell'. **AEM 2017**, Surrey, UK. (Poster)

8. D. Montesdeoca, P.D. Hodgson, P.J. Carrington, A. Marshall and A. Krier. 'Type II GaSb/GaAs quantum ring intermediate band solar cell'. **UK Semiconductors 2017** Sheffield, UK. (Poster)

9. D. Montesdeoca, P.D. Hodgson, P.J. Carrington, A. Marshall and A. Krier. 'Miniband formation in Type II GaSb/GaAs quantum ring solar cell'. **SIOE 2017**, Cardiff, UK. (Poster)

10. D. Montesdeoca, P.D. Hodgson, P.J. Carrington, A. Marshall and A. Krier. 'Two photon photo-current in GaSb/GaAs quantum ring solar cell'. **Photovoltaic workshop Imperial College 2016**, London, UK. (Poster)

11. D. Montesdeoca, P.D. Hodgson, P.J. Carrington, A. Marshall and A. Krier. 'GaSb/GaAs quantum ring for intermediate band solar cell' **MBE 2016**, Montpellier, France. (Poster)

12. D. Montesdeoca, P. J. Carrington, H. Fujita, J. James, M. C. Wagener, J. R. Botha, A. R.J. Marshall, and A. Krier. 'Quantum ring solar cells'. **Exhibition MSI 2016** Lancaster, UK. (Poster)

Contents

List of Figures

List of Tables

Chapter 1

Introduction

The development of society depends on access to electricity, for which the demand increases every year. From 2009 to 2017 human needs increased by 15%, reaching almost 19 TW/year [1, 2], and by 2050 it is expected to rise up to 27 TW/year (assuming linear growth). However, today we still depend mostly on fossil fuels, but reserves are limited and we need to develop alternative renewable energy sources. Solar energy has a great potential, since 1kW of energy falls on 1 m^2 surface perpendicular to the Sun's rays on a clear day at sea level. If we were able to collect the sun´s energy falling on all available land (~ 150 Mkm^2 [3]) we could obtain 23,000 TW/year, which is much larger than expected human needs for 2050. Figure 1.1 compares the available energy from renewable (TW/year), fossil fuels (TW in total reserve) and the world energy needs in 2009 (16 TW). Clearly, solar energy shows the highest potential among the different renewable energies. Even when considering the limitations of land installation/transportation ([4, 5]) and photovoltaic panels with an efficiency of 20%, the one-year solar potential would be of the order of the planetary reserves of coal. A multiple-year outlook unquestionably shows that if it could be successfully implemented, solar is the overwhelming energy solution for the future of the planet [6]. Also, solar energy is the only energy source suitable for isolated and remote (off-grid) areas, as well as in urban areas and in space.

Currently, the solar market is dominated by silicon solar cells with an efficiency of ~27% (mono-crystalline cell) under concentration [7], although many installations are significantly less than this. Meanwhile, GaAs based solar cells have achieved efficiencies as high as 30.5% [7]. However, cells based on a single junction (SJSC) are

limited by a maximum efficiency of 31%, reaching 41% under maximum solar concentration of 46,500 suns [8].

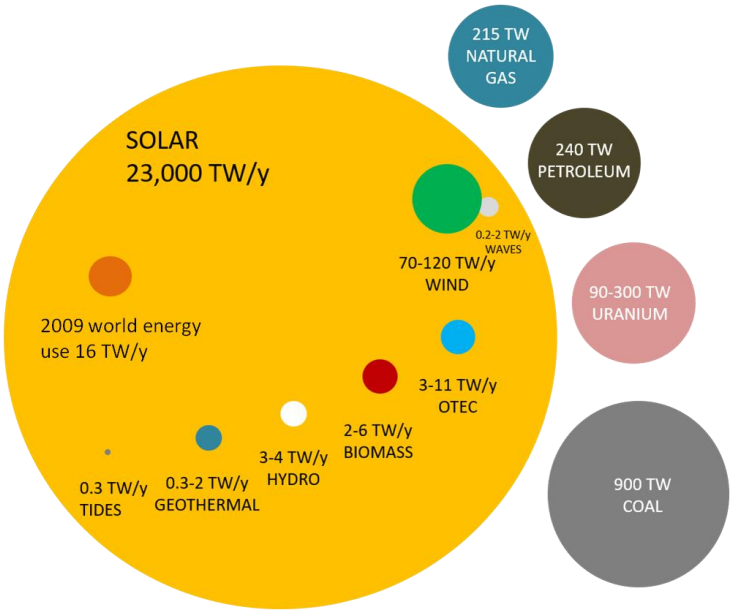

Figure 1.1. The diagram shows the available energy in TW per year for the different renewable energy sources (Tides, Geothermal, Hydro, Biomass, OTEC, Wind and Solar), and the energy available in the total reserve of fossil fuels (Natural Gas, Petroleum, Uranium and Coal). Solar energy is the one with the largest availability of 23,000 TW/year (yellow) where the world needs are just 16 TW/ year (orange).

The so-called first generation SJSC is based on thick devices, using a large amount of semiconductor material, increasing the cost of the final device. Over the last decades the cost per watt of Silicon panels has decreased dramatically, from 76 to 0.30 $/watt between 1977 and 2015, as shown in Figure 1.2(a). Figure 1.2(b) shows how in the second (II) and third (III) generation solar cells the price per solar panel is reduced compared with the first generation (I). The second generation consists of thin film technology, based on CdS, a-Si, $CuInSe_2$, CdTe or CIGS, the latter achieving an efficiency of 22.9% [9]. However, the second generation is also limited by the SJSC efficiency limit. The third generation involves different approaches to achieve high efficiency surpassing the SJSC limit, but still limited by the thermodynamic limit of 87% under maximum concentration. The most well-known among all of the approaches in the third generation is the multi-junction solar cell (MJSC), which to date has

achieved an efficiency of 46% [10]. Other emergent concepts exploit multiple e-h pairs, hot carriers, multiband absorption and thermo-photovoltaics [11].

The SJSC efficiency limit is a consequence of the mismatch between the relatively narrow spectral absorption of the semiconductor and the broad band solar spectrum. The light absorption in a semiconductor is limited by its bandgap, such that photons with energy much larger than the bandgap lose energy via carrier thermalization, and photons with energy lower than the bandgap are lost by transmission.

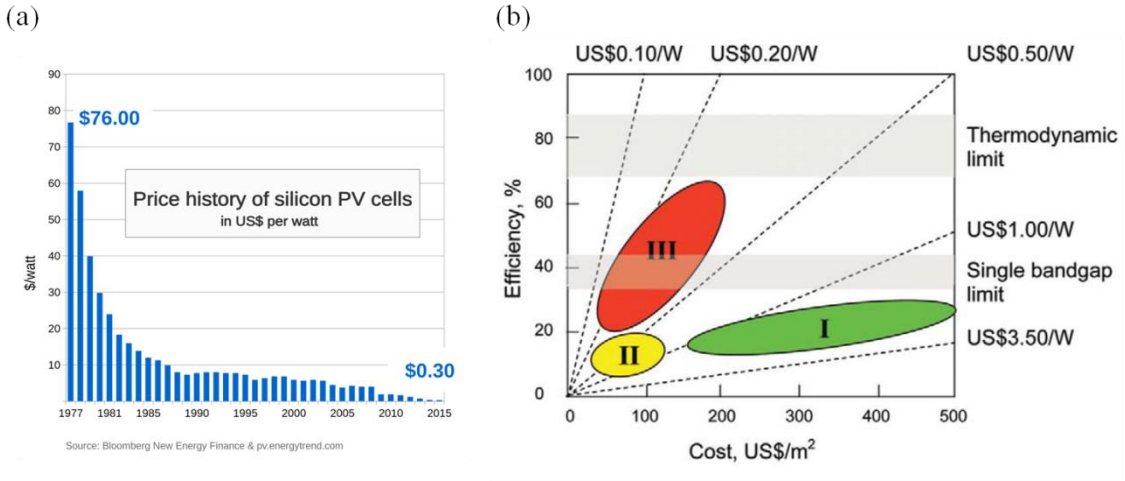

Figure 1.2. (a) Cost ($) per watt of Silicon photovoltaic cells from 1977 to 2015, the price has dropped from 76 to 0.30 $/watt [12]. (b) Efficiency and cost projections for first- (I), second- (II), and third generation (III) PV technologies (Si-based, thin-films, and advanced thin-films, respectively) [13].

In a MJSC, two (or more) cells with different bandgaps are stacked on top of each other, so that each cell absorbs a different part of the solar spectrum, improving sunlight absorption. Theoretically, in the ideal case of infinite junctions, with individual cells operating independently, the maximum achievable efficiency is 87%. In this case, thermalization and transmission losses are suppressed, and the efficiency is determined just by the thermodynamic limit (see *Background Theory* chapter section 2.4.3). However, in a MJSC the multiple cells are connected in series, and each of them must be carefully designed to produce the same current within ~5%, if not the cells start consuming power instead of generating it. Also, series connection between consecutive cells has to be controlled by building low resistance tunnel junctions between them. The

specific requirements for developing MJSCs make this approach expensive so that they are currently limited to use in large scale concentrator systems. [14]

An attractive alternative to MJSC is the intermediate band solar cell (IBSC), which is a particular case of the multiband approach. The principle for high efficiency is similar to that in the MJSC, splitting up the spectral absorption to reduce thermalization and transmission losses to surpass the SJSC efficiency limit. An IBSC consists of a SJSC with a narrow band in the middle of the bandgap, which enables two extra optical absorption transitions – valence band to intermediate band (VB-IB) and intermediate band to conduction band (IB-CB) – which can generate additional photocurrent without reducing the output voltage (see section 2.5 in *Background Theory* chapter). Figure 1.3 compares the maximum theoretical efficiency for an IBSC, a two-junction (tandem) solar cell, and a SJSC (single gap) calculated by Luque et. al [15]. The IBSC exhibits the highest efficiency of 63%, for a bandgap of 1.93 eV and an energy difference between CB and IB of 0.7 eV (ε_i). It is more than 20% higher than the SJSC, without implementing tunnel junctions or requiring a tandem structure.

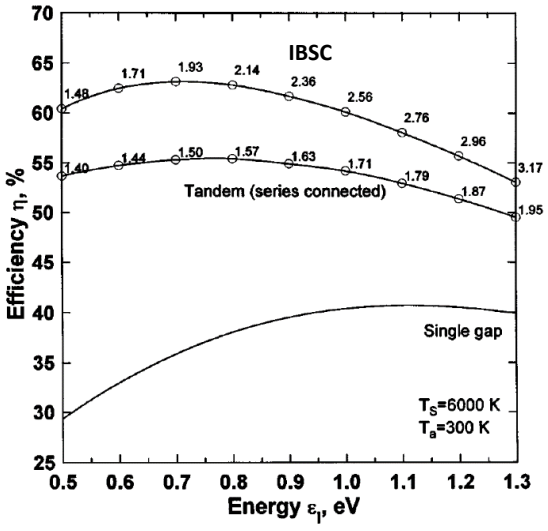

Figure 1.3. Calculated power conversion efficiency limits as a function of the lowest band gap for the three main photovoltaic solar cell approaches: single junction, tandem (two junctions) and IB – adapted from [15].

The most common system used to implement IBSC is the quantum dot solar cell (QDSC), more specifically type-I QDSC, where quantum dots are inserted within a

single junction solar cell [16]. However, type-I In(Ga)As/GaAs QDSC have so far failed to achieve high efficiency for the following reasons. Firstly, QD energy levels are thermally coupled to the CB, and thermionic emission dominates over optical generation for pumping photogenerated electrons from IB to CB, limiting the photocurrent obtained from the IB [17]. Secondly, the short carrier lifetime in type-I QD reduces output voltage due to the large QD recombination rate [18]. Consequently, type-II QDSC and type-II quantum ring solar cell (QRSC) have been proposed to overcome both of these difficulties [19, 20], offering improved IB performance by reducing the carrier thermal escape rate and enlarging the QD carrier lifetime. However, high efficiency has not yet been achieved with this approach [21].

This thesis studies the potential improvements to type-II GaSb/GaAs QRSC by (i) increasing poor sub-bandgap absorption, and (ii) improving low short-circuit current and open-circuit voltage. The focus is on understanding the main limitations for implementing IBSC with type-II GaSb/GaAs QRSC, by quantifying all the processes involved in QR carrier dynamics. Chapter 1 has motivated and introduced the topic of the thesis. Chapter 2 introduces the background theory required to understand the results. Chapter 3 reviews the main achievements reported in the literature concerning the third generation of photovoltaic. Chapter 4 describes the experimental techniques used in this research. Chapter 5 and 6 present all the experimental and theoretical results, and chapter 7 summarises and concludes the work suggesting future approaches.

Chapter 2

Background theory

2.1 Band structure of semiconductors

The properties of solids are conventionally described using band theory which successfully accounts for the differences between metals, insulators and semiconductors. The two main bands in a material are the (filled) valence band and the (empty) conduction band, the difference in energy between them (the bandgap) determines the electrical conductivity of the material. Figure 2.1 exhibits the energy distribution of the two bands in metals, semiconductors and insulators. In metals both bands overlap resulting in very high conductivity (10^3 – 10^{10} $\Omega^{-1}cm^{-1}$) as electrons can move freely in the unfilled band. However, in semiconductors the conduction and valence band are separated by a small (~1 eV) bandgap, so that electrons can be thermally excited to the conduction band producing conductivities between 10^{-12} – 10^3 $\Omega^{-1}cm^{-1}$. And, in the case of insulators the bandgap is so large (~5 eV) that electrons cannot reach the conduction band, resulting in negligible conductivity (<10^{-12} $\Omega^{-1}cm^{-1}$). [22]

Figure 2.2(a) shows a simplified band a diagram near the Gamma point (k = 0) for semiconductors, showing conduction band and the three bands of valence band: heavy holes (HH), light holes (LH), and split-off holes (SOH). The energy of each band in k-space is given by,

$$E_C = E_G + \frac{h^2k^2}{2m_e} \tag{2.1}$$

$$E_v(HH, LH) = \frac{-h^2k^2}{2m_{HH,LH}} \tag{2.2}$$

$$E_v(SOH) = -\Delta - \frac{h^2k^2}{2m_{SOH}} \tag{2.3}$$

where E_C, $E_v(HH, LH)$, $E_v(SOH)$ are the energy of the conduction band, heavy holes, light holes and spin orbit holes, respectively; $m_e, m_{HH,LH}, m_{SOH}$ are the corresponding effective masses for each band, *h* is the Planck constant, *k* the momentum and Δ the spin orbit splitting.

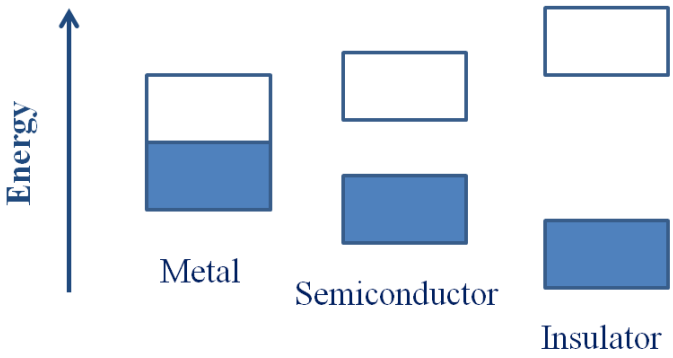

Figure 2.1. Valence band (blue rectangles) and conduction band (white rectangles) in metals, semiconductors and insulators.

The intrinsic carrier concentration in a semiconductor is controlled by E_G/K_BT, the ratio of the energy bandgap and the temperature. Assuming parabolic bands the number of electrons excited to the conduction band at temperature *T* is given by the Fermi-Dirac distribution integrated up in energy,

$$F(E) = \frac{1}{e^{E-E_F/k_BT}+1} \tag{2.4}$$

where E_F is the Fermi energy or chemical potential and k_B is the Boltzmann constant. Figure 2.2(b) shows the Fermi distribution function for the case of k_BT<<E_G. As the temperature increases the electrons from valence band are thermally excited to conduction band, and under bias both the excited electrons in the conduction band and holes left in the valence band contribute to the current.

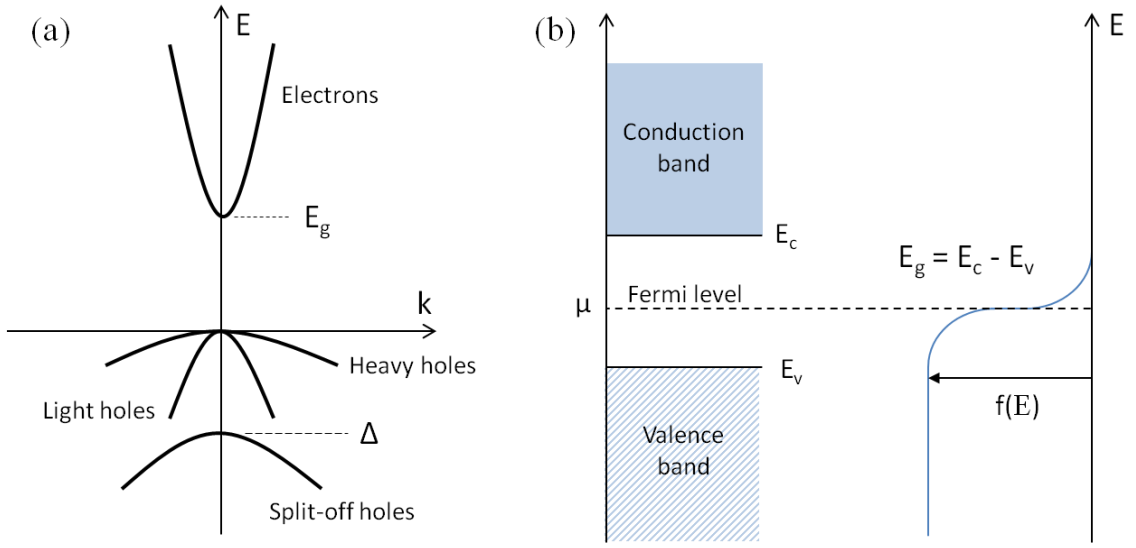

Figure 2.2. (a) Band diagram for electrons (CB) and heavy, light and split-off holes (VB). The difference in energy between the minima of the conduction band (E_C) and the maxima of the valence band (E_V) is the bandgap energy, E_G. And, the energy difference between the maxima of heavy holes and split-off holes is the spin orbit, Δ. (b) Electronic occupation of conduction and valence band determined by Fermi-Dirac distribution function as a function of energy, $f(\in)$, for K_BT<< E_G. The Fermi level (μ) lies in the middle of conduction and valence band.

2.1.1 Temperature dependence of bandgap

When the temperature is increased the bandgap energy is reduced, as the separation between conduction and valence band is shrunk in k space. The two main causes are, the dilation of the crystal lattice due to thermal expansion of the material [23] and the interaction between electrons and the quantized lattice vibrations, the phonons [24]. There are different semi-empirical and empirical models for explaining the bandgap shift with temperature (T), the most common is the Varshni equation [25],

$$E_g = E_0 - \frac{\alpha T^2}{T+\beta} \tag{2.5}$$

where E_0 is the bandgap at 0 K, and α and β are constants that depend on the material, for GaAs α = 2.41x10^{-4} eV/K and and β = 204 K.

2.1.2 Heterostructure band alignment

Heterojunctions are junctions between two different materials, defined by their bandgap and electron affinity, χ. The conduction and valence band discontinuities between materials 1 and 2 are given by

$$\Delta E_C = \chi_1 - \chi_2 \tag{2.6}$$

$$\Delta E_V = (\chi_1 + E_{g1}) - (\chi_2 + E_{g2}) \tag{2.7}$$

Where χ_1 and χ_2 are the electron affinities, and E_{g1} and E_{g2} the bandgaps of material 1 and 2, respectively. The electron affinity is the amount of energy necessary to remove an electron from the conduction band of a semiconductor, in metals the work function (Φ) is the required energy to extract an electron to the vacuum energy level. Figure 2.3 shows the position of E_C and E_V for the main semiconductors depending on their χ, also showing the work function for some metals.

There are three types of band discontinuity determined by the band alignment in the heterostructure as shown in Figure 2.4: (a) type-I, (b) type-II, and (c) type-III. In *type-I*, ΔE_C is positive and ΔE_V is negative, having a conduction band offset (CBO) and a valence band offset (VBO). In a type-I structure like AlGaAs/GaAs/AlGaAs, electrons and holes are confined in the lowest bandgap material (GaAs), as shown in Figure 2.4(a). Type-I structures present large light absorption and short carrier lifetime. Examples of type-I are InAs(Ga,Al)/GaAs and AlGaAs/GaAs.

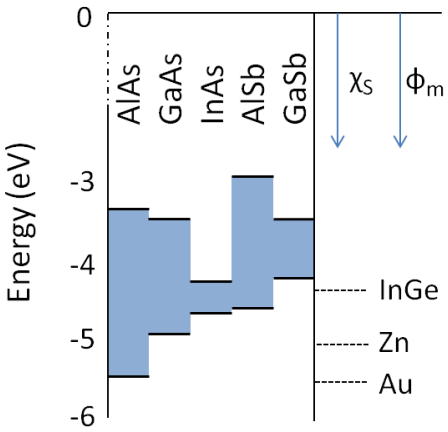

Figure 2.3. Conduction and valence band position for several semiconductors relative to a common vacuum level at E = 0 eV, taking into account the electron affinity of each semiconductor, χ_S. In the right, the work functions for different metals, ϕ_m, are shown for comparison.

In *type-II* there are two possibilities, ΔE_C and ΔE_V are positive as shown in Figure 2.4(b) for GaAs grown on top of GaSb, giving electronic confinement in GaAs layers

sandwiched with GaSb layers with a conduction band offset. Also, ΔE_C and ΔE_V can be negative if we consider the inverse structure, where the holes will be confined in the GaSb layers in GaAs/GaSb/GaAs structure with a valence band offset. Due to low wavefunction overlap in this structure absorption is inhibited and carrier lifetime is enhanced. Examples of type-II are GaSb/GaAs and InAsSb/InAs. In *type-III* the bandgap is broken, allowing electrons to move freely from the valence band of one material to the conduction band of the other material, for example from GaSb to InAs as shown in Figure 2.4(c).

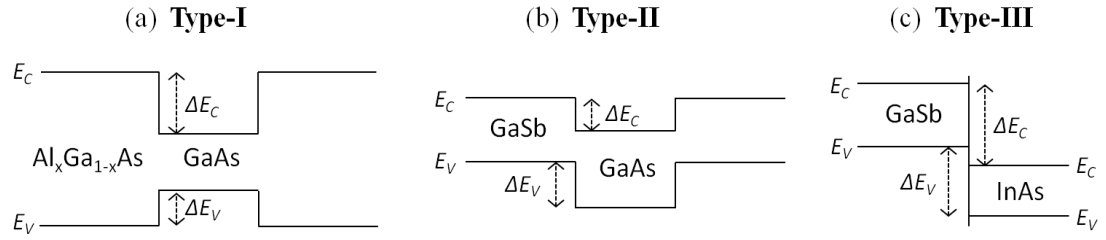

Figure 2.4. Sketches of the band-diagram structure for the three types of heterojunctions: type-I (a), type-II (b) and type-III (c). The conduction and valence band edges, E_C and E_V, are shown together with the band discontinuities, ΔE_C and ΔE_V.

2.1.3 Strained layers

When growing an epitaxial layer with a lattice parameter (a_{layer}) different than the substrate (a_{sub}) the lattice mismatch between the two materials is given by $\delta = (a_{layer} - a_{\mathrm{sub}})/a_{layer}$. When $\delta \geq 2x10^{-3}$ the strain between the two materials is too large and above the critical thickness defects and dislocations are generated due to the relaxation of the top layer [26]. For $\delta < 2x10^{-3}$ the elastic strain can be accommodated in the layer growth without degrading the crystal quality of the structure. Depending on the sign of δ the layer grown on top of the substrate is tensile strained (positive) or compressive strained (negative), as sketched in Figure 2.5(a) and 2.5(b). Lattice matched heterostructures ($a_{layer} = a_{\mathrm{sub}}$) give the best device performance due to low dislocation density. Strain induces changes in the band structure like shifting upwards GaSb conduction band when growing a layer on top of GaAs substrate [27].

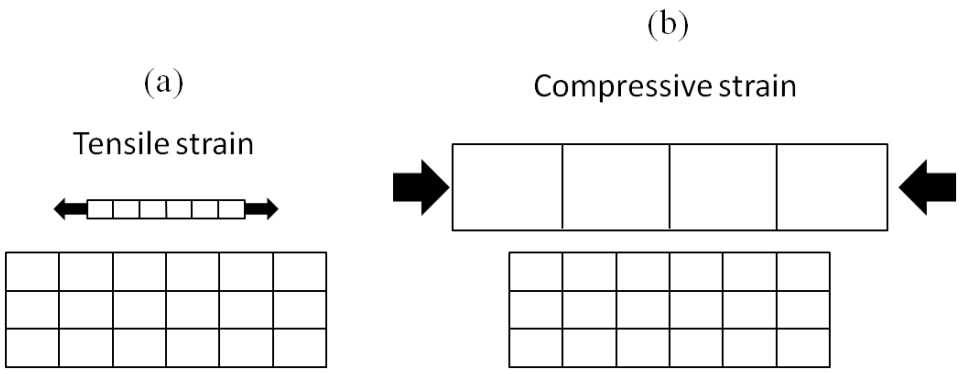

Figure 2.5. Sketch of a tensile strained layer (a) and a compressive strained layer (b) grown on top of the substrate. The rectangle in the bottom represents the substrate with 3x6 unit cells, and on the top is the strained layer with 1x6 unit cells.

2.1.4 Quantum structures

As discussed in section 2.1.2, carriers can be confined in type-I or type-II structures. When the size of the confinement is similar to the de Broglie wavelength, $\lambda_B = h / p$ (h is Planck's constant and p the particle's momentum), the energy level distribution is discrete. The confined energy levels of the particle are obtained by solving the time independent Schrödinger equation:

$$E\psi = -\frac{\hbar^2}{2m}\left(\frac{d^2}{dx^2}+\frac{d^2}{dy^2}+\frac{d^2}{dz^2}\right)\psi + V_0(x,y,z)\psi \tag{2.8}$$

where E and m are the energy and mass of the particle, ψ the particle's wavefunction and $V_0(x,y,z)$ the potential function.

In a quantum well (QW), the particles are confined just across the z direction. Considering the well as an infinite potential of length L, the energy of the n^{th} energy level obtained by solving eq. 2.8 is given by

$$E_n = \frac{\hbar^2}{2m}\left(\frac{\pi}{L}\right)^2 n^2 \tag{2.9}$$

In a quantum dot (QD) the confinement is in the three directions, and the energy levels are given by eq. 2.9 for each direction x, y and z (L_x, L_y and L_z). The carriers occupy the energy levels following the density of states (DOS), *g(E)*. The density of carriers per unit energy and unit of volume, *N(E)*, within an energy interval *dE* is given by [28]

$$N(E) = g(E)dE \tag{2.10}$$

Figure 2.6 shows the DOS for the different degrees of confinement. In a bulk material, there is no confinement in any direction (3D) and DOS is a continuous parabolic function with energy. In quantum wells, when there is confinement just in one direction (2D), the DOS follows the step function. For confinement in two directions (1D), nanowires, the DOS is given by the peak function and, in the case of confinement in all directions (0D), quantum dots, DOS is determined by the Dirac delta function. [29]

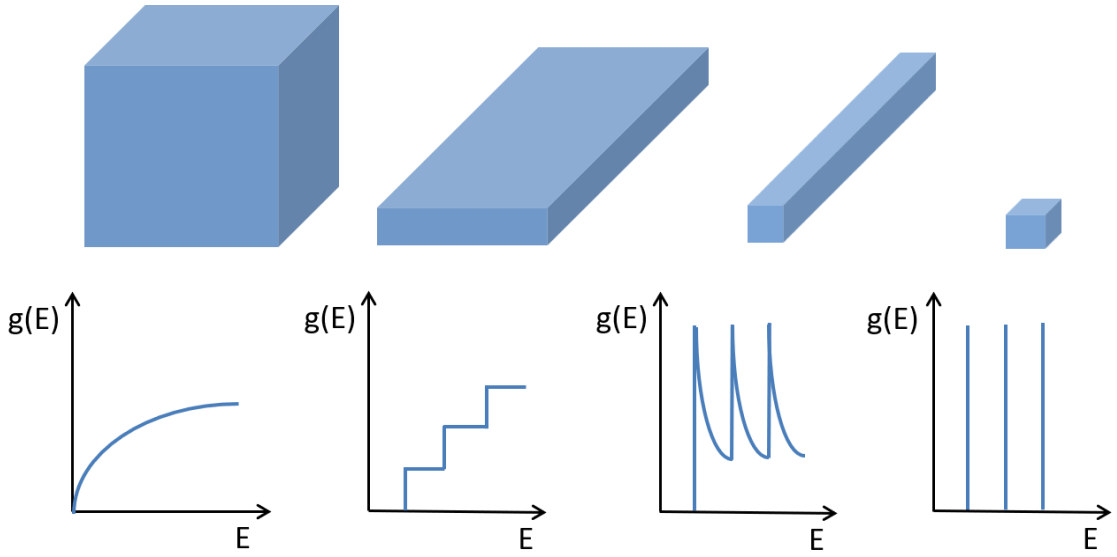

Figure 2.6. Density of states (g(E)) vs energy for the different dimensionalities, having different degree of confinement. In a bulk material (3D-blue), there is no confinement in any direction. In a quantum well (2D-red), the confinement is just along one direction. In a nanowire (1D-green), carriers are confined in two directions, and in a quantum dots (0D-yellow), carriers are confined in the three directions.

The occupation of the energy levels is given by the Fermi-Dirac distribution, described in section 2.1, where the Fermi level lies on the middle of the bandgap in an intrinsic semiconductor. At 0 K electrons will first fill the energy levels with lower energy, and then they will distribute following Pauli's exclusion principle. As the temperature increases, electrons start populating the conduction band, leaving holes in the valence band. By multiplying DOS and Fermi-Dirac distribution it is possible to calculate the distribution of electrons in the bands of a semiconductor.

2.2 Generation and recombination

An electron hole pair (EHP), i.e. an electron in the conduction band and a hole in the valence band, can be generated or recombined through different band-to-band processes, radiative and Auger generation/recombination. An EHP can be generated or recombined radiatively by absorbing or emitting a photon. Also, an EHP can be created or annihilated via Auger absorbing the energy released by the relaxation of a carrier to a lower energy state or the inverse process, the EHP recombines transferring the energy of the transition to a third carrier. An EHP can also be produced or destroyed via band-to-bound processes, where an electron or hole is generated or recombined via energy levels in the middle of the bandgap via Shockley-Read-Hall procesess, and via extra energy levels within the bandgap created close to an interface in heterojunctions or close to the surface via surface recombination. The generated EHPs increase the carrier concentration in the semiconductor, producing photocurrent in the device if the carriers are extracted before they recombine.

2.2.1 Radiative recombination

When an EHP is recombined optically a photon is emitted with an energy equal to the bandgap. In the inverse process, an EHP is generated by absorbing a photon with energy equal to or larger than the bandgap. These two processes are sketched in Figure 2.7.

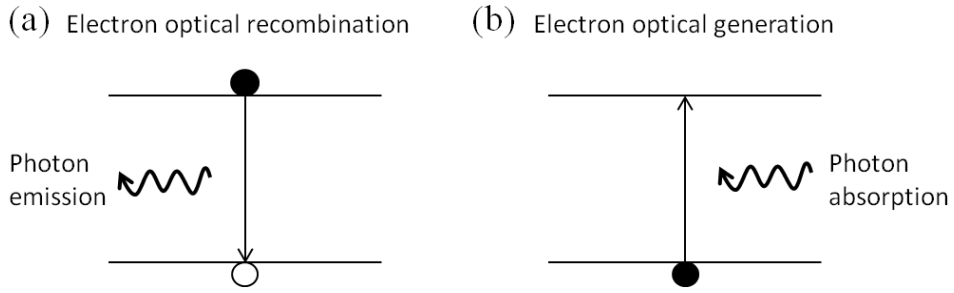

Figure 2.7. Diagram of electron optical recombination (a) and generation (b). When an electron in the conduction band recombines optically with a hole in the valence band, a photon is emitted. In the inverse process a photon is absorbed and an EHP is optically generated.

Radiative recombination

In equilibrium conditions, without any external stimuli, the law of mass action states that the product of the hole and electron population is a constant:

$$n_0 p_0 = n_i^2 \tag{2.11}$$

where n_i is the intrinsic carrier concentration, and n_0 and p_0 are the electron and hole concentration in equilibrium.

By absorbing light or by injecting current, extra carriers are generated in the semiconductor, and the population of electrons and holes is modified:

$$n = n_0 + \Delta n \ and \ p = p_0 + \Delta p \tag{2.12}$$

where Δn and Δp are the excess electron and hole population, respectively.

In semiconductors, the recombination rate of the different mechanisms is fundamental to quantify each process, and to obtain the dominant and limiting recombination process. The rate at which the carrier concentration decreases (R), corresponding to electrons in the conduction band and holes in the valence band, is proportional to the hole and electron population,

$$R = -\frac{dn}{dt} = -\frac{dp}{dt} = Bnp \tag{2.13}$$

This equation is the so-called *bimolecular rate equation*, and B is the bimolecular recombination coefficient ~ 10^{-11} – 10^{-9} cm^3/s for direct-bandgap III-V semiconductors. [30]

Radiative recombination lifetime for low-level excitation

The recombination dynamics with time are essential to understand the behaviour of carriers during time-dependent measurements. Since electrons and holes annihilate each other in a recombination process, then

$$\Delta n(t) = \Delta p(t). \tag{2.14}$$

Using the Bimolecular rate equation to describe the increase in electron and hole population with time, we obtain

$$R = B[n_0 + \Delta n(t)][p_0 + \Delta p(t)]. \quad (2.15)$$

For low-level excitation, $\Delta n << (n_0 + p_0)$, and by applying eq. 2.14 in eq. 2.15, we have

$$R = Bn_i^2 + B(n_0 + p_0)\Delta n(t) = R_0 + R_{excess} \quad (2.16)$$

where R_0 and R_{excess} are the equilibrium and the excess recombination rates, respectively.

The time-dependent carrier concentration is given by

$$\frac{dn(t)}{dt} = G - R = (G_0 + G_{excess}) - (R_0 + R_{excess}) \quad (2.17)$$

Where, G_0 and R_0 are the generation and recombination rates in equilibrium, respectively.

Now, we obtain the change in electron population after turning off the external stimuli (light or injected current) where, $G_{excess} = 0$ and using $R_0 = G_0$ we have,

$$\frac{d\Delta n(t)}{dt} = -B(n_0 + p_0)\Delta n(t) \quad (2.18)$$

The solution of this differential equation is,

$$\Delta n(t) = \Delta n_0 e^{-B(n_0+p_0)t} = \Delta n_0 e^{-t/\tau} \quad (2.19)$$

where, $\tau_{rad}^{low-level} = 1/B(n_0 + p_0)$ is the carrier lifetime for a radiative process under low-level excitation.

In the case of a p-type semiconductor $n_0 + p_0 \approx p_0 = N_A$, and the carrier lifetime of eq. 2.19 reduces to

$$\tau_n = \frac{1}{BN_A} \quad (2.20)$$

where N_A is the acceptor density. Similarly, in a n-type semiconductor $n_0 + p_0 \approx n_0 = N_D$, the carrier lifetime reduces to

$$\tau_p = \frac{1}{BN_D} \quad (2.21)$$

where N_D is the donor density.

Radiative recombination lifetime for high-level excitation

For high-level excitation, $\Delta n >> (n_0 + p_0)$, eq. 2.18 becomes

$$\frac{d\Delta n(t)}{dt} = -B\Delta n(t), \tag{2.22}$$

and the solution is given by

$$\Delta n(t) = \frac{1}{Bt+\Delta n_0^{-1}}. \tag{2.23}$$

Obtaining a time-constant for a non-exponential decay of

$$\tau_{rad}^{high-level}(t) = t + \frac{1}{B\Delta n_0}. \tag{2.24}$$

For long enough time $\tau_{rad}^{high-level}$ tends to $\tau_{rad}^{low-level}$.

2.2.2 Auger recombination

In an Auger recombination process, the energy released from the recombination of the EHP is transferred to a free carrier, exciting the electron or hole to a higher energy band. In the inverse process an EHP is generated via an Auger generation process, when absorbing the energy transferred from a free carrier relaxing to a lower energy band. The Auger coefficient is large in narrow bandgap materials and decreases with increasing bandgap, being negligible in wide bandgap materials. [31]

2.2.3 Shockley-Read-Hall recombination

The above processes are band-to-band, where an electron in the conduction band recombines directly with a hole in the valence band. However, band-to-bound generation and recombination also occur in semiconductors containing unintentional impurities or defects producing deep levels in the middle the bandgap which act as non-radiative recombination centres. These processes are called Shockley-Read-Hall (SRH). There are four different SRH processes, where electrons and holes can be trapped by deep centres and/or reemitted from deep centres as shown in Figure 2.9. EHP band-to-bound recombination occurs in two steps, combining processes (a) and (c) from Figure 2.8, a free electron in the conduction band is first trapped in the deep centre and later re-emitted to the valence band where it recombines with a free hole. Or inversely, an EHP is generated combining processes (b) and (d) from Figure 2.8, where firstly an electron

is trapped by the deep centre from the VB (leaving a hole in its place) and later reemitted to the conduction band. SRH contribution to EHP generation/recombination decreases with increasing temperature, as the carrier's thermal energy increases and carriers escape to the conduction or valence band. In high carrier injection conditions, traps are saturated and SRH processes are eventually saturated.

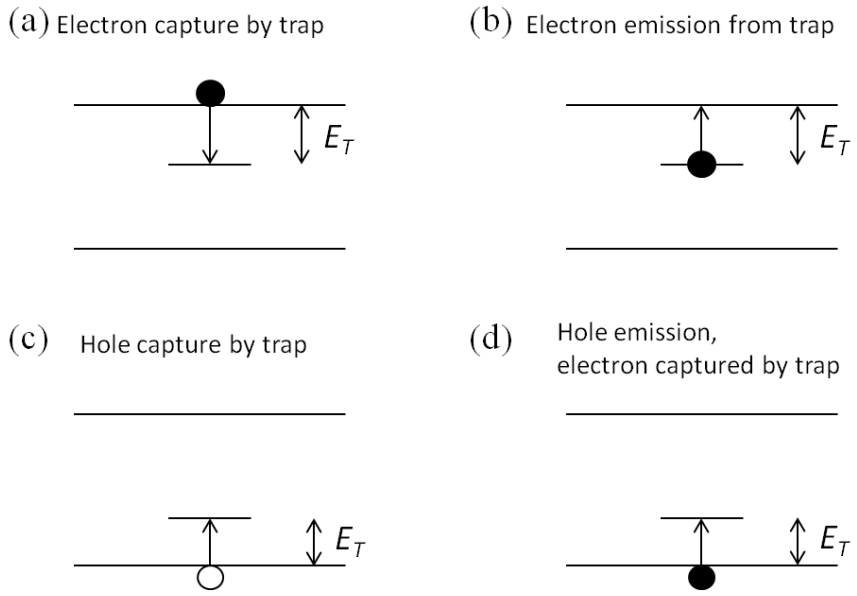

Figure 2.8. Diagrams of Shockley-Read-Hall (SRH) band-to bound recombination and generation processes. An electron from the conduction band can be trapped by a deep centre (a), or be emitted from a deep centre to the conduction band (b). A hole in the valence band can be trapped by a deep centre (c), or be emitted back to the valence band.

The non-radiative recombination carrier lifetime depends on the energy E_T and the concentration N_T of the deep level trap. Taking into account that SRH is limited by the capture of minority carriers, meaning that capture of a majority carrier is more likely, then the lifetime is given by [32]

$$\frac{1}{\tau_{SR}} = \frac{p_0+n_0+\Delta n}{\tau_{p0}(n_0+n_1+\Delta n)+ \tau_{n0}(p_0+p_1+\Delta p)} \tag{2.25}$$

where $\tau_{p0} = 1/N_T v_p \sigma_p$ and $\tau_{n0} = 1/N_T v_n \sigma_n$, with $v_{p,n}$ and $\sigma_{p,n}$ the thermal velocity and the capture cross-section of the traps of holes and electrons, respectively. $n_1 = n_i \exp\left(\frac{E_T - E_{Fi}}{KT}\right)$ and $p = n_i \exp\left(\frac{E_{Fi} - E_T}{KT}\right)$, are the electron and hole population if the

Fermi level is located at the trap level. For small deviations of equilibrium conditions, $\Delta n << p_0$, eq. 2.25 simplifies to

$$\tau_{SR} = \tau_{n_0} \frac{p_0+p_1}{p_0+ n_0}. \quad (2.26)$$

In a semiconductor the total carrier lifetime, τ, includes both the radiative, τ_r, and non-radiative, τ_{nr}, carrier lifetimes,

$$\tau^{-1} = \tau_r^{-1} + \tau_{nr}^{-1}. \quad (2.27)$$

so that the probability of radiative recombination or more usefully, internal quantum efficiency is given by

$$\eta_i = \frac{\tau_r^{-1}}{\tau_r^{-1}+\tau_{nr}^{-1}}. \quad (2.28)$$

2.2.4 Surface recombination

On the surface of a semiconductor, the lack of crystal periodicity of the lattice and the unbounded valence orbitals generating partially filled electron orbitals at the surface (dangling bonds), create electronic states inside the forbidden bandgap. The extra states acts as non-radiative recombination centres. The minority carrier concentration at the surface for a p-type semiconductor under illumination is given by

$$n(x) = n_0 + \Delta n_\infty \left(1 - \frac{\tau_n S\, exp(-x/L_n)}{L_n+ \tau_n S}\right) \quad (2.29)$$

where $x=0$ denotes the surface and $x=\infty$ the bulk, S is the surface recombination velocity, and L_n the electron diffusion length. For large values of S, the minority carrier concentration at the surface is similar to the equilibrium values. GaAs has particularly high values for S (10^6 cm/s) compared with InP (10^3 cm/s) and Si (10^1 cm/s).

2.3 Type-II GaSb/GaAs Quantum Ring (QR)

The self-assembled type-II GaSb/GaAs nanostructures can be QD or quantum rings (QR) depending on growth conditions as will be explained in detail in *Experimental Techniques* chapter section 4.1.4. GaSb/GaAs QD turn into QR by Sb segregation from

the centre of the QD resulting in a ring shape of GaSb atoms surrounded by GaAs atoms. By tuning the growth parameters QR can be grown preferentially. A quantum ring accumulates less strain than a QD due to a decreased volume of the nanostructure resulting in higher crystal quality, also as shown in Figure 2.9 electrons stay in the centre hole of the ring (GaAs) as well as in its close surrounding (GaAs) in a QR increasing optical absorption compared with a QD as explained in *Literature review* chapter section 3.2.2. The electrons in the conduction band are attracted by Coulomb force to the holes strongly confined due to the large VB offset between GaAs and GaSb (~0.5 eV) [33].

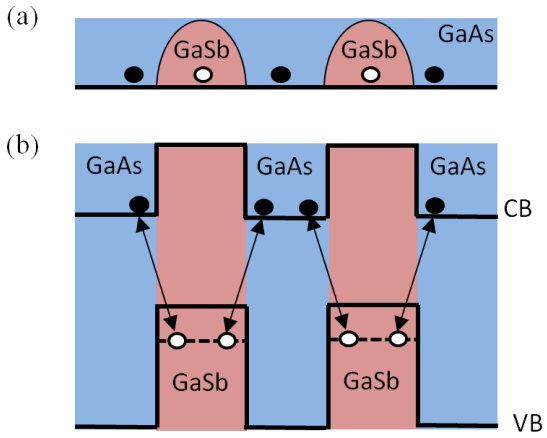

Figure 2.9. (a) Cross section of a GaSb quantum ring (QR) embedded in a GaAs matrix. Holes (white circles) are trapped inside the ring while electrons (black circles) are attracted by them, staying in the centre hole of the ring and in its close surroundings. (b) Corresponding band structure of the type-II GaSb/GaAs QR, showing only the ground state energy level. Wetting layer has been ignored for simplicity.

2.3.1 Charging mechanism in type-II GaSb/GaAs quantum rings

In addition to radiative and non-radiative generation and recombination processes, it is also important to quantify the charging effects in nanostructures. From photoluminescence (PL) emission the main charging mechanisms can be identified. Band bending typically has the major contribution, however capacitive charging also has to be considered. In Figure 2.10(a) the PL spectra of type-II GaSb/GaAs QR measured by Young et. al. is shown, containing sub-peaks attributed to different hole populations inside the GaSb nanostructures [33]. Hodgson et. al. studied in detail the

contribution of band bending and capacitive charging in this structure, revealing that the capacitive charging effect is stronger [34]. From Figure 2.10(b) the experimental value for capacitive energy per hole is obtained as 24 ± 2 meV. This value is in agreement with theoretical calculations, based on

$$\delta E_{CC} = \frac{e^2 d}{2A\epsilon_0 \epsilon_r} \tag{2.30}$$

where d is the Böhr diameter (10 nm for GaAs), e the electron charge, A the area of the nanostructure (7.5 and 12.5 nm for inner and outer diameter), ϵ_0 the absolute permittivity, and ϵ_r the relative permittivity (12.9 for GaAs). The theoretical capacitive energy for a hole inside the GaSb QR is 22 meV, in agreement with the experimental value.

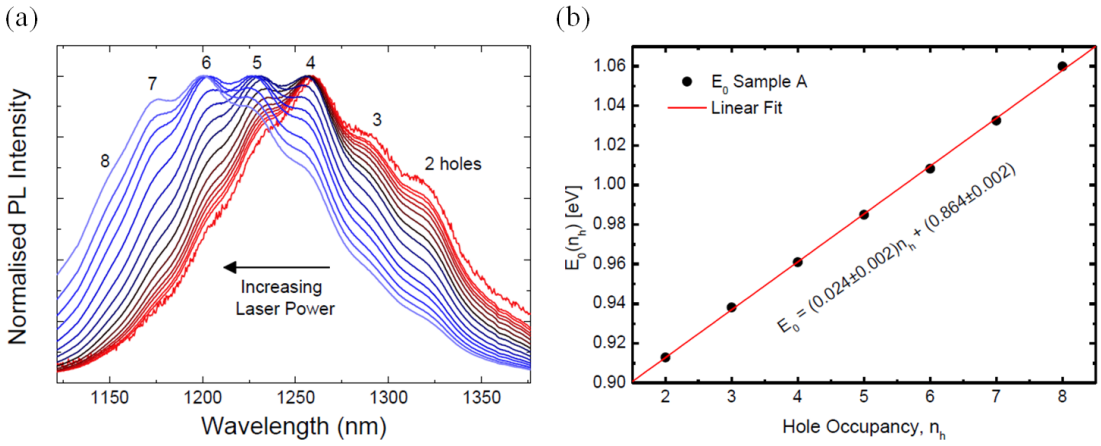

Figure 2.10. (a) Photoluminescence spectra for a GaSb/GaAs nanostructure measured at 4 K under different laser power. From red to blue the laser power is increased blueshifting the energy of the emission. The sub-peaks correspond to different hole population inside the GaSb nanostructure (from 2 to 8). [34] (b) Energy of the ground state (E_0) as a function of hole population in the QD/QR (n_h), the experimental data (black dots) fits to a line (red line) with a slope of 24 ± 2 meV. [35]

2.4 Solar Cell (SC)

The solar cells considered in this work essentially consist of a p-n junction producing electrical current and voltage under illumination. A p-n junction is formed between a p-type material with a acceptor concentration N_A and n-type material with a donor concentration N_D. In the interface of an abrupt p-n junction (depletion region) all the

electrons are ionized and the electron concentration (n) is equal to N_D , and all holes are also ionized with a hole concentration (p) equal to N_A. The Fermi levels of each region before forming a junction are:

$$\phi_n = \psi - \frac{KT}{q}\ln\left(\frac{n}{n_i}\right) \; and \; \phi_p = \psi + \frac{KT}{q}\ln\left(\frac{p}{n_i}\right) \tag{2.31}$$

where $\psi = E_i/q$ is the potential corresponding to the intrinsic semiconductor (E_i=E_g) before adding doping. The output voltage or built in voltage (V_{bi}) obtained from a p-n junction is the difference between the Fermi levels of electrons and holes, $V_{bi} = \phi_p - \phi_n \leq E_g$, limited by the bandgap of the material.

A solar cell is based on a p-n junction, and a broad response is required which is well matched to the solar spectrum, optimizing absorption and carrier extraction. The simple p-n junction can be improved to obtain high efficiency solar cells. Figure 2.11(a) shows a typical solar cell structure consisting of: a highly doped thin contact layer to reduce contact resistance at the front, a wide band gap highly doped window layer to avoid surface recombination without blocking incident light, a thin highly doped emitter to absorb high energy photons, an intrinsic region to separate n-region from p-region, a thick low doped base to absorb low energy photons, and a back surface field (BSF) to avoid surface recombination at the rear. The window layer and BSF are required for blocking carriers close to the contacts avoiding minority carrier recombination. The metal contact pattern is optimized for transmitting the maximum sunlight to the material while collecting the maximum photocurrent, for which finger patterns are the most commonly used. Figure 2.11(b) shows the p-i-n structure of the solar cells studied in this thesis including a contact and window layer. The window layer reflects photogenerated electrons in the emitter so that electrons migrate to the n-region contributing to photocurrent and photovoltage.

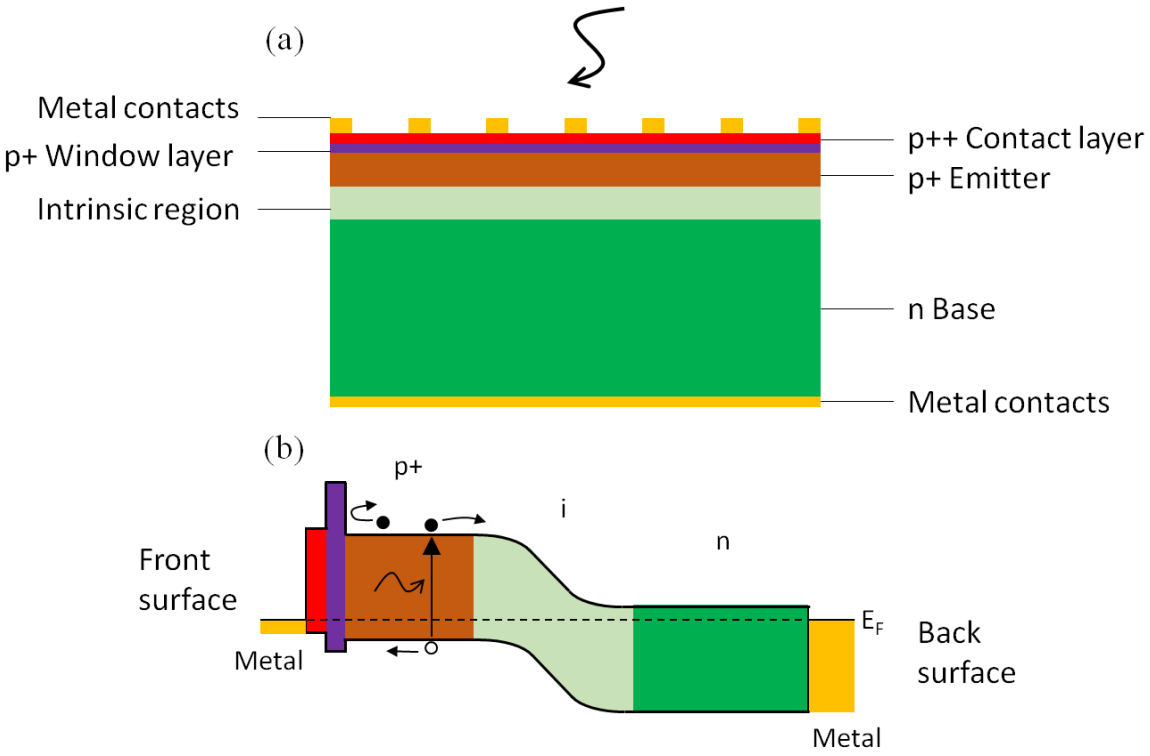

Figure 2.11. (a) Solar cell device based on a p-i-n junction including contact layer, window layer, emitter (p-region), intrinsic region and base (n-region). (b) Band diagram of the corresponding solar cell structure.

Due to high absorption close to the surface in GaAs (Figure 2.12) it is extremely important to add a p-AlGaAs layer in the front of the device to prevent high surface recombination. By adding the AlGaAs layer *S* is typically reduced from 10^6 to 10^4 cm/s. Also, the wide bandgap of AlGaAs transmits most of the light through to the p-GaAs layer. In GaAs the electron diffusion length is higher than that for holes (for the same doping level in GaAs) making p-n junctions more suitable for solar cells than n-p junctions, such that electrons reach the n-contact across the thick p-region before recombining. In addition, high doping in the window layer gives low contact resistance so that the p-GaAs layer can be lightly doped increasing carrier lifetime and consequently improving carrier collection and conversion efficiency.

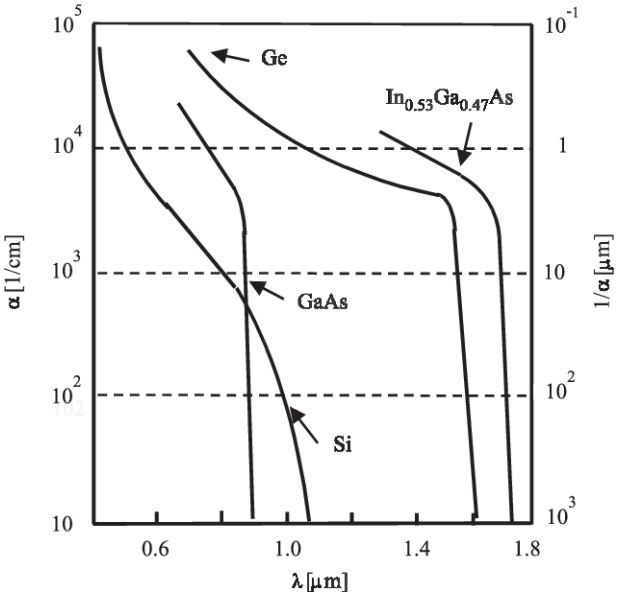

Figure 2.12. Absorption coefficient (α) and penetration depth (1/ α) for Si, GaAs, Ge and InGaAs. Showing high energy photons absorbed close to the surface. GaAs has an absorption coefficient around one order of magnitude higher than Si, making more suitable for solar cell applications. [36]

2.4.1 Junction capacitance

Determining the intrinsic carrier concentration in solar cells is crucial to control the un-intentional impurities in the lattice improving the crystal quality of the material. By measuring the capacitance vs voltage characteristic, depletion width (W), built-in voltage (V_{bi}) , acceptor concentration (N_A) and intrinsic carrier concentration (n_i) can be obtained. The capacitance across the junction with an area A is given by

$$C = \frac{\epsilon_S \epsilon_0 A}{W}. \tag{2.32}$$

Assuming an abrupt junction between the n-region and p-region, W depends on the applied voltage (V_a) and is given by

$$W = \sqrt{\frac{2\epsilon_S \epsilon_0}{q}(V_{bi} - V_a)\frac{N_A + N_D}{N_A N_D}}. \tag{2.33}$$

In the case that one side of the junction is more heavily doped than the other one, eq. 2.33 is simplified. Applying the condition $N_A >> N_D$, the square of the inverse of the capacitance becomes

$$\frac{1}{C^2} = \frac{2}{q\epsilon_s \epsilon_0 N_D A^2}(V_{bi} + V_a) \tag{2.34}$$

obtaining N_D from the slope and V_{bi} from the intercept on the voltage axis from the plot of $1/C^2$ as a function of V_a. By substituting the two values in eq. 2.34, W is obtained at a certain bias. Alternatively, by plotting N_D as a function on W V_{bi} can be obtained from the intercept while N_D corresponds to n_i for $W << W_{grown}$ (W_{grown} is the i-region thickness in a p-i-n structure).

2.4.2 Photovoltaic performance

The equivalent circuit corresponding to a real solar cell is sketched in Figure 2.13, consisting of a diode producing a dark or saturation current I_D plus a current source generating a photocurrent, I_L under illumination, and to account for current and voltage losses series and shunt resistance are included. Series resistance (R_S) includes contact resistance and recombination within the material structure, while shunt resistance (R_{SH}) accounts for leakage current across the sidewalls of the device due to surface recombination. Both can be reduced by improving crystal quality in the material, by optimizing grid design, and by performing edge passivation. In solar cells generally series resistance has a stronger effect compared with shunt resistance on photovoltaic performance.

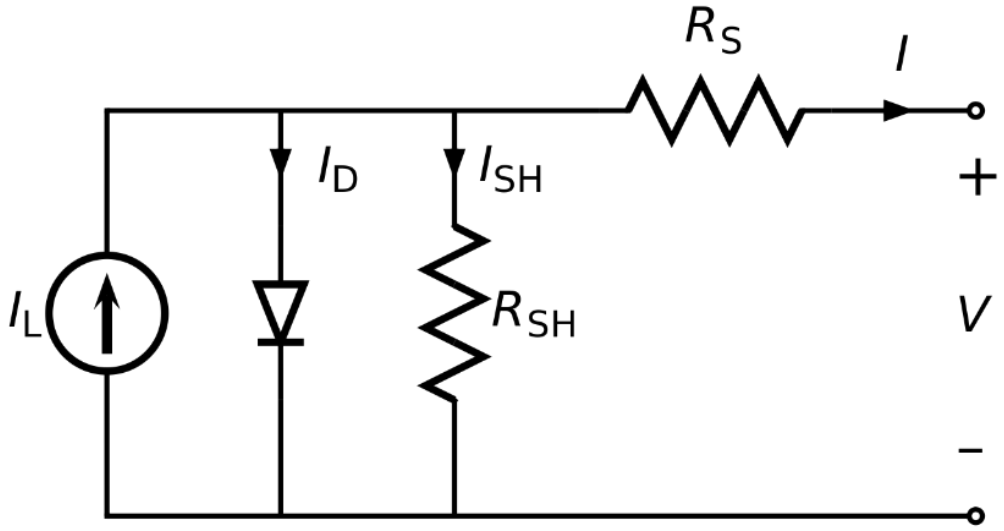

Figure 2.13. Equivalent circuit for a solar cell, under illumination the solar cell produces current (I_L), its contribution to the final current is reduced by the dark current (I_D) and current going through shunt resistance (R_{SH}) in the device (I_{SH}). Finally, the total current (I) goes through the series resistance of the device (R_S), giving a voltage (V) between the positive and negative terminal of the solar cell.

The current flowing in a solar cell (Figure 2.14) is described by

$$I = -I_L + I_D\left(e^{\frac{qV-IR_S}{kT}} - 1\right) + \frac{V-IR_S}{R_{SH}} \tag{2.35}$$

where k is the Boltzmann constant, I_L the illumination current, and I_D dark current, also called reverse or saturation current (I_S). I_D is given by

$$I_D = q\left(\frac{L_n}{\tau_n N_A} + \frac{L_p}{\tau_p N_D}\right) n_i^2 + \frac{qW}{\sqrt{\tau_N \tau_P}} n_i \tag{2.36}$$

where L_n, L_p and τ_n, τ_p are the minority carrier diffusion lengths and the lifetimes of electrons and holes, respectively, N_A and N_D are the p- and n- type doping concentrations, W is the width of the depletion region, and n_i the intrinsic carrier concentration. The dark current has two contributions, diffusion and recombination. Diffusion current depends on the square of n_i (first term of eq. 2.36) and the recombination depends linearly with n_i (second term of eq. 2.36). The square of n_i depends exponentially on the band gap and temperature, given by

$$n_i^2 = N_A N_D e^{-E_g/KT}. \tag{2.37}$$

The illumination current is proportional to the incident flux (ϕ) intensity and depends upon the bandgap of the material, described by

$$I_L(E_g) = Aq\int_{h\nu=E_g}^{\infty} \frac{d\phi_{ph}}{dh\nu} d(h\nu) \tag{2.38}$$

where A is the area of the device. Photons with energy ($h\upsilon$) larger than the bandgap contribute to the photocurrent, those with lower energy lower are lost by transmission. Then, the smaller the bandgap the better because more photons are collected, maximizing I_L.

Eq. 2.35 describes the ideal case, where the current produced in a solar cell is limited by diffusion. However, when generation-recombination current in the depletion region dominates via traps (SRH), the dependence of the photocurrent is given by

$$I = -I_L + I_D\left(e^{\frac{qV-IR_S}{2kT}} - 1\right) + \frac{V-IR_S}{R_{SH}} \tag{2.39}$$

where a factor two is added in the denominator of the exponential. SRH processes reduce current compared with diffusion driven current. In the case that both contribute to current, eq. 2.35 is modified adding the ideality factor (n) in the exponential

$$I = -I_L + I_D\left(e^{\frac{qV-IR_S}{nkT}} - 1\right) + \frac{V-IR_S}{R_{SH}}. \tag{2.40}$$

The ideality factor is obtained from the slope of *ln(I)* vs V at dark conditions ($I_L = 0$) and low current to decrease the series resistance contribution, neglecting shunt resistance. Meanwhile, series resistance is determined by the slope of I vs V at high voltages.

The main photovoltaic parameters are: open-circuit voltage (V_{OC}), short-circuit current (I_{SC}), filling factor (FF), and conversion efficiency (η). Neglecting series and shunt resistance in eq. 2.40 and applying the condition of zero current, we obtain the open-circuit voltage:

$$V_{OC} = \frac{KT}{q}\ln\left(\frac{I_L}{I_D} + 1\right) \approx \frac{KT}{q}\ln\left(\frac{I_L}{I_D}\right). \tag{2.41}$$

Combining eq. 2.37 and 2.38 we obtain $I_D \propto \exp(-E_g)$, such that for a large bandgap dark current decreases enhancing V_{OC} for a given I_L.

Short-circuit current is obtained by applying the condition of zero voltage to eq. 2.40, obtaining

$$I_{SC} = -I_L + I_D\left(\exp\left(-\frac{I_{SC}R_S}{KT}\right) - 1\right) \tag{2.42}$$

where R_{SH} effect has been neglected compared with R_S. For low series resistance I_{SC} equals I_L, typically we assume to be in this regime.

The maximum power (P_m) obtained from a solar cell is given by the product of maximum voltage (V_m) and maximum current (I_m) extracted from the device, obtained by equalising to zero the derivative of the power (P) given by

$$P = IV = I_D V\left[\exp\left(\frac{qV}{KT}\right) - 1\right] - I_L V \tag{2.43}$$

and applying $dP/dV = 0$,

$$I_m = I_D \beta V_m \exp(\beta V_m) \approx I_L \left(1 - \frac{1}{\beta V_m}\right) \tag{2.44}$$

and

$$V_m = \frac{1}{\beta} \ln \left[\frac{\left(\frac{I_L}{I_D}\right)+1}{1+\beta V_m} \right] \approx V_{OC} - \frac{1}{\beta} \ln (1 + \beta V_m) \tag{2.45}$$

where $\beta = q/KT$.

The maximum power obtained from a solar cell is a function of the main photovoltaic parameters, sketched in Figure 2.14, and related by

$$P_m = I_m V_m = FF I_{SC} V_{OC} \approx I_L \left[V_{OC} - \frac{1}{\beta} \ln(1 + \beta V_m) \right] \tag{2.46}$$

where $FF = \frac{I_m V_m}{I_{SC} V_{OC}}$, and the power conversion efficiency (η) is given by,

$$\eta = \frac{P_m}{P_{in}} = \frac{I_m V_m}{P_{in}} = \frac{FF I_{SC} V_{OC}}{P_{in}}. \tag{2.47}$$

Then, to maximize conversion the bandgap needs to be optimized for maximum open-circuit voltage and short-circuit current.

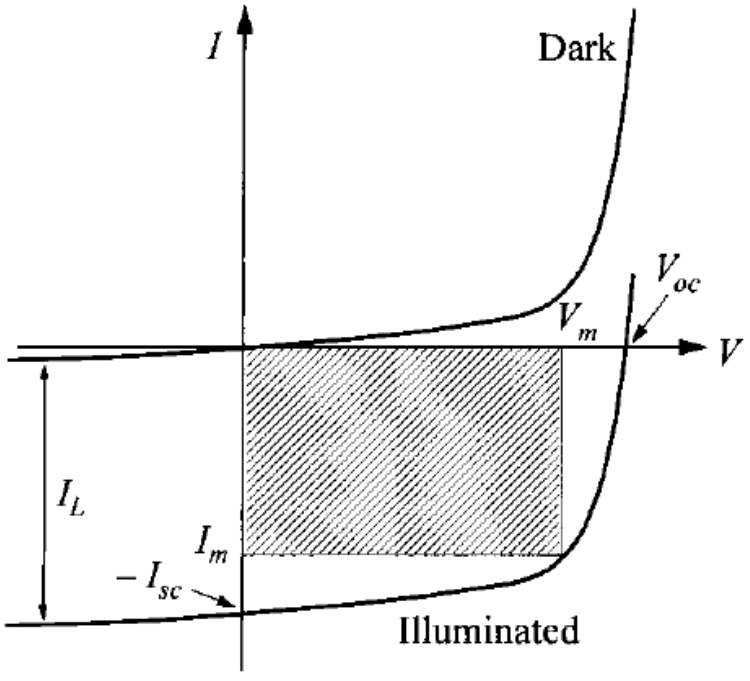

Figure 2.14. Solar cell I-V curve, showing the different photovoltaic parameters: illumination current (I_L), short-circuit current (I_{SC}), and open-circuit voltage (V_{OC}). The shaded area corresponds to the maximum power which can be extracted from the solar cell, given by the product of maximum current (I_m) and maximum voltage (V_m).

The conversion efficiency of a solar cell is the ratio between the maximum power output given by the cell and the power input of the illumination. The standard illumination condition for testing the efficiency of solar cells is the AM1.5 solar spectrum, meaning that sunlight has travelled through a thicker atmosphere of exactly 1/cosθ, where θ (=37°) is the zenith angle of the Sun with respect to the Earth. AM1.5d and the AM1.5g solar spectrum consider only direct light and direct and diffuse light, respectively.

Temperature is an important parameter in solar cells. I_L increases with temperature, due to an increased minority carrier lifetime with temperature. However, both V_{OC} and FF decrease with temperature, resulting in a decrease in power conversion efficiency. V_{OC} decreases as temperature increases, as I_D increases exponentially with temperature. The temperature dependence of the efficiency is especially important under solar concentration (conc), which is commonly used to increase the solar cell efficiency,

$$\eta_{con} = \eta\left(1 + \frac{KT}{q}\frac{\ln(conc)}{V_{OC}}\right) \tag{2.48}$$

Obtained by substituing I_L(1Sun) for *conc* x I_L(conc) in eq. 2.41 and 2.47.

2.4.3 Limiting efficiency in a Single-Junction Solar Cell (SJSC)

The Thermodynamic Limit

The solar cell can be considered as a heat engine, absorbing the heat from the sun and storing it. The stored heat is converted to entropy-less chemical energy stored in e-h pairs, and this conversion is limited by the Carnot efficiency,

$$\eta_{Carnot} = 1 - \frac{T_C}{T_A} \tag{2.49}$$

where T_A and T_C are the temperature of the absorber (the solar cell) and of the surroundings, respectively. Eq. 2.49 assumes 100% conversion from chemical to electrical energy, and assumes that the cell absorbs all the incident sunlight. Taking into account the solid angle (Ω) of the incident sunlight and the emitted emission (radiative recombination) the Carnot efficiency is further reduced. In the case of maximum

concentration, 46500 suns ($\Omega_{inc} = 2\pi$), the upper limit of the thermal efficiency, the so-called Boltzmann efficiency, is given by,

$$\eta_{SC}^{max\ conc} = \left(1 - \frac{T_A^4}{T_S^4}\right)\left(1 - \frac{T_C}{T_A}\right) \tag{2.50}$$

where T_S is the sun´s temperature.

The thermodynamic efficiency limit varies from 67 to 87% depending on the concentrator factor [37, 38, 39, 40].

The Shockley-Queisser limit

Figure 2.15 shows the losses in an ideal *SJSC*, coming mainly from the spectral mismatch between the solar spectrum and the bandgap of the material, and the unavoidable radiative recombination for a cell in thermal equilibrium with the environment, (T_{SC} ~300 K, emitting radiation as stated by Planck's law). Figure 2.15(a) shows sunlight transmission and photogenerated carrier thermalization and recombination, as well as junction and voltage loss. As shown in Figure 2.15(b), thermalization of carriers excited by absorbing a photon with energy $h\upsilon > E_G$ and transmission of photons with $h\upsilon < E_G$ are the two major loss mechanisms reducing the conversion efficiency by ~50%. The detailed balanced principle described for first time by Shockley and Queisser in 1961 [41], refers to the balance between light absorption and radiative recombination in a device. Every microscopic process in a system must be in equilibrium with its reverse process if the system itself is in thermodynamic equilibrium with the environment. Following detailed balance, the open-circuit voltage is limited via radiative recombination (dark current), leading to an upper efficiency of 31% for a bandgap of 1.3 eV. This value can be increased up to 41% for 1.1 eV under maximum sunlight concentration by minimizing Boltzmann loss (increasing the efficiency by 10%) [37]. Solar cells are capable of experimentally achieving efficiencies close to the theoretical limit, i.e. 27.6% for monocrystalline Si cells under 92 suns and 29.1% for monocrystalline GaAs cells under 117 suns.

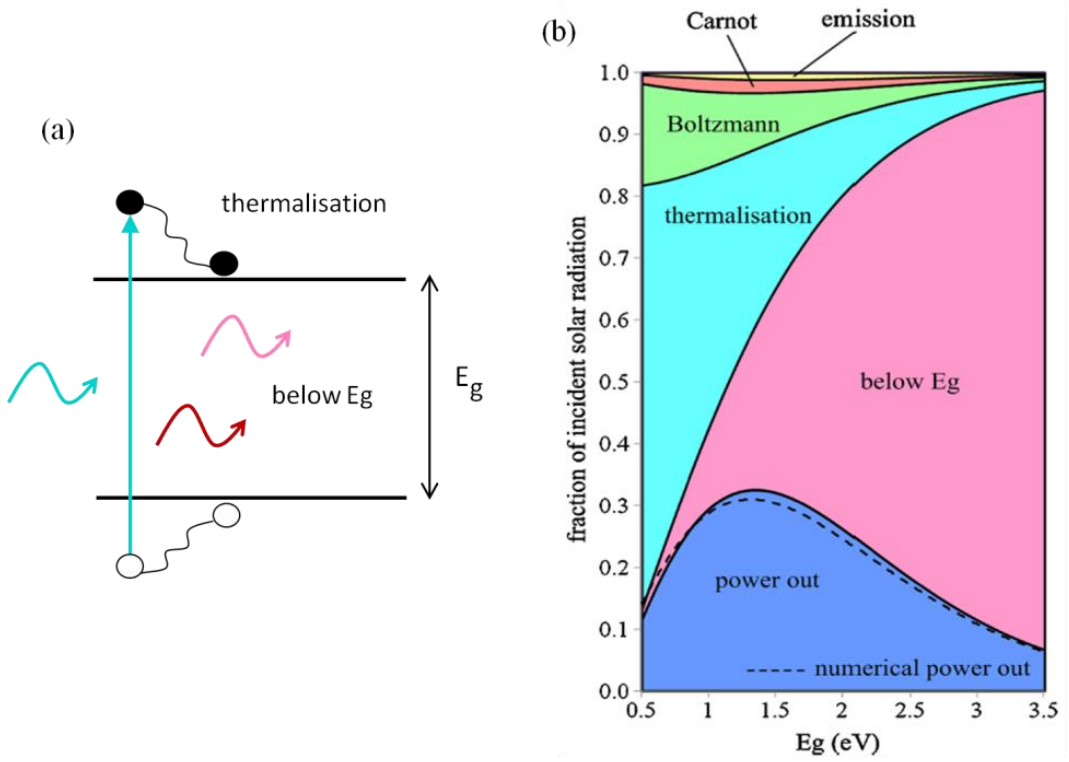

Figure 2.15 Main loss mechanisms in an ideal single-junction solar cell (SJSC). (a) Band structure of a SJSC showing thermalization and transmission losses. (b) Fraction of incident solar vs bandgap energy for a SJSC, showing the different losses mechanism: emission, Carnot, Boltzmann, thermalization and below bandgap. The efficiency for a SJSC is shown by the power out.

2.4.4 Hydrostatic pressure effect on bandgap

When applying high hydrostatic pressure (1000 atm) on a semiconductor, the lattice parameter (a_0) of the crystal decreases by the same amount in all directions, and as a consequence the band structure is modified. From the study of the electrical and optical properties under pressure important properties can be inferred. Typically, under few thousand atmosphere a_0 is reduced by around one per cent. It is important to notice that, by using this technique the dilation of the lattice can be altered without modifying the electron-phonon interaction, and combined with the temperature dependence the phonon contribution can be isolated.

The induced shift under pressure in conduction and valence band given by eq. 2.51, it depends on the pressure coefficient of the material (*PC)* and on the deformation

potential of the conduction and valence band (a_C and a_V, respectively). The conduction band shift (ΔE_C) under a certain range of pressure (ΔP) is given by

$$\Delta E_C = \Delta P \frac{a_C}{a_C + a_V} PC \tag{2.51}$$

where the valence band shift is obtained using the same expression exchanging a_C with a_V. For GaAs and GaSb, a_C is 7.17 and 7.5 meV^{-1}, respectively and a_C is 1.16 and 0.8 meV^{-1}, respectively.

2.5 Intermediate Band Solar Cell (IBSC)

Different approaches have been suggested to overcome the efficiency limit of single junction solar cell (SJSC), represented by the third generation of solar cells. This thesis is focussed on the intermediate band solar cell (IBSC) approach. As shown in Figure 2.17(a), in an IBSC apart from CB-VB transitions there are other two sub-bandgap transitions between VB-IB and IB-CB, generating two-photon photocurrent via an intermediate band (IB) producing photocurrent without modifying the open-circuit voltage. Two-photon photocurrent (TPPC) is produced by firstly absorbing a photon with energy close to $E_{VB\text{-}IB}$ creating a hole in the VB and an electron in the IB, and secondly by absorbing a second photon with energy close to $E_{IB\text{-}CB}$ generating a hole in the IB and an electron in the conduction band. In an IBSC transmission loss is reduced by absorbing sub-bandgap photons, achieving a maximum theoretical efficiency of 63% for a bandgap of 1.93 eV and a transition energy CB-IB of 0.7 eV (under maximum light concentration), which is more than 20% larger than in the SJSC. To achieve IB behaviour in a structure exhibiting TPPC and V_{OC} preservation (IBSC has the same V_{OC} as the equivalent SJSC without IB), three specific conditions must be fulfilled: three separate Fermi levels so that the intermediate band is de-coupled from the valence bad and conduction band preserving V_{OC}, an IB partially filled with holes maximizing the two-photon absorption, and overlapping of the absorption coefficient of each transition ($E_{VB\text{-}IB}$, $E_{IB\text{-}CB}$ and $E_{VB\text{-}CB}$) allowing high TPPC. Figure 2.16(a) shows a sketch of an

ideal IBSC with the three separate Fermi levels and the three optical transitions. QDs sandwiched between the base and emitter of a solar cell are the best candidates for implementing IBSC. Figure 2.16(b) shows the typical structure of a quantum dot solar cell.

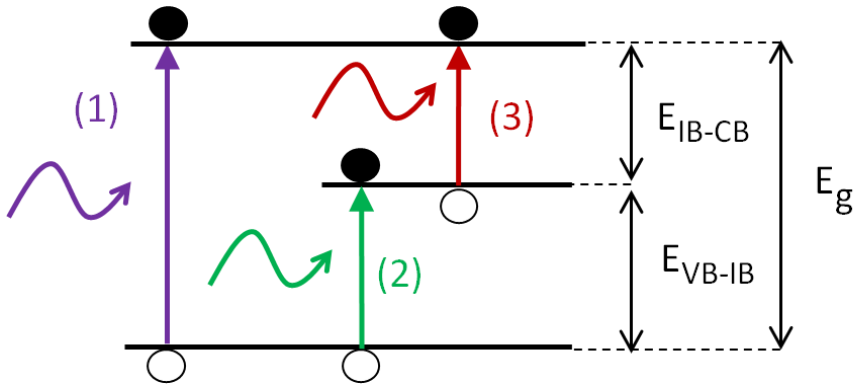

Figure 2.16. In an intermediate band solar cell carriers are photo-generated from valence to conduction band (1) ($h\upsilon \geq E_g$), from valence to intermediate band (2) ($E_g \geq h\upsilon \geq E_{VB-IB}$), and from intermediate to conduction band (3) ($E_{VB-IB} \geq h\upsilon \geq E_{IB-CB}$).

Chapter 3

Literature review

In this chapter multi-junction and intermediate band solar cells are reviewed, summarising the main achievements and limitations of both approaches. The third generation aims for low cost and high efficiency solar cells, surpassing the efficiency limit of a SJSC (41% under maximum concentration) [8], but it is still limited by the thermodynamic efficiency limit (87% under maximum concentration) [42], as shown in section 2.4.3 in *Background Theory* chapter.

3.1 Multi-Junction Solar Cell (MJSC)

The single-crystal III-V multi-junction solar cell (MJSC) holds the efficiency record for solar cells [10]. The devices are generally grown by Metal Organic Vapour Phase Epitaxy (MOVPE), limiting this technology to concentrator systems to reduce the high cost of substrates and epitaxy. III-V semiconductors allow bandgap flexibility for matching the solar spectrum (Figure 3.1(a)), and epitaxial growth ensures high crystal quality if the layers are lattice matched. MJSC are typically lattice matched to Ge (lattice constant of ~ 5.66 Å). Figure 3.1(b) shows the InGaP/(In)GaAs/Ge triple-junction solar cell which is well matched to the solar spectrum, with an efficiency of 31% [43], which is the highest among the lattice matched MJSC.

Metamorphic growth is an alternative to lattice matched growth, allowing materials with different lattice parameters to be grown on top of each other, increasing the flexibility of material combinations and the number of junctions within the cell. By using metamorphic growth the cell spectral absorption matches better the solar spectrum, increasing further the efficiency.

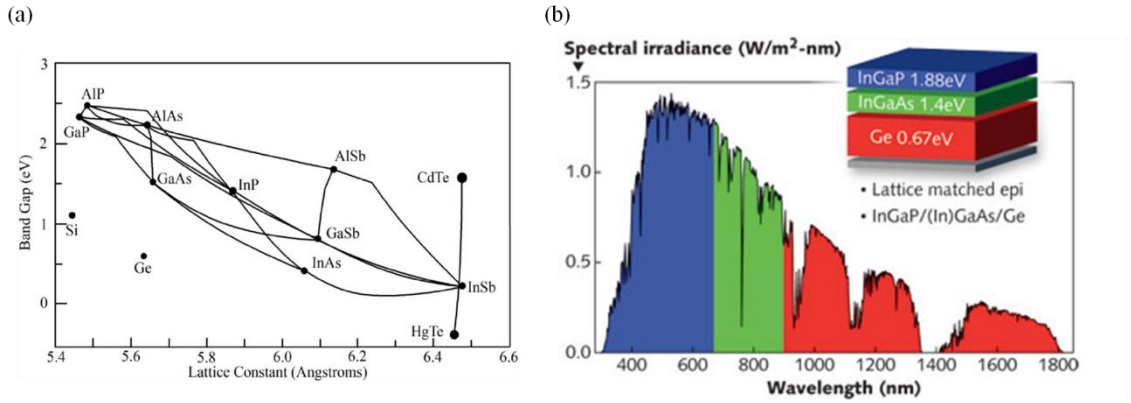

Figure 3.1. (a) Bandgap against lattice constant. (b) Spectral irradiance under the AM1.5d solar spectrum for the triple multi-junction cell InGaP/(In)GaAs/Ge, each cell absorbs a different part of the solar spectrum [43].

Even though crystal quality is degraded due to dislocations, the metamorphic triple-junction GaInP/GaInAs/Ge cell has achieved an efficiency of 40.7% under 240 suns [44], being the first device to exceed an efficiency of 40%. However, metamorphic growth is limited by the maximum strain that can be accommodated within the lattice.

The development of wafer bonding technology has offered the opportunity to combine mismatched materials through a permanent, electrically conductive and optically transparent interface. Figure 3.2 shows the four-junction cell GaInP/GaAs/GaInAsP/GaInAs with an efficiency of 44.7% under 297 suns concentration [45]. The top cell, grown lattice matched to the GaAs substrate, was wafer bonded to the bottom cell, grown lattice matched to the InP substrate. The same cell was measured in 2016 under 508 suns, producing the world record for solar cell efficiency at 46% [10].

3.2 Intermediate Band Solar Cells (IBSC)

Intermediate band solar cell (IBSC) devices have been extensively studied, using structures based on quantum dots, impurity levels, and highly mismatched materials [16, 46]. In fact, deep centre levels in the band gap were the first system suggested to study IB behaviour.

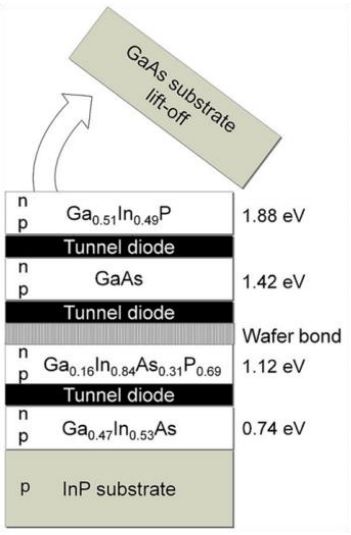

Figure 3.2. Metamorphic growth and wafer bonding have allowed the design of the four-junction solar cell GaInP/GaAs/GaInAsP/GaInAs. [45]

This approach requires adding impurities to the semiconductor with energy levels close to the middle of the bandgap. However, in this situation SRH is enhanced [47, 48] and electron wavefunctions need to be delocalized forming a miniband to inhibit non-radiative recombination [49]. Lifetime measurements on Ti- and S- implanted silicon wafers support this theory. However, the band anti-crossing (BAC) concept provides a better alternative for forming an IB [50, 51] in highly mismatched alloy materials [52], by adding N or O in the semiconductor lattice. The formation of the band is the result of the interaction between the localised states of the N and O atoms mixing with the CB states of the material, and it has proven IB behaviour. For example, in GaNAs electronic transitions from IB to CB have been identified [52], and in n-doped GaNPAs layers, photoreflectance measurements show IB absorption [53], while open-circuit voltage has been improved in ZnTe solar cells and ZnTeO IBSC using an n-ZnS window layer [54]. Incorporating quantum dots (QDs) in the active region of the p-i-n solar cell is considered one of the most promising candidates for implementing intermediate band (IB) behaviour [16, 55, 56]. The III-V semiconductor QDs grow by self-assembly using MBE or MOVPE, such that the ground state of the multiple confined energy levels of the nanostructure acts as the IB. As explained in *Background Theory* chapter (section

2.5), the QD ground state must fulfil specific conditions to work as an IBSC to boost the efficiency over the SJSC efficiency limit. The requirements are; (i) to have three un-coupled Fermi levels [57], meaning that the IB must be thermally decoupled from CB and VB, (ii) it must be partially filled with electrons so that E_{FI} lays in the middle of it [58], and (iii) the absorption spectra of the three transitions (VB-CB, VB-IB and IB-CB) must not overlap. When quantum dot solar cells (QDSC) fulfil these conditions, they may generate two-photon photocurrent (TPPC), while still conserving the open-circuit voltage (V_{OC}) of the reference cell without QDs – the two so-called IBSC working principles.

In the following subsections, type-I and type-II QDSC are reviewed. The focus is on the sub-bandgap light absorption, the photovoltaic performance of the cell (J_{SC}, V_{OC} and η), and the two working principles of the IBSC.

3.2.1 Type-I Quantum Dot Solar Cell (QDSC)

The most common system to study as an IBSC is the type-I In(Ga)As/GaAs QD. Figure 3.3(a) shows a high density InAs/GaAs QD crystal superlattice sandwiched between n- and p-layers of a GaAs SC. Figure 3.3(b) exhibits the corresponding band structure with the three possible optical transitions (E_G, $E_{VB\text{-}IB}$ and $E_{IB\text{-}CB}$) and Fermi levels for the three bands (VB, IB and CB). [16]

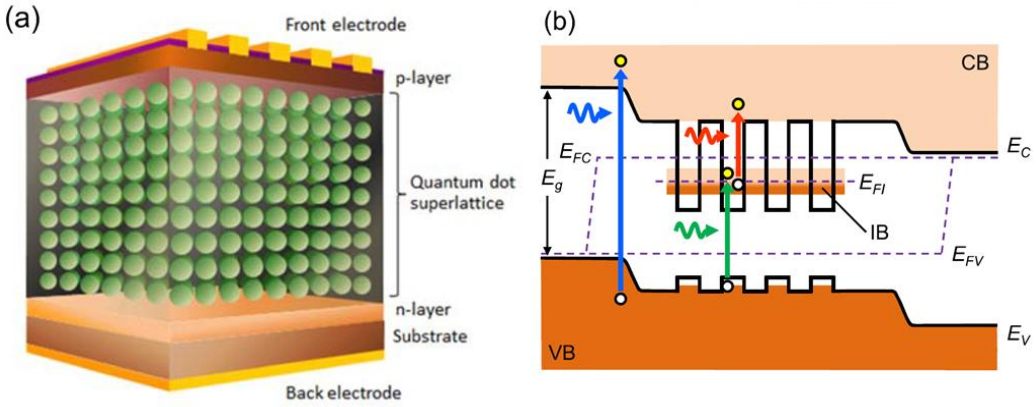

Figure 3.3. (a) Sketch of a type-I InAs/GaAs high density quantum dot superlattice sandwiched between the p- and n- layers of a GaAs SC. (b) The band structure of the p-n junction of the QD superlattice device. The VB is full of electrons (dark orange) while the CB is empty (light orange) and the IB is half-filled with electrons. [16]

Sub-bandgap light absorption, short-circuit current and open-circuit voltage

Figure 3.4(a) shows the InAs/GaAs QDSC with 10 QD layers doped with Si for achieving a partially filled *IB* exhibiting sub-bandgap absorption. However, sub-bandgap photocurrent is a few orders of magnitude lower than supra-bandgap current from the GaAs bulk, without increasing short-circuit current noticeably. Furthermore, by adding QDs into the matrix, the open-circuit voltage is degraded, limiting the conversion efficiency of the QD-IBSC (Figure 3.4(b)). *Low QD absorption* (not enough photogerenated carriers) is identified as the main limitation resulting in low sub-bandgap photoresponse, meanwhile *fast carrier capture* (QD thermally coupled with CB) is responsible for the low output voltage in such systems.

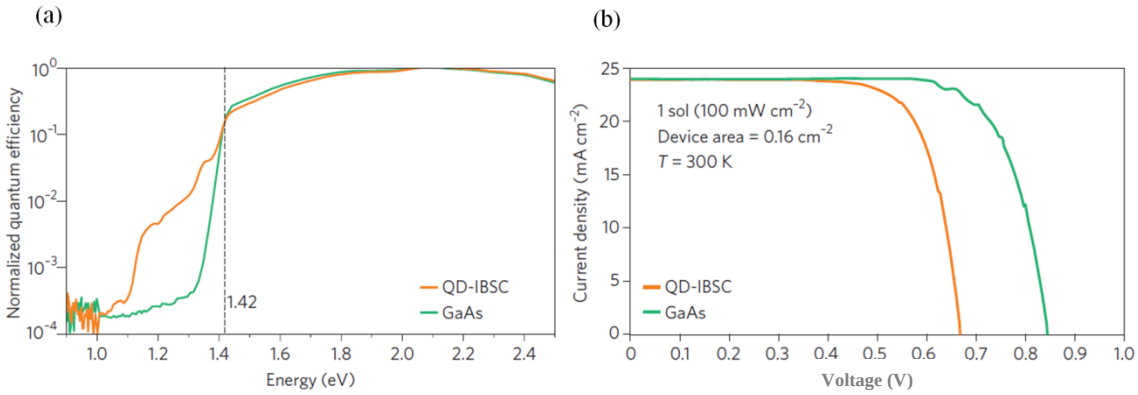

Figure 3.4. Electrical characterization for InAs/GaAs QD-IBSC (orange) with Si doping and the GaAs reference solar cell (green) measured at room temperature. (a) Normalized quantum efficiency, below the GaAs bandgap at 1.42 eV (dotted line) just the QD-IBSC produces photocurrent. (b) J-V curve under 1 Sun illumination (100 mW/cm^2), showing similar short-circuit current for both cells and a reduction in open-circuit voltage for QD-IBSC compared with the GaAs SC [59].

QD absorption can be increased by further increasing the QD density or by building SC containing more QD stacks. The typical QD area density for the self-assembled SK growth technique is ~1x10^{10} cm^{-2}, however ideally a much larger density is required to increase sub-bandgap optical absorption. Yamaguchi et. al. succeeded in increasing QD density up to 1x10^{12}cm^{-2} by adding Sb during InAs QD growth [60, 61, 62]. The number of QD layers within the device is ultimately limited by the maximum strain accumulated in the structure before the formation of dislocations and defects. Different techniques

have been developed to overcome this problem by preventing material quality degradation, based on adding strain compensation or balancing layers (SCL or SBL). Alternatively, a different material composition with large critical thickness can be used allowing a high number of stack layers. For example, the ultra-high density stack based on $In_{0.4}Ga_{0.6}As$/GaAs QD, contains 400 QD layers and exhibits a high crystalline quality using thick spacers [63]. Increasing the QD layers from 10 to 150 enhances solar cell quantum efficiency and short-circuit current. Sub-bandgap quantum efficiency is improved from 10 up to 70%, as shown in Figure 3.5(a) and short-circuit current is increased from 17.5 up to 23.6 mA/cm^2. However, open-circuit voltage is reduced from 0.88 to 0.62 V, unfortunately decreasing the conversion efficiency from 12.4 to 9.2%, as shown in Figure 3.5(b).

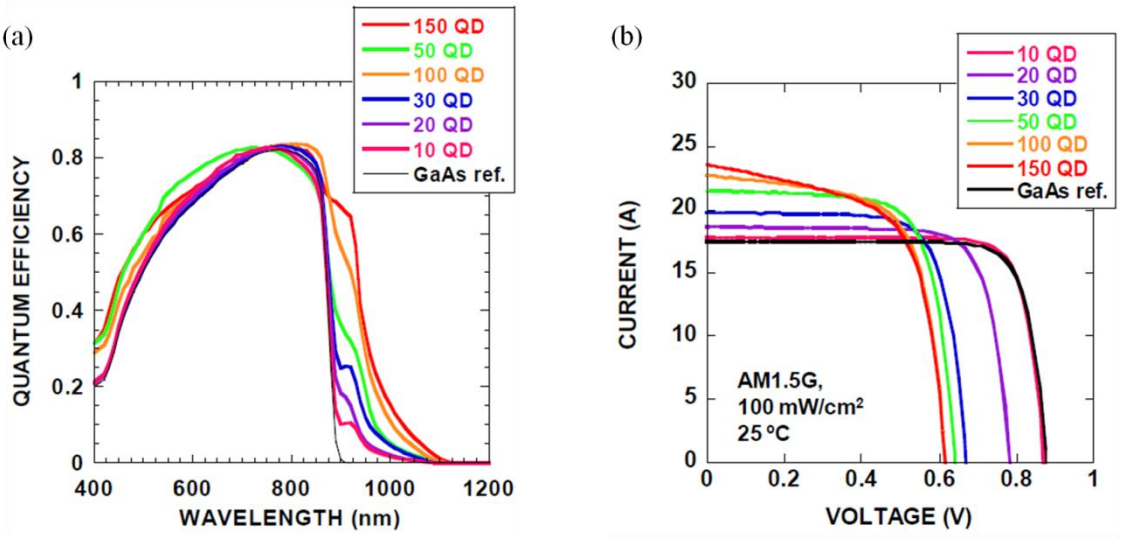

Figure 3.5. Solar cell characterization at room temperature for GaAs reference cell (black) and type-I InAs/GaAs QDSC with increasing number of QD layers: 10 (pink), 20 (purple), 30 (blue), 50 (green), 100 (orange) and 150 (red). (a) Quantum efficiency vs wavelength. (b) I-V curve under AM1.5g solar spectrum. [63]

By using a GaP SCL between the InAs/GaAs QD layers (5 QD layers) the efficiency can be improved from 3.7 to 10.8% (reference cell´s efficiency is 14.7%) [64]. Also, by using GaP SBL and reducing InAs QD coverage in InAs/GaAs QDSC (10 QD layers), V_{OC} increases from 0.880 to 0.994 V (reference´s value is 1.041 V), and J_{SC} enhances by 3.5% with respect to the reference cell (Figure 3.6(a)) [65, 66].

A different approach consists of highly dense packed InGaAs/GaAs QDSC, with a high QD density of $5x10^{11}cm^2$ [67]. Due to the small spacing (10 nm) between consecutive QD layers strain builds up in the structure producing vertical alignment (columns) of QD. This type of QDSC exhibits J_{SC} as high as 27.66 mA/cm^2 resulting in an efficiency of 18.3%. The high performance of this system is attributed to a reduction in non-radiative recombination centres and an improvement in photocarrier extraction due to the miniband formation in the array of vertically coupled QDs [68].

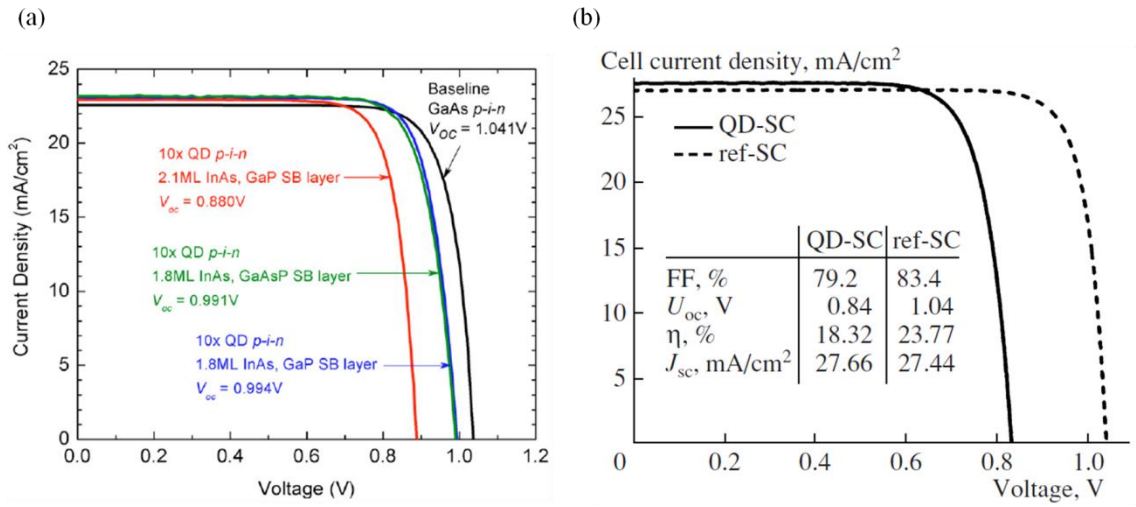

Figure 3.6. Current density vs voltage under AM1.5g solar spectrum. (a) For GaAs p-i-n (black) and InAs/GaAs QDSC (10 layers) with 2.1 ML of In coverage and GaP strain balance layer (SBL) (red), 1.8 ML of In coverage and GaAsP SBL (green), and 1.8 ML of In coverage with GaP SBL (blue). [65, 66] (b) Highly dense packed vertically aligned (columns) of InGaAs/GaAs QDSC (solid line) and reference GaAs SC (dotted line), photovoltaic parameters from both cells are presented in the inset. [68]

By means of increasing QD density and QD layers sub-bandgap quantum efficiency is enhanced boosting short-circuit current. However, open-circuit voltage reduction from the reference value limits solar cell efficiency. The drop in open-circuit voltage is caused mainly by non-radiative/radiative recombination and thermal escape of electrons from the QD ground state to the CB. To decouple the electronic population of the QDs from the CB an InAlGaAs strain relief layer (SRL) is introduced [69], isolating the QD ground state from the CB and consequently increasing the activation energy from 115 to 224 meV by reducing the wetting layer (WL) potential. A thin WL is formed during SK QD growth prior to QD nucleation. However, the WL introduces a continuum of states

between the CB and the QD states acting as a route for electrons to escape from the QDs to the CB. To improve the open-circuit voltage, the thermal escape of electrons from QD to WL and from QD to CB needs to be suppressed.

The two IBSC working principles: TPPC and V_{OC} recovery

Direct evidence of two-photon photocurrent (TPPC) in InAs/GaAs IBSC has been demonstrated at low temperature [70, 71, 72], using two light sources to pump the electron from VB to IB and then from IB to CB. Datas et. al. measured the broadest TPPC spectrum in type-I QDSC at low temperature in InAs/AlGaAs QDSC, as shown in Figure 3.7 [73]. TPPC is not observed at room temperature due to high thermal carrier escape from QD to CB, so that thermionic emission dominates over optical generation. Different systems like GaAs/AlGaAs also show TPPC when cooled down [74] and in some cases, by adding N thermal escape is inhibited allowing TPPC to be detected at room temperature [75].

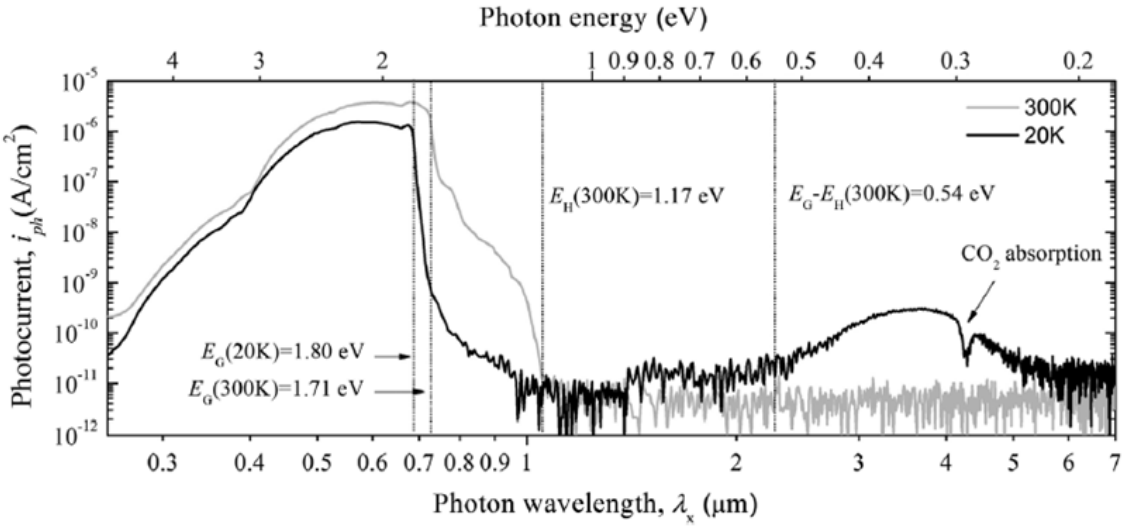

Figure 3.7. Photocurrent extracted from the InAs/AlGaAs QDSC as function of the wavelength of the primary light source at 300 K (grey) and 20 K (black) pumping electrons from QD to CB, while the secondary light source pumps electrons from VB to QD. [73]

V_{OC} recovery has been probed in QD-IBSC under extreme conditions capable of reducing both the high thermal escape rate and inhibiting the fast QD recombination rate. Sakamoto et. al. and Tobias et. al. calculated the sunlight concentration required to overcome QD recombination for a typical QD density of $1x10^{10}$ cm^{-2} (E_{IB-CB} ~ 0.2 eV)

assuming an optical cross-section of $3x10^{-14}$ cm^2 for VB-QD and QD-CB transitions [76, 77]. The results show that under 1000 suns optical generation (pumping electrons from QD to CB) overcomes QD recombination (electrons in QD recombining with holes in VB). Experimentally, full V_{OC} recovery is achieved in InAs/GaAs QDSC at low temperature and under high light concentration [18, 78]. Figure 3.8(a) and (b) shows the J_L-V_{OC} curves measured under different light concentration for a QD-IBSC and a GaAs reference cell at 150 and 20 K, respectively. At 20 K (Fig. 3.8(b)) under 1000 suns, V_{OC} is as high as 1.506 V for the QD-IBSC, which is close to the GaAs bandgap, fully recovering V_{OC} to the reference value.

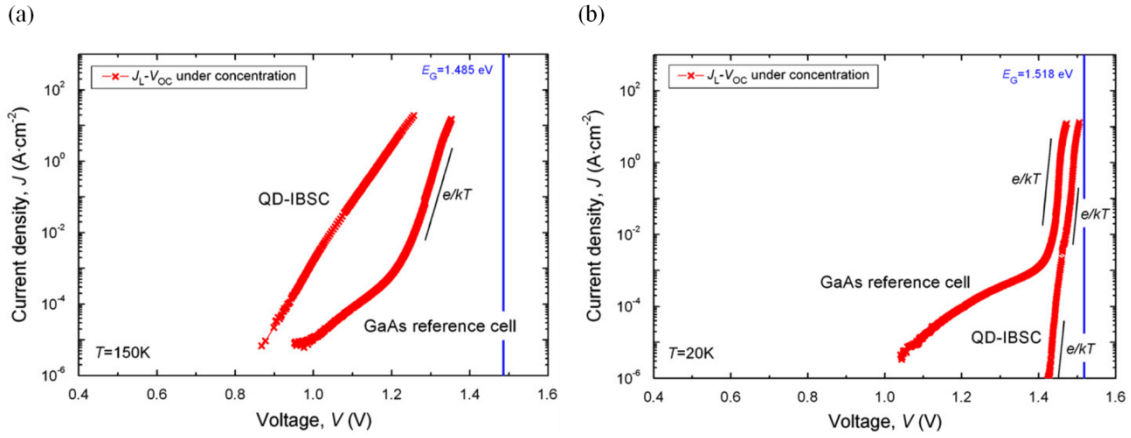

Figure 3.8. J_L-V_{OC} curves under light concentration up to 1000 suns, for a QD-IBSC and a GaAs reference cell. (a) At 150 K both cells exhibit V_{OC} lower than bandgap energy, while the reference cell exhibits a larger V_{OC} than the QD-IBSC. (b) At 20 K, the QD-IBSC reaches the reference, achieving values close to the bandgap. [18]

Summary

QDSC present poor sub-bandgap absorption and high QD recombination rate (short carrier lifetime), limiting short-circuit current and reducing open-circuit voltage. Non-effective decoupling between the QDs and the CB causes high thermal carrier escape, which dominates over optical generation and limits IB behaviour at room temperature in QDSC. The main challenges and limitations in type-I QDSC are summarised in table 3.1.

Table 3.1. Comparison between ideal SJ, ideal IB and type-I QD, showing the challenges and solutions to achieve IB behaviour. The maximum efficiency is calculated under maximum sunlight concentration of 46,500 suns. (GS means ground state)

	SJSC	*IBSC*	*Type-I QDSC*	*Challenges*	*Solutions*
$V_{OC} \approx E_G$	✓	✓	x	Thermal coupling between QD-CB & QD recombination	Low T/ increase QD GS confinement & minimize QD recombination
Sub-bandgap & two-photon photocurrent	x	✓	x	Low sub-bandgap absorption & short carrier lifetime	High densely packed QDSC & type-II QD
η_{MAX} *(%)*	41	63	x	Low efficiency	High efficiency

The main achievements in type-I QD-IBSC to date in In(Ga,Al)As/(Al)GaAs are:

- $1x10^{12}$ cm^{-2} QD area density [61] by adding Sb, and 400 layer ultra-high density stacks in InGaAs/GaAs QDSC [63]
- Largest V_{OC} = 0.994 V, with J_{SC} = 23.3 mA/cm^2, FF = 0.8, and efficiency = 13.5 % (AMd 1.5 spectrum) at room temperature – achieved by reducing In coverage in InAs QDs and by adding GaP strain balance layer [65]
- Highest J_{SC} = 27.66 mA/cm^2 and highest efficiency = 18.3 %, with V_{OC} = 0.84 V, FF = 0.792 – achieved by vertical stacking (columnar) InGaAs/GaAs QDs [67]
- Full V_{OC} recovery, reaching 1.506 V close to the bandgap in InAs/GaAs QDSC at 20 K under 1000 suns [18]
- *TPPC* detected using two light sources at 20 K in InAs/GaAs QDSC [73] and at 300 K by adding N to InAs QDs [75]

3.2.2 Type-II Quantum Dot and Quantum Ring Solar Cell (QD/QRSC)

In 2002, Cuadra et. al. proposed implementing type-II QD as an alternative to type-I QD in IBSC [19]. In type-II band alignment the lower wavefunction overlap of holes and electrons can reduce thermal carrier escape and capture processes improving IB behaviour. The long carrier lifetime of type-II QD reduces the QD recombination rate, improving carrier extraction and enhancing J_{SC} and V_{OC} [20, 79]. Figure 3.9(a) shows

the enhancement of carrier lifetime in type-II compared with type-I. For InAs QDs embedded in GaAsSb, the type-II QDs exhibit a carrier lifetime as long as 220 nm. Type-II alignment also reduces the valence band offset (VBO) compared with type-I, increasing the effective band gap ($E_{G,eff}$) of the material, as shown in Figure 3.9(b) [80]. Since 1999, type-II GaSb/GaAs nanostructures have been grown using SK growth, which resulted in the formation of GaSb quantum dots and quantum rings (QR) [81, 82, 83, 84, 85]. Type-II GaSb/GaAs quantum ring solar cells (QRSC) were subsequently developed in 2012 [21]. Since then, different groups have studied IB behaviour in these devices, especially Michigan University together with Universidad Politecnica de Madrid (UPM) [86, 87, 88, 89, 90, 20, 91], and Lancaster University together with Nelson Mandela Metropolitan University [21, 92, 93, 94, 95]. The main findings are briefly considered below.

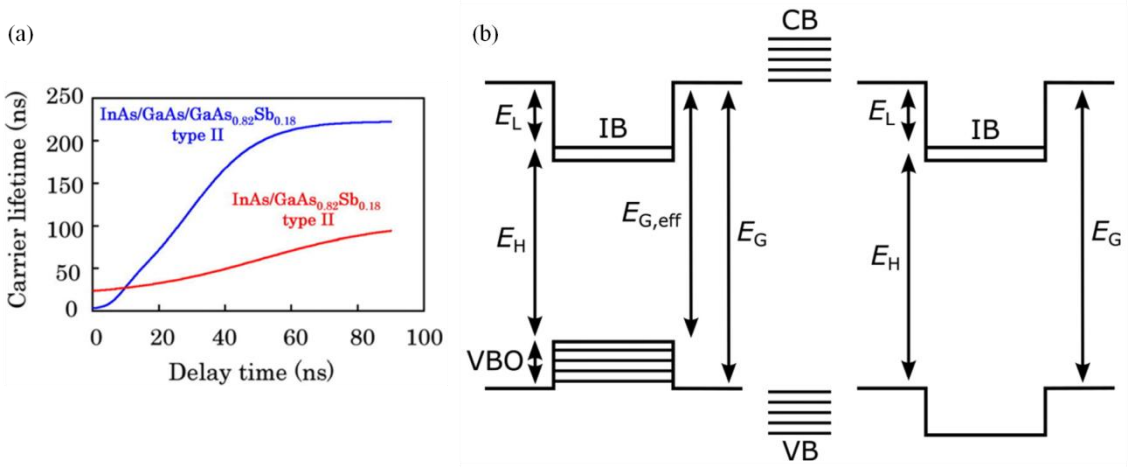

Figure 3.9. (a) Carrier lifetime as a function of delay time, for two type-II structures $InAs/GaAs_{0.82}Sb_{0.18}$ (red) and $InAs/GaAs/GaAs_{0.82}Sb_{0.18}$ (blue) with a maximum of 100 and 200 ns lifetime, respectively [79]. (b) Type-I (left) and type-II (right) band alignment for electrons. VBO in type-I reduces the bandgap, E_G, resulting in an effective bandgap, $E_{G,eff}$ [87].

Y. Shoji et. al. from Tokyo University have compared the performance of a QDSC vs a QRSC based on type-II GaSb/GaAs system designing two solar cells with the same structure one with a QD stack an another one with a QR stack as shown in Figure 3.10 [96]. Their study shows higher photoluminescence intensity and higher room temperature external quantum efficiency for QRSC, indicating the superior crystal

quality of QR compared with QD. Also, low temperature two-photon photocurrent measurement suggest that in QR structures two-photon absorption is more dominant for carrier extraction than QD shape.

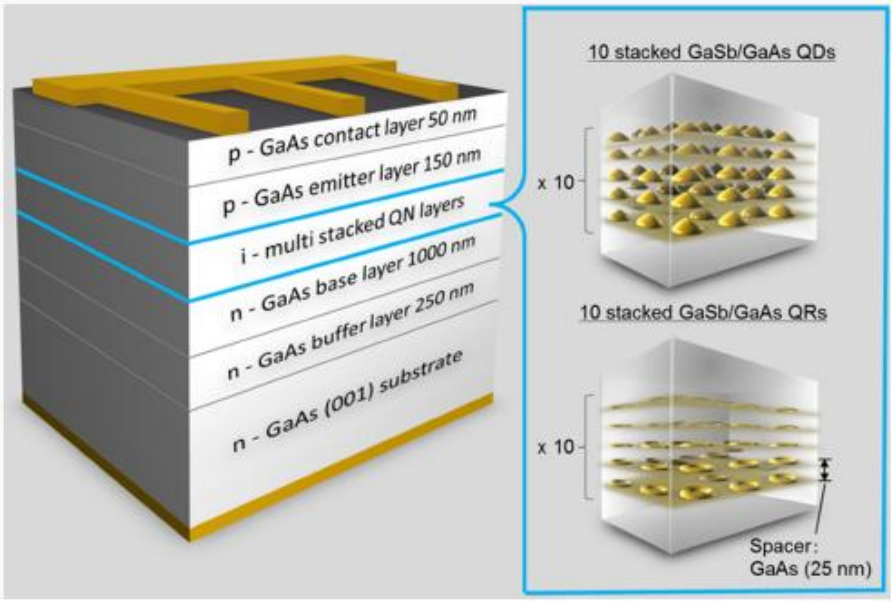

Figure 3.10. Solar cell based on a p-i-n junction with 10 stacked GaSb/GaAs quantum dots (QD) and quantum rings (QD) grown in the intrinsic layer [96].

Sub-bandgap light absorption, J_{SC} and V_{OC}

Figure 3.11(a) shows sub-bandgap photocurrent in the EQE of GaSb/GaAs QRSC from 900 to 1400 nm, corresponding to transitions from the QR energy levels to the CB. However, the low QR absorption results in a low external quantum efficiency (EQE) between 0.001 - 0.1 %. By increasing the number of GaSb/GaAs QR layers, the sub-bandgap light absorption and total photocurrent are enhanced. As shown in Figure 3.11(b), by adding 10 QR layers to the SC without using strain balance techniques, J_{SC} increases from 26.4 to 27.9 mA/cm^2. This is the highest value reported for J_{SC} in QD-IBSC, showing the superior characteristics of type-II compared with type-I [67]. However, the V_{OC} reduction in QD-IBSC is even higher for type-II compared with type-I cells [21]. Hole trapping has been identified as the main reason for the low V_{OC} in type-II devices, because photogenerated holes in the n-region (base) of the cell are

trapped in QR, while in transit across the intrinsic region, when drifting to the p-region (emitter), therefore decreasing the supra-bandgap EQE [21].

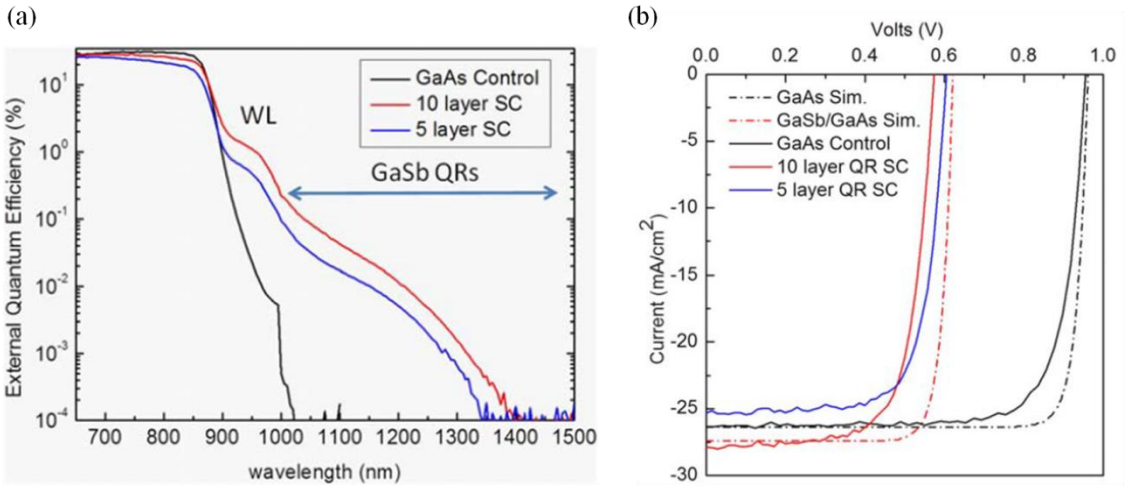

Figure 3.11. (a) External Quantum Efficiency vs wavelength for GaAs reference cell (black), 10 GaSb/GaAs QR stack SC (red) and 5 GaSb/GaAs QR stack SC (blue). From 850 to 1400 nm, QRSC exhibit WL and GaSb QR absorption. By increasing the number of QR layers from 5 to 10 the sub-bandgap photocurrent is enhanced. (b) Current density vs voltage measured under AM1.5g solar spectrum - experimental data (solid lines) and simulation (dotted lines), GaAs reference cell (black), 10 GaSb/GaAs QR stack SC (red) and 5 GaSb/GaAs QR stack SC (blue). The 10 QD layer QRSC exhibits a larger J_{SC} than the reference cell, however V_{OC} is reduced. [21]

For a better understanding of carrier dynamics in QRSC H. Fujita et. al. studied J_{SC} under different power intensities, temperatures and bias voltages [94]. The diagram in Figure 3.12(a) shows the different mechanisms involved in pumping electrons from QR to CB (photo-excitation), and removing holes from QR to VB (tunnelling, thermionic emission, and photo-excitation). Figure 3.12(b) reveals sub-bandgap photocurrent dominated by hole thermionic emission for temperatures above 100 K, and by tunnelling and photo-excitation for temperatures below 100 K. Hole thermal escape prevents conservation of V_{OC} due to thermal coupling between the QR and the VB.

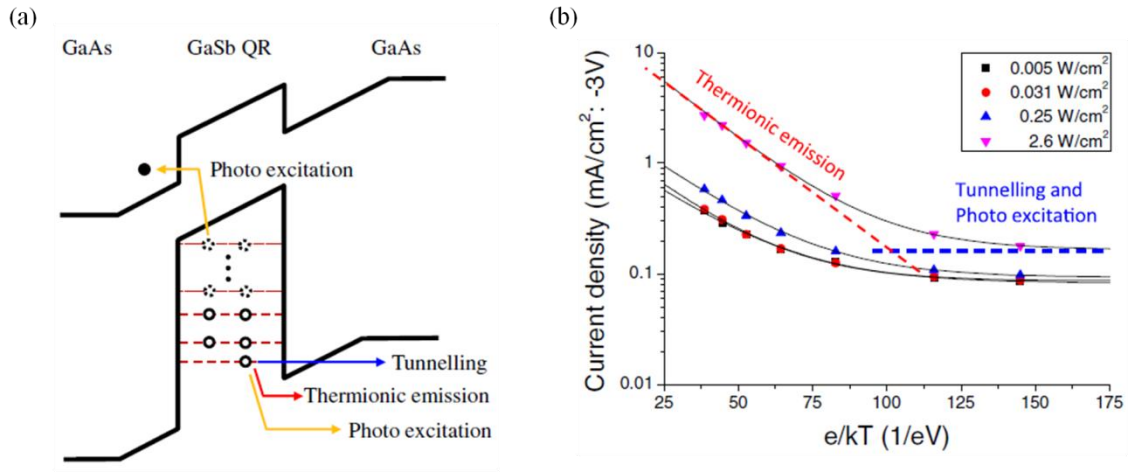

Figure 3.12. (a) Carrier dynamics in QRSC. An electron in a QR can be photo-excited to the CB, and confined holes in the QR can escape to the VB via tunnelling, thermionic emission and photo-excitation. (b) Arrhenius plot of current density under a bias of -3 V for a GaSb/GaAs QRSC. The cell was measured under different laser power (λ_{laser} = 1064 nm): 0.005 W/cm^2 (black square), 0.031 W/cm^2 (red circle), 0.25 W/cm^2 (up blue triangle), 2.6 W/cm^2 (down pink triangle). At low temperature tunnelling and photoexcitation dominates, and above 100 K thermionic emission is the main carrier escape mechanism. [94]

The two IBSC principles: TPPC and V_{OC} recovery

GaSb/GaAs type-II QDSC and QRSC have successfully demonstrated IB behaviour, as shown in Figure 3.13(a) probing TPPC using two light sources measured at 9 K [86, 87, 90, 97]. E_H and E_L correspond to transitions QD → CB and QD → VB, respectively. From EQE and electroluminescence spectra E_H and E_L are identified as 1.02 eV and 0.49 eV, respectively, in agreement with literature values [93, 98]. In type-II QDSC, TPPC is achieved by firstly absorbing a photon from the primary source, pumping holes from QD to VB, and secondly absorbing a photon from the secondary source, to pump electrons from QDs to the CB (photofilling QD with holes). In the absence of a secondary source, non-radiative mechanisms such as thermalization, tunnelling or impact ionization promote electrons from the QDs to the CB (producing EQE for energies smaller than E_L). Figure 3.13(b) shows the increase in EQE for photon energies close to E_L under two photon illumination (EQE_{2ph}) compared with one photon illumination (EQE_{1ph}). The ratio between the two is as high as 1000, revealing the huge potential of GaSb/GaAs QDSC in producing TPPC by photofilling QD energy levels

with holes (under secondary source illumination), fulfilling the first of the two working principles of an IBSC.

Compared with type-I QDSC, TPPC has been observed in $In_{0.4}Ga_{0.6}As$ QDs embedded in GaAsSb layers (type-II) and GaAs (type-I), showing larger TPPC for type-II as a consequence of the increased carrier lifetime in type-II alignment [99].

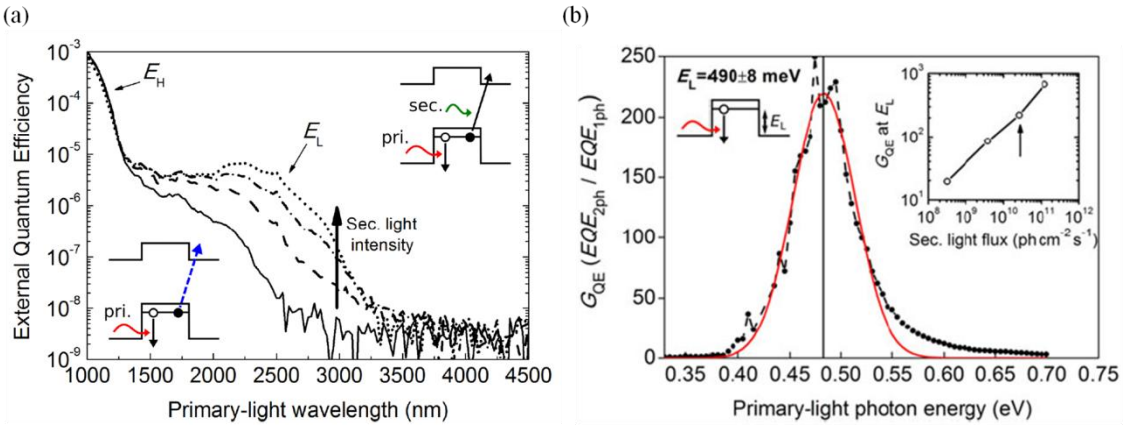

Figure 3.13. Two-photon photocurrent measured at 9 K for type-II GaSb/GaAs QDSC. (a) External Quantum Efficiency (EQE) vs primary-light wavelength, as the intensity of the secondary light is increased. The inset shows secondary light (green arrow), primary light (red arrow), and non-radiative mechanisms (blue dotted line). (b) Ratio of EQE under two photons and under one photon illumination. For an energy E_L (QD-VB) of 0.49 eV, the ratio is 200. The inset shows a maximum ratio of 1000. [86]

In order to achieve high efficiency IBSC devices at room temperature, optical generation process must dominate over thermal emission, producing high TPPC while preserving the *Voc* of the reference cell. Figure 3.14(a) shows the optical and thermionic emission rate for different solar concentrations (Φ) in GaSb/GaAs QDSC, using an optical cross-section (σ_{op}) of $2x10^{-13}$ cm^2, assumed to be similar to those in Ge and Si QDs, and a thermal hole capture cross-section, σ_h = $2x10^{-16}$ cm^2 measured in GaSb/GaAs QDSC [20]. From the emission rate values at room temperature, $e_{op} = \Phi\sigma_{op}$ and photogeneration overcomes thermal processes when the emission rate $e_h = 3x10^7$ s^{-1}, i.e. above 1000 suns illumination. Under high solar concentration, the high optical emission rate is expected to compensate for the high thermal escape. Figure 3.14(b) shows partial V_{OC} recovery at room temperature in GaSb/GaAs QRSC, achieving 0.916

V under 2,500 suns [95]. Full V_{OC} recovery was expected at this concentration following Hwang et. al. work [20], however thermal escape was underestimated and optical generation overestimated. At high concentration the ideality factor (*n*) - obtained from V_{OC} versus concentration - was 1.0 and 1.6 for the reference cell and the GaSb/GaAs QRSC respectively. Therefore, the reference cell was limited by radiative band-to-band recombination and the QRSC was limited by a combination of SRH and band-to-band processes. By extrapolating the curve, full *Voc* recovery is expected at higher solar concentration, consistent with the second of the two principles of IBSC operation.

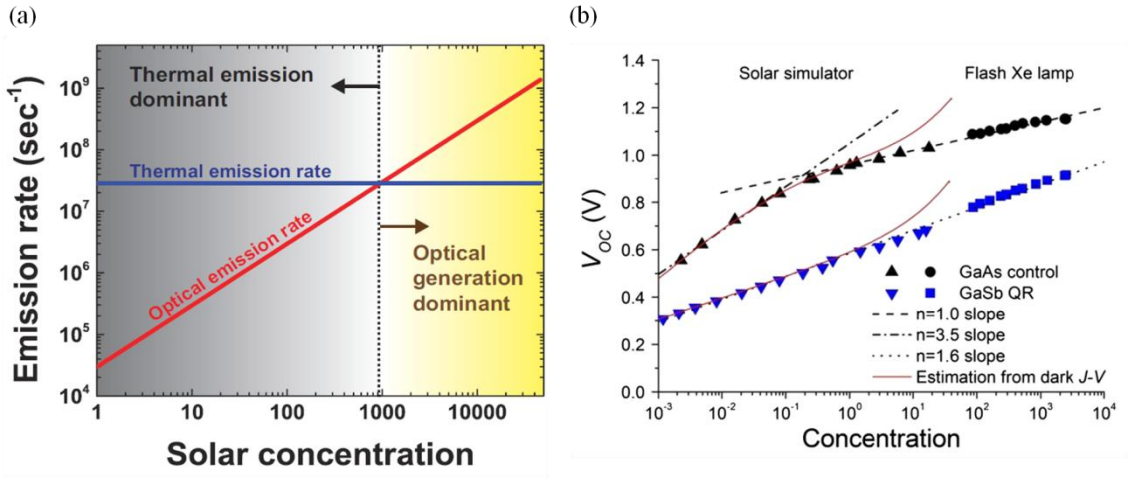

Figure 3.14. (a) Optical (red) and thermal (blue) emission rate for holes confined in GaSb/GaAs QD for different solar concentration. For concentration below 1000 suns hole thermal emission to the VB dominates, and for concentration above this value optical generation dominates [20]. (b) Room temperature open-circuit voltage (*Voc*) vs solar concentration for GaSb/GaAs QRSC (blue) and GaAs reference SC (black). Ideality factors (n) are also shown: 1 (dash - dash), 3.5 (dash - dot) and 1.6 (dot - dot) [95].

Even when thermionic emission degrades cell performance, the hole capture cross-section (σ_h) in this type-II structure is ~$2x10^{-16}$ – 10^{-12} cm^2 [20, 98], which is orders of magnitude lower than the electron capture cross-section (σ_e) in type-I structures ~10^{-10} – $3x10^{-12}$ cm^2 [100, 101, 102]. Thermal emission at 300 K is reduced down to $3x10^7$ s^{-1} which is much lower than in type-I systems ($2.6x10^{12}$ - $3x10^9$ s^{-1} [103]).

Summary

The main achievements in type-II GaSb/GaAs QD/QRSC are:

- Longest carrier lifetime, τ_h = 220 ns, measured in type-II InAs/GaAs/$GaAs_{0.82}Sb_{0.18}$ [79]
- Highest *Jsc* = 27.9 mA/cm^2 with *Voc* = 0.58 V, FF = 0.7, and efficiency = 11.7%; under AM1.5d solar spectrum – achieved by stacking 10 GaSb/GaAs QR layers [21]
- Lower thermal hole capture cross-section, σ_h = 2x10^{-16} cm^2, measured in GaSb/GaAs QDSC [91]
- Partial *Voc* recovery at room temperature, reaching 0.916 V (~20 Acm^{-2}) at 300 K under concentration of 2500 suns in GaSb/GaAs QRSC [95]
- TPPC detected and G_{QE} (EQE_{2ph} / EQE_{1ph}) = 3000 at 9 K under IR illumination, corresponding to EQE (E_L) ~10^{-5} in GaSb/GaAs QDSC [86]

Table 3.2. Comparison between type-I InAs/GaAs QDSC and type-II GaSb/GaAs QD/QRSC, showing short-circuit current (J_{SC}), open-circuit voltage (V_{OC}) at different solar concentrations (conc), and electron/hole thermal capture cross-section (σ_e/σ_h), highlighting the highest values.

	Type-I In(Ga)As/GaAs QDSC	***Type-II GaSb/GaAs QD/QRSC***
J_{SC} (mA/cm^2)	27.7	27.9
V_{OC} (V) under 1 sun	0.99	0.89
V_{OC} (V) under conc	1.506 (20 K, 1x10^3 suns)	0.916 (300 K, 2.5x10^3 suns)
σ_e , σ_h (cm^2)	10^{-12} – 10^{-10}	10^{-16} – 10^{-13} (at 0.8 – 2.6 V)
τ_e , τ_h (ns)	< 100	220

Type-I was the first system to be studied as an IB candidate, focussing especially on material requirements for IB behaviour, including the use of *ultra-high density stacks*. Meanwhile, type-II research has mainly been based around analysing the *potential and limitations* of QD within an IBSC.

In summary, from the above we can remark that the current state-of-the art in QDSC lies far from the theoretical maximum value and also lags behind that of existing multi-

junction cells. However, the type-II QD approach has some significant advantages over type-I QD, due to an increased carrier lifetime and decreased thermal escape, enhancing J_{SC} and TPPC, as shown in table 3.2. But there are also some significant drawbacks, which include in particularly large V_{OC} reduction due to *hole trapping* and high *QD recombination rate*. Also, full V_{OC} recovery under solar concentration has not yet been achieved in this structure.

This thesis is focused on the modification of QR stack(s) to improve *sub-bandgap light absorption* and to reduce *hole-photocurrent loss* (photogenerated holes migrating from base to emitter) and analysing IB behaviour by quantifying *radiative and non-radiative mechanisms* limiting IB performance. More specifically, the following chapters report on a detailed study of:

(i) The effect of increasing *sub-bandgap optical absorption* by increasing the number of GaSb/GaAs QR layers

(ii) The effect of decreasing *hole-photocurrent loss* by reducing the overall thickness of the QR stack placed in the intrinsic region

(iii) *QR hole charging and discharging mechanisms* via measuring TPPC at different temperatures and light intensity, quantifying capture rate, thermionic and photogenerated emission rates

(iv) Radiative and non-radiative decay times via time-resolved photoluminescence measured at low temperature

(v) Partial V_{OC} recovery under high solar concentration measured at room temperature

(vi) Recombination when artificially increasing the bandgap by applying hydrostatic pressure at room temperature

Chapter 4

Experimental techniques

Type-II GaSb/GaAs quantum rings (QR) were grown by Molecular Beam Epitaxy (MBE) (4.1) and the material quality of the samples was studied (4.2 - 4.4). Devices containing GaSb/GaAs QR were fabricated in the cleanroom (4.5), and the electrical properties were measured under different conditions (4.6 – 4.13). MBE growth, material characterization, device fabrication and standard solar cell characterization was done in the Quantum Technology Centre at Lancaster University. The most specific characterization techniques were performed in different laboratories: Advanced Technology Institute (Surrey university, UK), Instituto de Energia Solar (Universidad Politecnica de Madrid, Spain) and Nelson Mandela University (South Africa).

4.1 Molecular Beam Epitaxy

Molecular-beam epitaxy is an ultra-high vacuum technique (UHV) - pressure as low as 10^{-11} Torr - where the molecular beams generated from the thermal Knudsen sources interact on a heated crystalline substrate to produce a single-crystal layer. The UHV ensures a very low impurity background (~10^{15} cm^{-3}), and the slow deposition rate (~ 1μm/hour) of the molecular beams allows high control on layer thickness and composition. The rapid response of the shutters (one for every source), assures abrupt interfaces between layers with different composition or doping. By tuning the growth parameters (substrate temperature, deposition rate, III-V ratio and shutter time) the dimension of the structure (0D, 1D, 2D or 3D) can be controlled, achieving quantum structures with electron and/or hole confinement in the different dimensions. Therefore, MBE is an epitaxial growth technique with the highest achievable purity of the grown films [104].

The samples presented in this thesis were grown at Lancaster University, in a Veeco GENxplor MBE System. Figure 4.1 sketches the configuration of the growth chamber. The substrate is introduced via a load lock and placed in a substrate holder close to the heater and in front of the multiple cells (Si, Sb, Ga, As, Be). During growth, substrate rotation is turned on to obtain a uniform material deposition. A reflection high-energy electron diffraction (RHEED) pattern is obtained using an electron gun and a phosphor screen (see section 4.1.2 of this chapter for more information). When liquid nitrogen flows inside the cryopanelling, impurities inside the chamber condense on the inner wall decreasing further the pressure. Finally, the chamber wall isolates the cryopanelling from the outside atmospheric pressure.

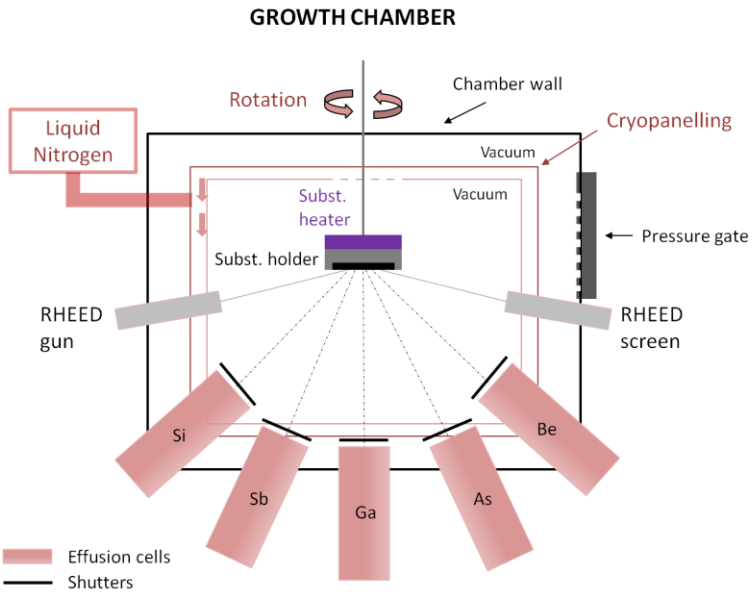

Figure 4.1. Sketch of MBE growth chamber containing two walls: chamber wall; and cryopanelling, with liquid nitrogen flowing through it to reach ultra-low pressure. The substrate is introduced via pressure gate, placed in the substrate holder close to the heater, rotating during growth. The different materials are inside an effusion cell blocked by a shutter, and placed in front of the substrate. A RHEED gun and screen are necessary to monitor growth through RHEED pattern.

4.1.1 Substrate preparation

Substrate preparation is required prior to every growth. The surface needs to be clean atomically for ensuring epitaxy with the molecular beam - atoms of the molecular beam need to interact with atoms on substrate surface. The sample preparation and loading

process are sketched in Figure 4.2. First, the substrate is loaded into the load lock chamber where water is desorbed by using a heater (~ 100 °C), while rotatory and turbomolecular pumps are used to decrease the atmospheric pressure down to ~ 10^{-7} Torr. Then, it is transferred to the Prep-chamber and placed on the heater (~ 300 °C) for hydrocarbon desorption. During desorption the Prep-chamber reaches a pressure of ~ 10^{-6} Torr, the ion pump is used to recover low pressure. Once it reaches ~ 10^{-9} Torr, the substrate is transferred to the Growth chamber, where the substrate temperature is increased up to ~ 20 ºC higher than standard growth temperature for desorbing oxide from the surface (~ 580 ºC for GaAs). At this point the substrate is "atomically" clean and ready for epitaxial growth. To ensure low background impurities during growth, the pressure is decreased down to ~ 10^{-10} Torr by using a cryopump inside the chamber once the crypanelling is cooled down to 70 K using liquid nitrogen.

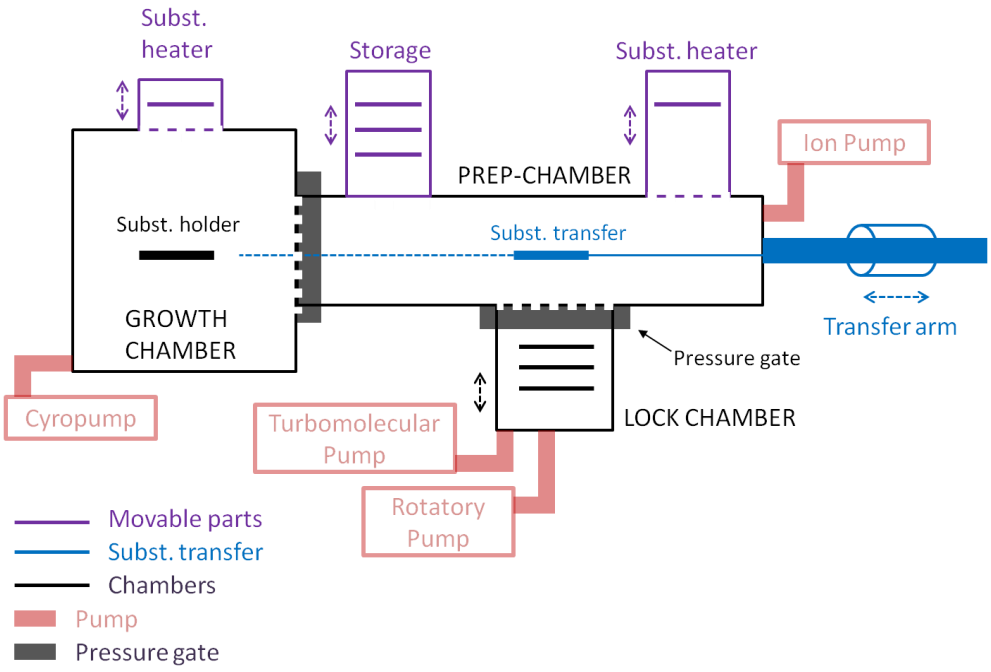

Figure 4.2. Diagram of the Veeco GENxplor MBE System at Lancaster University. Substrate is introduced via a load lock chamber, rotary and turbomolecular pumps decrease pressure down to ~ 10^{-7} Torr. Then, it is transferred to the Prep-chamber, where ion pumps decrease pressure down to ~ 10^{-9} Torr. A Transfer arm is used for moving the substrate from Heater to Storage and Growth chamber. Inside thhe Growth chamber, once the cyropump is cooled down to 10 K, the pressure is decreased down to ~ 10^{-10} Torr. The three chambers are separated via pressure gates.

4.1.2 RHEED

This in-situ technique called reflection high-energy electron diffraction (RHEED) is used for monitoring the growth process and it is essential for calibrating growth rate and identifying surface reconstruction and surface roughness. The technique consists of an electron beam with energy of 14 keV impacting the crystal surface, at a shallow angle (1 - 2º) so that the reflected beam forms a diffraction pattern on the phosphorescent screen. The specular reflection is essential for calibrating the growth rate as the intensity oscillation frequency corresponds to the monolayer (ML) growth rate [105], and the intensity shows the degree of "disorder" or growth stage of the ML itself. This can be explained by using the layer-by-layer growth approach where the adsorbed atoms on the surface start assembling with each other into islands forming one ML at each time. Through this process the surface experiences three extreme situations: (a) smooth surface - before any deposition starts, (b) maximum disorder / isolated islands not fully assembled – half of the ML, (c) "completely" planar after complete island assembly – end of ML formation. These three stages correlate with a full oscillation in the brightness of the specular spot: (a) first maximum, (b) minimum, (c) second maximum; as shown in Figure 4.3.

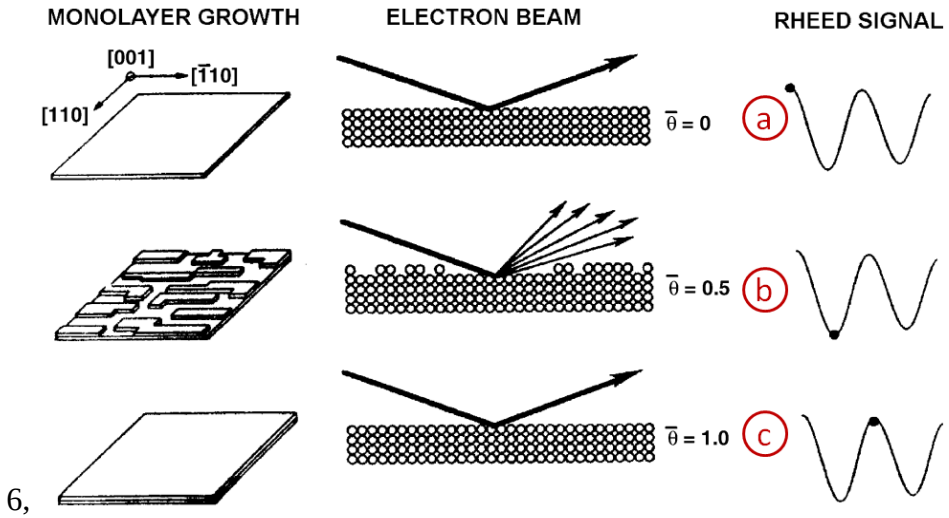

6,

Figure 4.3. Illustration of the mechanism for RHEED specular spot oscillations during layer-by-layer growth of a monolayer: (a) Smooth surface - before any deposition starts, (b) maximum disorder / isolated islands not fully assembled – half of the ML, (c) "completely" planar after complete island assembly – end of ML formation [106, 107].

The diffracted pattern is crucial for determining the surface reconstruction of the atoms that depends on III-V flux ratio. During epitaxial growth, the atoms of the surface are re-arranged to minimise the free energy. In the case of a crystal with periodicity *a*, if during growth the periodicity doubles (*2a*) in one direction and stays the same in the perpendicular one, the surface reconstruction is *2x1*. If instead, it doubles in one direction and it quadruples (*4a*) in the perpendicular one, the reconstruction is *2x4*. For a 2D growth, RHEED pattern consists of parallel lines spaced by *a*. For a surface reconstruction of *2x*, every two bright lines a third one appears separated by ½ from each other. And for reconstruction of *4x*, three lines appear between the two bright ones separated by ¼. In this work, for (001)-GaAs in As rich conditions at the optimum growth temperature (500 – 570 ºC) the surface reconstruction is *2x4*.

4.1.3 Epitaxial growth modes

The growth of an epitaxial layer depends critically on the interaction strength between adatoms and the surface, as growth occurs via the vapour phase. Figure 4.4 shows the three different types in MBE growth: 3D Volmer–Weber (VW) growth (adatom–adatom interactions are stronger than those of the adatom with the surface) [108], 2D Frank–van der Merwe (FM) layer-by-layer growth (adatoms attach preferentially to surface sites resulting in atomically smooth layers) [108, 109] and Stranski–Krastanov (SK) growth (above the critical thickness the 2D layer growth turns to 3D island growth releasing the accumulated strain the structure) [108, 109, 110].

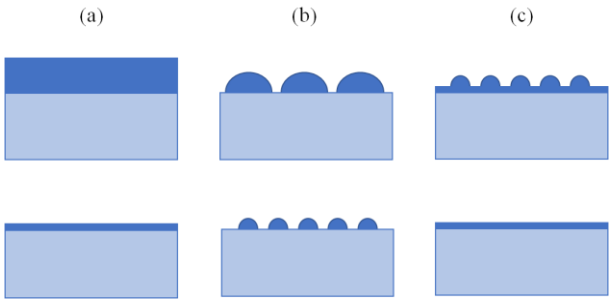

Figure 4.4. Growth modes: (a) 2D Frank–van der Merwe growth, (b) 3D Volmer–Weber growth directly on top of the substrate and (c) 3D Stranski–Krastanov where an initial wetting layer grows prior to 3D nucleation.

4.1.4 Growth of GaSb/GaAs Quantum Ring Stack

Self-organised GaSb quantum dots (QD) can be grown epitaxially on GaAs, due to the large lattice mismatch of ~8% between the materials. GaSb QD are grown by Stranski-Krastanov method after depositing a thin GaSb wetting layer (WL) of ~2 nm. The shape of the islands can be controlled obtaining quantum rings (QR), QD or clusters. Figure 4.5 shows the two different approaches to grow type-II GaSb/GaAs quantum rings (QR). At Lancaster University, the GaSb QDs are capped by two different GaAs layers to achieve predominantly QR shape. By modifying the thickness of the first cap layer and the temperature of the second cap layer, the relative amount of QD, QR and clusters can be controlled, as shown in Figure 3.14(a) and (b). GaSb ring formation is favoured by the use of a thin first cap layer (≤ 8nm) and a high growth temperature for the second cap layer (580 °C) [111]. Taiwan University has recently developed another approach, based on As soaking (30 sec) after GaSb QD formation [96].

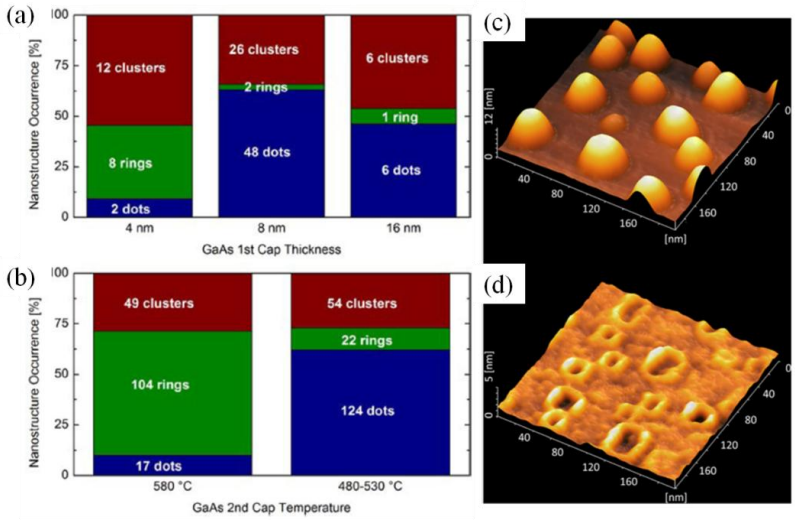

Figure 4.5. (a) and (b) represent the percentage of clusters (red), rings (green) and dots (blue) for different growth conditions [111]. (a) Varying thickness of first cap layer, where first and second cap temperature were 430 and 530 °C. (b) Varying temperature of second cap layer, where thickness of first cap layer was kept ≥ 8 nm. (c) and (d) show AFM images of an uncapped layer of QD and QR, respectively [96]. After GaSb QD formation via SK method, As soaking turns the initial QD toward QR shape.

The growth recipe used in this thesis for growing GaSb/GaAs QR stacks is adapted from E. P. Smakman et. al. [111]. Growth rate and GaAs substrate temperature needs to

be calibrated in the Veeco GENxplor MBE system prior growth. Figure 4.6 shows the different layers of a QR stack sample showing substrate temperature for each layer, a GaSb/GaAs QR layer contains a thin WL and self-assembled QR nanostructures.

The GaSb/GaAs QR samples are always grown on n-type GaAs substrates with a doping density of $1x10^{18}$ cm^{-3}. The recipe for a GaSb/GaAs QR stack consists on a thick 300 nm un-doped GaAs buffer layer at 560°C grown at 1 µm/h, then the temperature of the substrate is lowered to 480°C under As flux prior GaSb QR growth, after Sb flux is irradiated for 30 s to exploit As-Sb exchange reaction, followed by the growth of nominally 2.1 ML GaSb QR with 0.3 ML/s growth rate. For obtaining QR shape the GaSb self-assembled nanostructures are capped by a 5 nm GaAs cold cap layer grown at 430°C, and for preserving good crystal quality a GaAs layer is grown between consecutives QR layers at 560°C. Once the QR stack is grown a final cap of GaAs is grown on top of 100 nm. The thickness of cold cap and GaAs layers changes for each sample, tables 4.1 to 4.4 summarise the growth parameters of each sample.

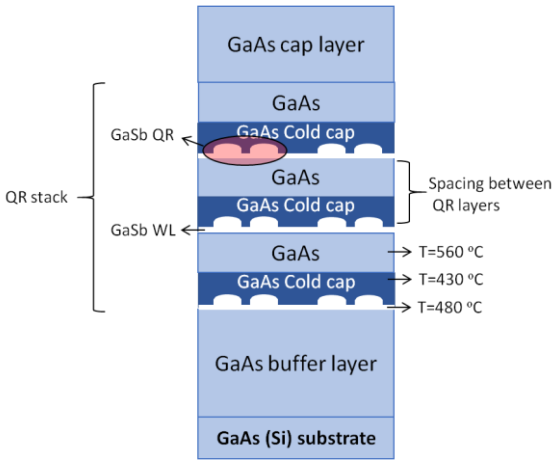

Figure 4.6. GaSb/GaAs quantum ring (QR) stack sample. Each QR layer contains a thin wetting layer (WL) and QRs (red shaded area) in white. QR layers are capped by a thin GaAs Cold cap layer (dark blue) followed by a GaAs layer (light blue). Substrate's temperature is also shown.

Section 4.2 shows transmission electron microscopy for the QR sample PJC645 with 10 QR layers spaced by 40 nm, showing evidence of quantum ring formation. The sample's growth parameters are shown in table 4.1 at the end of this chapter.

4.1.5 Doping calibrations and Solar Cell structure

Controlling doping is crucial for achieving high performance devices. For doping calibration, doped samples with a thickness ≥1μm are grown on semi-insulating substrate. For each dopant, a set of doped samples are grown for different temperature of the effusion cell of the dopant material (T) as doping concentration scales linearly with $1000/T$. Doping can be measured by techniques like SIMS, however it may differ from the activated doping. By using the Hall effect, the electrically activated doping can be measured directly and it can be checked by Capacitance - Voltage measurements on a diode device. Figure 4.7 shows the grown GaAs reference solar cell, following standard values for doping and layer thickness for a high efficiency GaAs SC [112]. The high energy photons are absorbed strongly close to the surface in GaAs (~0.4 -0.65 μm), where the top layer of the solar cell is a thin emitter (0.5 μm) so photo-generated electrons can diffuse to the p-n junction before recombining with photo-generated holes. Emitter is heavier doped than base with p-doped of 10^{18} cm^{-3}, for producing a strong electric field across the depletion region to separate the carriers. The bottom of the solar cell is a thick base of 3 μm where the low energy photons are absorbed (~0.65 – 0.85 μm). The base has low n-doping of 10^{17} cm^{-3}, for avoiding high recombination before photo-generated electrons reach the n- contact and photo-generated hole the p-n junction. The intrinsic regions are typically between 0.1 and 0.5 μm thick, in our case because we place the QR stack in the i-region, the region was kept the thickest possible without degrading the solar cell performance. A window layer is grown on top of the emitter for avoiding surface recombination, reflecting the minority carriers to the p-n junction. The contact layer reduces the contact resistance due to high doping levels (in our cells we wanted to achieve [p] ~10^{19} cm^{-3} doping concentrations, but the maximum doping achieved was 10^{18} cm^{-3}). In this work, the dopants used in GaAs are Si and Be for n and p-doping, respectively.

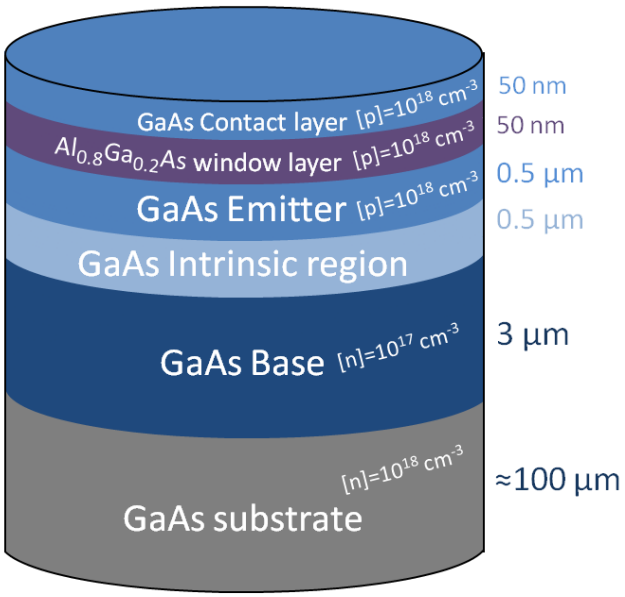

Figure 4.7. GaAs reference solar cell with a thick n-doped Base (3 µm), an undoped intrinsic region (0.5 µm), a p-doped Emitter (0.5 µm), a thin p-doped window layer (50 nm), and a thin p-doped contact layer (50 nm), grown on top of a n-doped GaAs substrate (≈ 100 µm).

4.2 Transmission Electron Microscopy (TEM)

Transmission electron microscopy (TEM) is a powerful technique used for nanocharacterization. A high energy electron beam impacts the sample, obtaining information of the surface from the diffracted electrons. The atomic resolution allows measuring QD height as thin as 1-2 nm. Dark field configuration is more sensitive to composition and bright field to strain. Figure 4.8 shows a cross-sectional TEM picture of the PJC645 with 10 layer GaSb/GaAs quantum ring stack with a 40 nm spacing (table 4.1), exhibiting pristine interfaces without dislocations or defects [21]. The coherently GaSb rings present an average distance between the two lobes of the QR of ~22.2 nm for outer diameter and 3-4 nm for QR height, with a surface density of 10^{10} cm^{-2}. The GaSb WL has around ~1.1 nm thickness.

TEM samples are prepared prior to characterization using standard grinding, polishing and Ar+ ion-milling to electron transparency. The TEM measurements were performed by Richard Beanland in Warwick University, using a JEOL2100 LaB6 TEM operating at 200 kV.

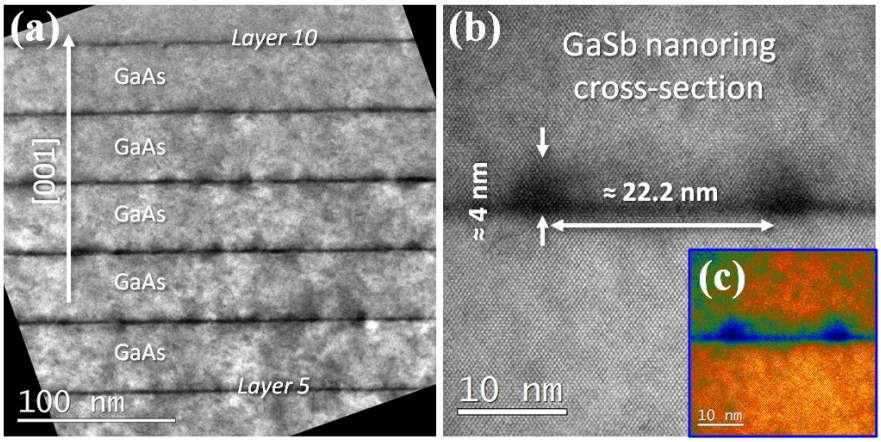

Figure 4.8. Cross-sectional TEM pictures of 10 layer GaSb/GaAs quantum ring stack. (a) From layer 5 to 10 showing the alternate GaSb and GaAs layers. (b) Magnification showing the two lobes of a single GaSb QR. (c) Same as (b) using brighter colors for helping the eye to see the contrast in lattice parameters between GaSb and GaAs.

4.3 High Resolution X-ray Diffraction (HRXRD)

High resolution x-ray diffraction (HRXRD) is a material characterization technique used for measuring the lattice constant of materials, giving information about the composition and thickness of the layers as well as the strain between them. The HRXRD is the result of the interference between the diffracted x-rays striking the atomic planes, as shown in Figure 4.9 (d is the distance between atomic planes). The condition for constructive interference is given by Bragg's law,

$$n\lambda = 2d\sin(\theta) \tag{4.1}$$

where n is an integer, λ the wavelength of the incident x-ray, and θ is the angle between the atomic planes and the x-rays.

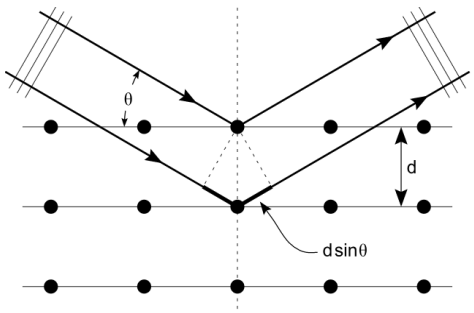

Figure 4.9. X-ray diffraction. The incident x-ray reaches the sample with an angle θ, the light is diffracted by the plane of atoms spaced a distance d between them. The reflected light is the result of the constructive interference between the diffracted beams.

In Lancaster University a BEDE QC200 double crystal rocking machine was used to perform the HRXRD spectra. The electrons generated from the filament lamp are accelerated by a high voltage to a copper target creating the X-ray that is collimated ensuring a monochromatic beam with a wavelength of 1.54 Å. The sample is placed onto a movable table which can be rotated through an angle ω and the beam intensity is recorded by a detector which moves through an arc at an angle 2θ measured relative to the path of the X-ray beam. BEDE software is used to monitor the intensity and obtained the X-ray spectra. By comparing simulations performed with RADS Mercury with experimental data, lattice mismatch, thickness and composition of layers can be obtained.

4.4 Photoluminescence (PL)

Photoluminescence (PL) measurements were performed in the Magneto-Optics lab at Lancaster University. PL set up is sketched in Figure 4.10. The samples are excited by a frequency-doubled, diode-pumped, neodymium yttrium aluminium garnet (Nd:YAG) solid state laser emitting at 532 nm. Figure 4.10(a) shows the laser light going firstly through the laser line filter of 532 nm to reduce the FWHM of the laser emission. Then, the laser beam is attenuated by neutral optical filters reducing the laser power. For measuring the laser power a beam splitter is placed in the light path and a power meter is used. The transmitted light from the beam splitter is focused by an objective lens inside the 200 μm silica core multimode optical fibre (Thorlabs BFL22-200) mounted on an adjustable stage. Figure 4.10(b) shows the laser light travelling through the optical fibre focused on the sample placed at the bottom of the stick. The sample is mounted using electrodag on a copper holder and screwed on the bottom of the stick. For low temperature measurements, the stick is introduced inside the He dewar. A Cernox temperature sensor is placed inside the stick close to the sample, the measurements are

taken once the temperature reader reaches 4 K. The collected light travels through the silica core multimode optical fibre connected to the spectrometer with a diameter of 550 μm (Thorlabs BFL22-550), as shown in Figure 4.10(c). The PL spectrum is obtained using an InGaAs detector and an Acton SpectraPro-2300i spectrometer using the grating with 150 l/mm given a spectrum width of 550 nm. The reflection of the laser is blocked by a long pass filter at the spectrometer's entry slit. The InGaAs array detector (An Andor Technology Peltier-cooled 512 pixel) cooled at to -60 °C operates from 800 to 1700 nm, with a resolution of 1 nm. Measurements at 4 K were performed at full power, 350 mW/cm^2. And for power dependence measurements, laser power was decreased 6 orders of magnitude, by adjusting the current supplied to the laser and adding neutral density filters.

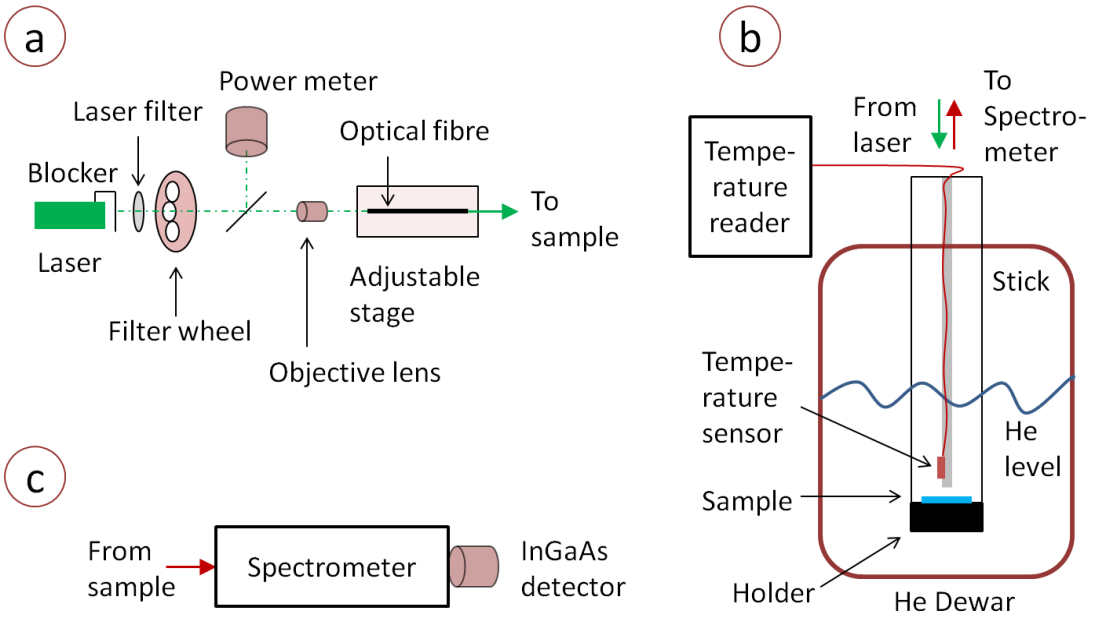

Figure 4.10. Photoluminescence set up. (a) Laser light is filtered (laser filter) to reduce FWHM, then goes through optical density filters (filter wheel) to control laser power. The laser beam is split (beam splitter), the reflected light reaches a power meter to read the laser power, and the transmitted light is focused by a objective lens inside the optical fibre (placed on an adjustable stage). The laser light travels through the optical fibre to the sample. (b) The optical fibre goes inside the stick, where the sample is placed at the bottom. A second optical fibre collects the emitted light. For 4 K measurements, the stick is placed inside the He dewar. The temperature sensor at the bottom of the stick is close to the sample. (c) The second fibre is connected to the spectrometer and the InGaAs detector.

4.5 Device fabrication

Device fabrication was done at the Quantum Technology Centre in a class 1000 / 100 class clean room in Lancaster University. Solar cells were fabricated into a Spider Web Mask with ~ 1 mm^2 area as shown in Figure 4.11, with a metal coverage of 38 % corresponding to an optical fill factor of 62 %. This mask is optimized for reducing series resistance and for increasing current collection under concentrated light, thanks to the multiple fingers with size of ~ 10 µm.

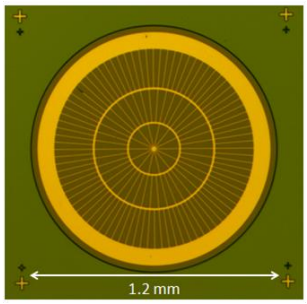

Figure 4.11. Spider Web Mask, with a diameter of 1.2 mm, and multiple fingers ~ 10 µm thick connecting the centre of the mask with the three concentric circles.

Top-bottom configuration has been used as the GaAs based structure is grown on lattice matched GaAs substrate. There are 7 steps involved in the fabrication process: Cleaning (4.5.1), UV photolithography (4.5.2), Top contacts deposition (4.5.3), Lift off (4.5.4), Wet etching (4.5.5), Back contact deposition (4.5.6), and Cleaving and mounting (4.5.7). Figure 4.12 summarises from section 4.5.2 to 4.5.6.

4.5.1 Cleaning

The two-step cleaning process consists of dipping the sample in acetone for 5 minutes, followed by another 5 minutes in isopropanol (IPA). The sample is constantly being moved inside the beaker, finally it is dried by using dry nitrogen.

4.5.2 UV photolithography

The next step is the top contact deposition. Firstly, the pattern needs to be “imprinted” by using resist coating and Ultraviolet (UV) lithography. Two photoresists are deposited on top of the sample by using the Spinner Labspin 6 Suss Microtech.

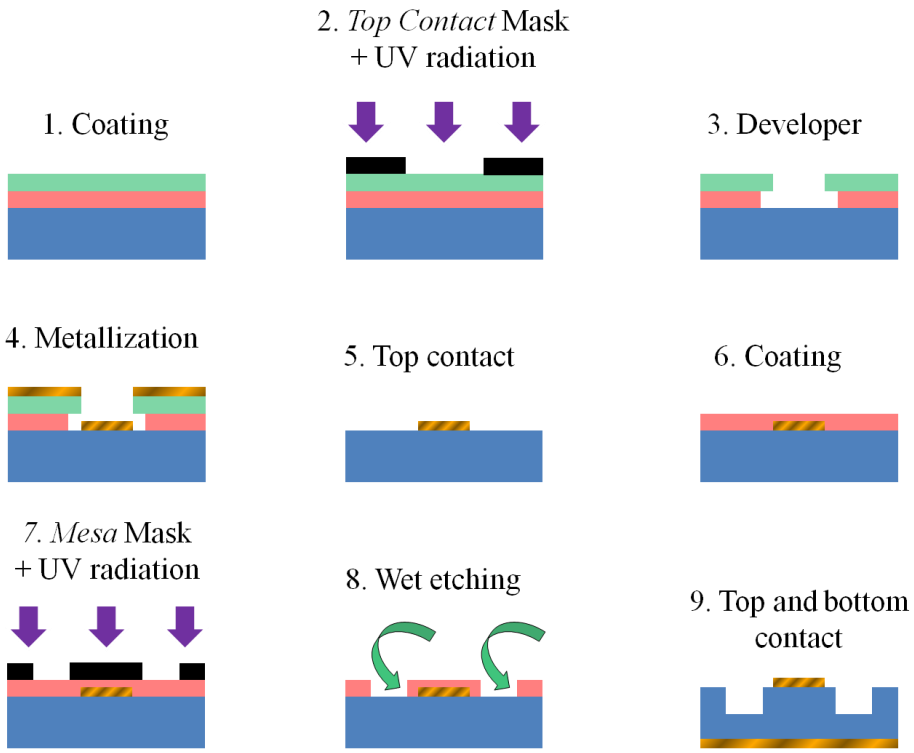

Figure 4.12. 1 to 9 summarise the different steps involved in *Top contact* deposition and Wet etching. After cleaning, the sample is placed in the spinner and two different photoresists are deposited on top (1). Then, UV photolithography is applied using a *Top contact* mask (2), by using developer the impressed pattern is revealed (3). Metals are evaporated on top of the sample (4), and after lift off the desired top metallic contact pattern is on the sample's surface (5). Prior to wet etching, another layer of photoresist is deposited (6) followed by UV photolithography using a *Mesa* mask. Once the top metal contacts are covered by resist and the rest of the surface is exposed, the sample is immersed in the etching solution (8). After another step of lift off the photoresist is removed. The back contacts are evaporated on the bottom of the device, obtaining the final device (9). Colour description: blue-sample, green and red-photoresist, black-mask, purple-UV radiation, orange stripe-metal contacts, and green arrows-chemicals. The "Developer" removes the un-covered photoresist during UV radiation and in "Lift off" all the leftover photoresist is removed.

Firstly, LOR 3A is spun at 3000 rpm during 30 s to produce a homogenous film with a thickness of ~ 1300 nm followed by softbake at 180 ºC for 5 min. A second layer of photoresist is deposited on top of the first one, the S1813 is spun at 6000 rpm for 30 seconds (thickness ~ 1300 nm) and baked at 115 ºC for 2 min. The softbake process is necessary for reducing the solvent content in the layer, improving adherence to substrate, avoiding mask contamination, and preventing the dissolution of the resist layer in multiple coating and bubbling during subsequent thermal processes [113]. After deposition and baking of the two photoresist layers the sample is covered partly to "imprint" the desired *Top Contact* pattern shown in Figure 4.13(a) and is exposed to UV

light for 2.5 s using the Mask Aligner (JBX-5500series). The sample is dipped into developer MF-CD26 for 80 s followed by few seconds in DI water and finally dried using dry N_2. After using the developer an "undercut" is obtained due to a quicker dissolution rate of LOR3A compared with S1813, helping to improve the lift off. *Coating*, *Top contact mask +UV radiation* and *Developer* processes are summarised in Figure 4.12 from step 1 to 3.

4.5.3 Top Contact evaporation

The next step is the Top Contact evaporation, a T60 thermal source Minilab thermal evaporator was used. To obtain good ohmic contacts the work function of the deposited metals must be close to the electron affinity of the p and n-doped GaAs region. For p-doping the contacts used are Au (10 nm)/ Zn (10 nm)/ Au (200 nm), the work function for Au is 5.1-5.5 eV and for Zn is 3.6-4.9 eV, and the electron affinity of undoped GaAs is 4.1 eV [114]. The initial gold layer is deposited for improving the adhesion of Zn to the GaAs surface, rapid thermal annealing (RTA) is necessary to allow Zn atoms to diffuse to the surface (through the thin layer of Au deposited) making an Ohmic contact with the p-doped GaAs layer. *Metallization* process is summarised in Figure 4.12 in step 4.

4.5.4 Lift off

Finally, in the lift off process the gold is removed revealing the "imprinted" pattern. The sample is immersed in Remover 1165 heated at 60 ^{0}C for 15 min. Due to the spider web mask pattern, the lift off process needs to be checked under an optical microscope with the sample inside a flat beaker with acetone, if some gold is still adhered to the sample it is gently wiped with a cotton bud. Finally, the sample is cleaned using the two-step cleaning process obtaining the top contact desired pattern on the surface of the device as shown in step 5 in Figure 4.12.

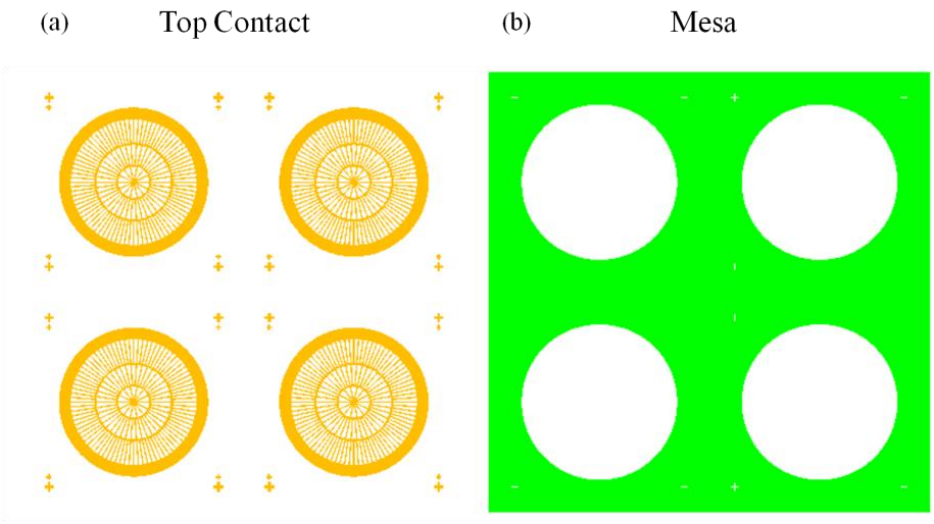

Figure 4.13. The Spider Web Mask pattern obtained from DraftSight software. (a) Top Contact mask used to define the pattern prior Top contact deposition, corresponding to step 2 in Figure 4.12. (b) Mesa mask used to define the pattern prior to etching, corresponding to step 7 in Figure 4.12.

4.5.5 Wet etching

Etching is applied for isolating the multiple cells in the device from each other. Wet etching is used for isotropic etching with smooth edges, while avoiding contaminants on the lateral surface. Prior to etching the pattern *Mesa* mask shown in Figure 4.13(b) is used to cover the top contact metallization protecting it. The same procedure as in *Top Contact* is applied for imprinting the pattern, this time just S1813 will be used as undercut is not necessary in this step (there is no lift off process). The bottom of the sample needs cleaning prior to photoresist baking, to avoid photoresist contamination on the bottom of the device. *Coating* and *Mesa mask +UV radiation* processes are summarised in Figure 4.12 in steps 6 and 7.

After patterning the sample the thickness of the resist is checked with the Alpha Step Surface Profiler (10 nm resolution). The wet etching dissolution for GaAs consists of orthophosphoric acid mixed with hydrogen peroxide and deionized water, H_3PO_4:H_2O_2:H_2O, with 1:1:10 ratio [115] [116]. The standard rate for this etching mixture is calibrated after the first minute, as ~ 0.4 μm/min. Typical etched thickness in GaAs based devices is ~ 2 μm, penetrating ~ 1 μm inside the n-region, ensuring that the

intrinsic region is completely etched. After the process, the side walls of the p-i-n junction are smooth and isolated from the other devices, as shown in Figure 4.14. *Wet etching* process is summarised in Figure 4.12 in step 8.

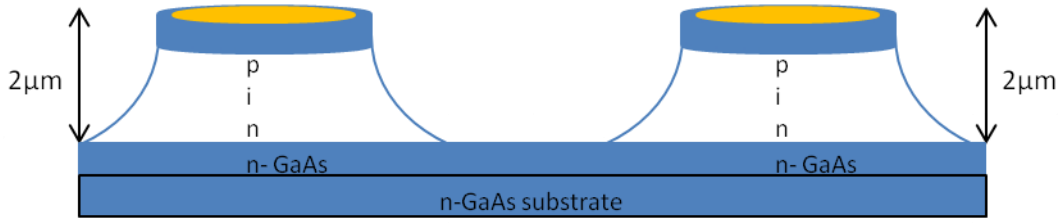

Figure 4.14. Diagram of the device cross-section after etching. 2 µm have been etched inside the p-i-n structure defining its sidewall smoothly, and isolating each device.

4.5.6 Bottom Contact deposition

GaAs is a wide bandgap material (E_G ~ 1.5 eV) and different metallic contacts are required for p and n-region contacts. For the back contact, a layer of 20 nm of InGe followed by a 150 nm of Au are evaporated in the thermal evaporator. The metals are deposited directly on the back surface of the device, without defining any pattern with the photoresist as previously shown for Top Contact deposition (subsection 4.5.3). The final device with top and bottom contacts is shown in step 9 in Figure 4.12. The structure of a finished processed GaAs solar cell device using the spider mask is shown in Figure 4.15.

4.5.7 Cleaving and mounting

Once both contacts, top and bottom, are deposited and the single cells are isolated the device is ready to characterize via probe station. However, some of the characterization techniques require the device to be mounted on a header. The last step consists of: scribing the processed wafer into individual devices (SUSS RA 120M); mounting the device on the metallic header using silver epoxy and baking for 60 min at the curing temperature of 150ºC; and finally, wire bonding using Au wire.

Extra steps could be further studied like passivation layers for decreasing and removing defects in sidewall – it was not necessary for the GaAs reference cell but it might be

interesting to study the effect on the QR solar cells. Anti-reflection coating was not studied, the effect on GaAs solar cells is already well known, and the focus of this thesis is the analysis of physics of the GaSb/GaAs QRSC working as an IBSC. RTA (Rapid Thermal Annealing) was optimized for a different mask with larger contact area and series resistance was reduced by an order of magnitude, however it had little effect on contacts made with the *Spider Web Mask*, meaning that Zn diffuses through the thin Au layer during the evaporation step. Oxygen plasma cleaning was used prior to evaporation for removing any developer residue, however it was also found not necessary.

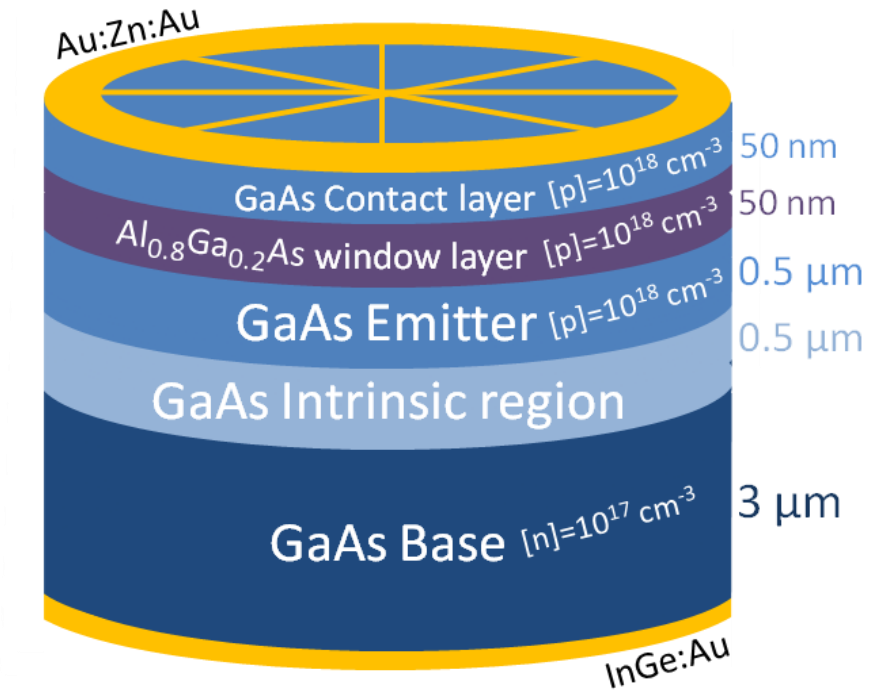

Figure 4.15. Device structure of the reference GaAs solar cell fabricated into a device using top-bottom contacts with *Spider Web mask*. The structure consists of a p-i-n diode (emitter, intrinsic region and base) with a contact and window layer on top.

4.6 Current – Voltage (I-V) characteristics

For measuring the I-V characteristics of un-mounted devices a probe station is used, it integrates an optical microscope and two metallic probes for electrical contact. The headers of the mounted devices have two metallic legs for positive and negative

contacts. Both, the probes and the holder are connected to a Keithley 2400 Source Meter Unit that is remotely controlled via the Labview program installed in the computer. In the program the starting and final voltage are set typically to - 0.5 to 2 V, with steps of 0.1 V, with a current limit of 0.2 A for avoiding damage to the device.

4.7 Capacitance – Voltage (C-V) characteristics

C-V measurements were taken using the probe station for making electrical contact with the device. The capacitance was measured using a Agilent E4980A Precision LCR meter. This measures the capacitance at an applied DC bias by a superimposed AC voltage of amplitude 25 mV and frequency 1 MHz. A parallel equivalent circuit mode was used as the parallel shunt resistance is larger than the parasitic series resistance. A maximum of 15 V reverse bias was applied during the measurements to fully deplete the base.

4.8 1 Sun I-V characteristics

For measuring the conversion efficiency of the solar cells, an illumination of 1 Sun with the AM 1.5G spectra was simulated with an LOT ORIEL LS0106 solar simulator, as shown in Figure 4.16. The devices are placed 10 cm from the light source to ensure homogeneity in an area of ~ 5 cm^2. The incident power is measured with a power meter of 1 cm^2 area. The current source of the solar simulator is slowly increased up to 6.5 mA to obtain a power of 100 mW. To measure the I-V curve, the solar simulator is placed above the probe station or the connected header as described in the previous section 4.6.

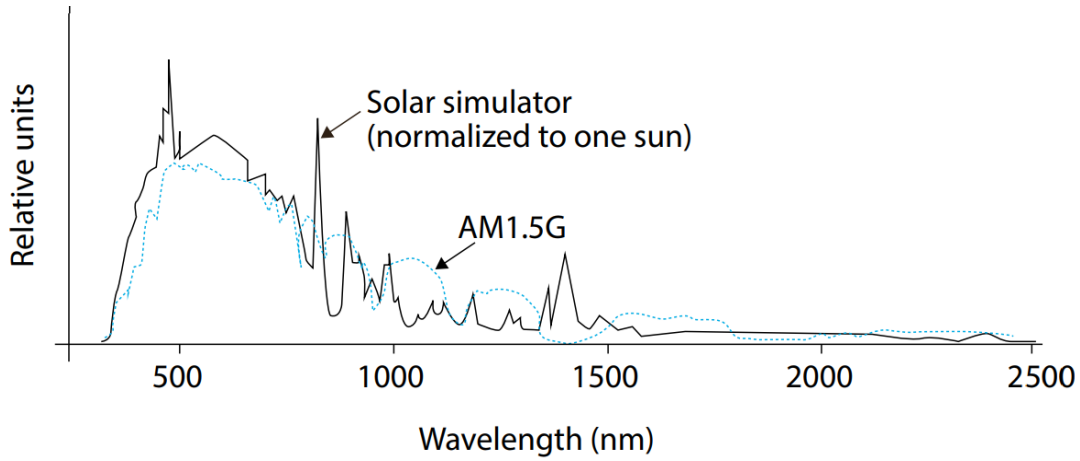

Figure 4.16. Solar simulator spectrum (Xe arc lamp 150 W) normalized to one sun (solid black line) and AM1.5G spectrum (dotty blue line) from 400 to 2500 nm.

4.9 External Quantum Efficiency (EQE)

The external quantum efficiency of the solar cell is the ratio between extracted electrons (current) and incident photons (illumination) on the device. The PVE300 photovoltaic Bentham system was used for the EQE measurements. Figure 4.17 shows the set up, consisting of a 100 W Quartz Halogen (QH) lamp operating at 8.5 A and 12 V provided by a 610 constant current supply. The QH lamp has a black-body spectrum similar to Sun´s emission, with a maximum power density of 1.6 mW/cm^2 for 800 nm, producing spectrum of light over the range 250 - 2500 nm. The TMc300 monochromator has two gratings with a wavelength resolution below 1 nm, one for the range 0.3 - 1.1 μm (1200 lines/mm) and another one for 1.1 – 2.5 μm (600 lines/mm). The chopped light is focused on an area of 0.25 mm^2 over the moveable stage with a stepper motor. The current is measured by a 496 DSP lock-in amplifier and 218 Optical chopper controller The incident radiation is calibrated with two reference detectors: Si for the range 0.3 – 1.1 μm and Ge for 0.8 -1.8 μm. The temperature is set to 25 ºC with a Peltier plate. GaAs reference solar cells were measured from 0.4 to 1 μm and QR SCs from 0.4 to 1.5 μm.

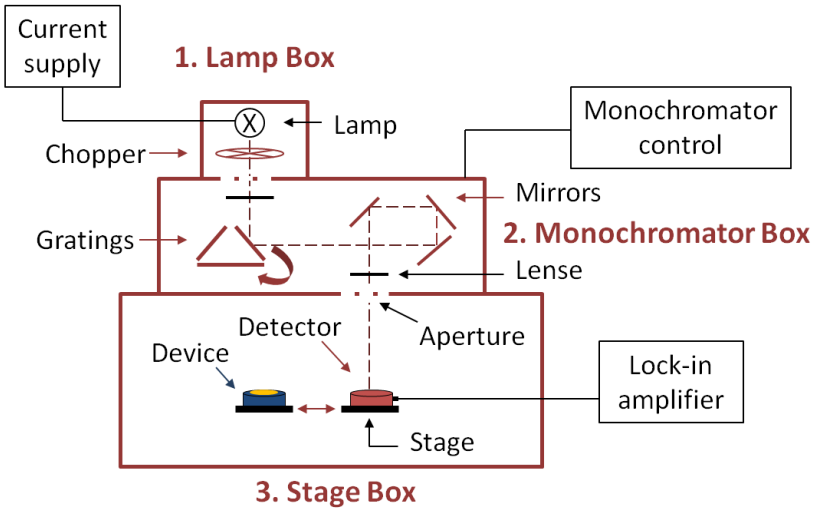

Figure 4.17. PVE300 photovoltaic Bentham system, experimental set up for External Quantum Efficiency measurements [117]. The chopped lamp light (1. Lamp box) goes inside the monochromator, with three gratings and a set of optical lenses and mirrors (2. Monochromator box). The light beam is focused on the stage, where firstly is placed the detector for calibrating the incident flux density and secondly the device for measuring the EQE spectra (3. Stage box).

4.10 High Light Concentration

High light concentration measurements were performed at Instituto de Energia Solar in Universidad Politecnica de Madrid (Spain), with the supervision of Dr. Pablo. G. Linares. Figure 4.18 shows the high light concentration set up used. A photography flash camera (Xenon discharge lamp) is used to generate the pulsed light beam, that is concentrated on the device by using a concentration lens. The solar cell device is simplified in Figure 4.18 as a current and a voltage source. Short-circuit current (J_{SC}), open-circuit voltage (V_{OC}) and *J-V* curve are measured using a shunt resistance and a 4-quadrant source-meter. The electrical measurements measure the response to the flash light, where the intensity decreases exponentially with time. For collecting the fast electrical signal a DAQ interface is used together with a specific data acquisition system (PCI card) in the PC. An external photodiode is always placed close to the device, recording illumination intensity vs time, just for comparing and synchronizing the intensity obtained. For each flash shot- J_{SC} and V_{OC} are measured in consecutive flash shots and the PC monitors J_{SC}-V_{OC} pairs for each concentration factor. [Obtained from *IEEE J. PV 3 (2013)* [78]] A measurement takes place as follows: the flashlamp is

charged, from the software we start the measurement and the camera flashes twice consecutively, in the first flash the circuit must be in short-circuit configuration to measure J_{SC}, and before the second shot flashes the circuit must be changed to open-circuit configuration for measuring V_{OC}. Then, using the intensity recorded by the photodiode in each shot, J_{SC} is matched with the corresponding V_{OC} measured under the same illumination intensity, hence obtaining J_{SC} - V_{OC} pairs for each concentration. For different concentration factors, the distance between flash camera and concentrating lens is modified; the lens is focused for each set of measurements on the device. The concentration factor (x) is defined as the ratio between J_{SC} *(x suns)* and J_{SC} *(1 sun)*. Due to high series resistance in the devices, J_L is measured instead of J_{SC} by biasing the device between - 0.25 and – 1 V (where I-V curve is flat).

The measurements were performed at room temperature for three concentration ranges: 0.01 – 10 suns, 1 – 1000 suns, and 10 – 4000 suns. For each range the electrical characterization was obtained recording J_L-V_{OC} pairs. To improve the accuracy of the results, the measurements are taken 3 times (from each flash we obtain a J_L-V_{OC} curve) and the final data is the average of the 3 scans.

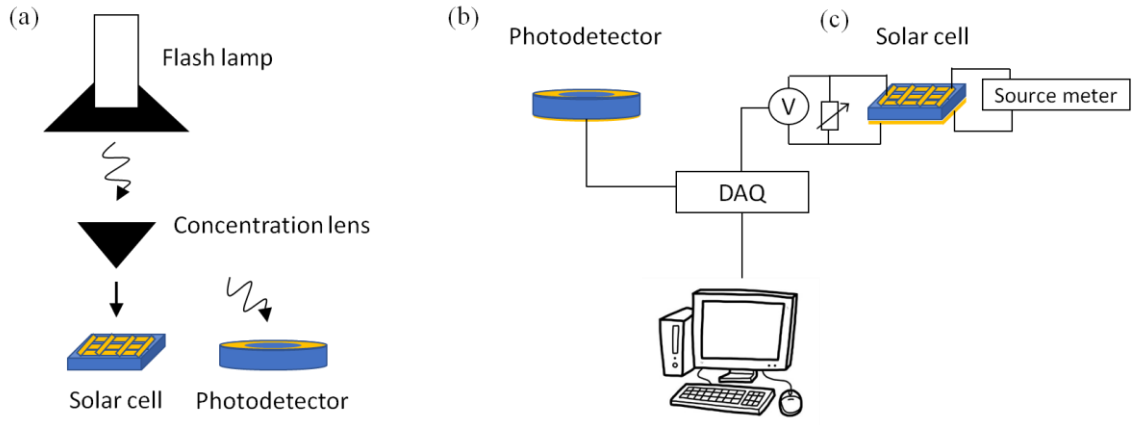

Figure 4.18. High light concentration system. (a) A flash camera is concentrated on the solar cell by using a concentration lens. The photodetector is placed close to the solar cell for reference. (b) For each flash the voltage generated in photodetector and solar cell is collected by a DAQ interface connected to the PC. (c) The source meter is connected to solar cell to force short-circuit and open-circuit conditions, measuring voltage and current with a voltmeter and a shunt resistor.

4.11 Hydrostatic Pressure

Hydrostatic pressure measurements were performed at the Advanced Technology Institute in Surrey University (UK), with the supervision of Dr. Igor. P. Marko. Figure 4.19 sketches the hydrostatic pressure setup. A unipress He-gas compressor is used to increase the pressure from 0 to 8 kbar. The compressed He gas builds up the pressure hydrostatically in the chamber, where the device is placed. Two different chambers were used in the experiment, one for performing dark characterization and another one with a sapphire window for measuring under illumination conditions. Both chambers have electrical connection for measuring current and voltage. [118]

Hydrostatic pressure measurements were carried out at room temperature, measuring the spectral response and I-V characteristics. The spectral response is measured from 400 to 1300 nm by using a Bentham quartz-halogen (QH) lamp connected to a Bentham TMc300 grating monochromator. A Ge reference detector was used to obtain the spectral flux dependence of the source. In section 4.9 the EQE setup is described, including more details of spectral response measurements. I-V characteristics are measured using a Keithley 2635 source-measure unit controlled by a Labview program in the computer. QH lamp is used to simulate solar illumination.

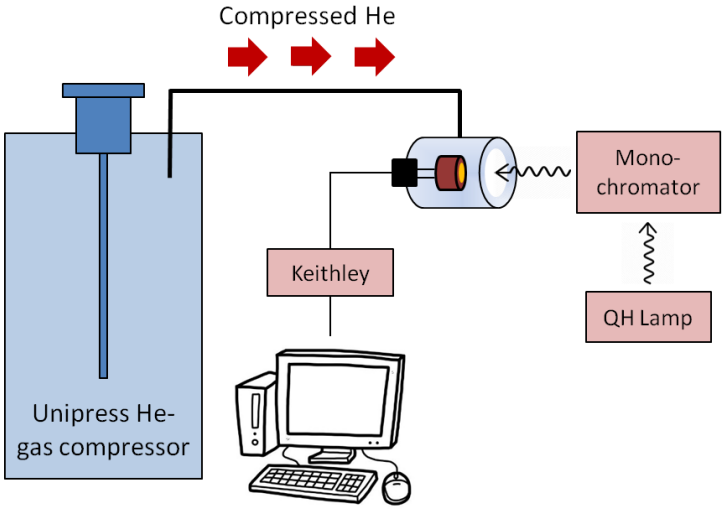

Figure 4.19. Hydrostatic pressure is generated using a Unipress He-gas compressor. QH lamp light goes through monochromator to the device by a sapphire window. Electrical measurements are taken using a source-measure unit controlled by a Labview program in the PC.

4.12 Two-Photon Photocurrent (TPPC)

Two-photon photocurrent measurements were performed at Nelson Mandela University (South Africa) by Prof. Magnus C. Wagener. In the two-colour spectroscopy setup two light sources are used: a mid-infrared Bentham TMC300 spectrometer and quartz-halogen lamp (primary source), and a 975 nm 5 mW laser diode (secondary excitation source). The primary source was focused on the top of the solar cell mesa using gold mirrors and a CaF lens. The devices were oriented at normal incidence to the excitation sources inside a closed-cycle helium cryostat with a ZnSe window. For photocurrent measurements the solar cells are bias under 1 V reverse bias using a picoammeter and phase-sensitive lock-in amplifier, with the optical chopper placed in-front of the entrance slit of the spectrometer (primary source). The laser diode (secondary source) was used as a continuous, unmodulated photo-filling source, with the intensity varied by means of neutral density filters. The spectral flux dependences of the excitation sources were determined directly using calibrated photodiodes. In the case of time-dependent two-colour measurements, the phase-modulated photocurrent signal was monitored using a digital oscilloscope. [119]

4.13 Electroluminescence (EL) spectroscopy

Electroluminescence measurements were performed at Nelson Mandela University (South Africa) by Prof. Magnus C. Wagener. EL is the radiative recombination between carriers injected in the device, the inverse process of EQE measurements. In this case, the device is biased with current flowing through it and the emitted light is collected. EL is the standard technique for characterizing an LED and EQE for a solar cell.

A Keithley 6221 pulsed generator is used to produce the square electrical current pulses between 0.2 to 100 mA in amplitude. The typical pulse frequency of 70 Hz and duty cycle of 4% was used. A set of lenses focused the emitted light into a Cornerstone 260

0.25 m grating monochromator equipped with room temperature InGaAs detector for detecting the EL intensity for each wavelength. The photocurrent was measured using a Keithley 6487 picoammeter and lock-in amplifier synchronised to the pulse generator. The EL spectrum is measured from 0.7 to 1.6 eV at 18 K, using a closed cycle helium cryostat.

4.14 Type-II GaSb/GaAs Quantum Ring Photoluminescence samples and Solar Cell devices

In this thesis different samples and devices were grown to study sub-bandgap absorption enhancement, hole transport through the device and carrier dynamics in QR. Tables 4.1 and 4.2 summarise the different photoluminescence samples grown and studied in this thesis and tables 4.3 and 4.4 the two sets of quantum ring solar cell (QRSC) devices grown, processed and characterized in this work containing a QR stack in the intrinsic region.

A generic photoluminescence sample is represented in Figure 4.6 containing a quantum ring stack, the stack can have different amount of QR layers and different spacing thickness between the QR layers. The spacing thickness between consecutives QR layers is the sum of the thickness of GaAs cold cap layer and GaAs layer.

The photoluminescence samples in tables 4.1 and 4.2 are analysed in subsection 5.2.1 and 6.3.1, respectively. The samples in table 4.1 were designed to study the effect of increasing the amount of QR layers on photoluminescence spectra. The samples in table 4.2 were developed to understand the effect of decreasing the spacing between QR on photoluminescence and time-resolved photoluminescence.

Table 4.1. Quantum ring stack parameters of photoluminescence samples 1x-XDM364 (1x), 10x-XDM426 (10x,10nm) and 50x-XDM497 (50x,10nm), where amount of QR layers is increased. Samples are grown on n-type GaAs substrates. The QR stack is deposited after a 300 nm of undoped GaAs buffer layer and is capped by an undoped GaAs of 100 nm. Photoluminescence of these samples is presented in subsection 5.2.1.

Sample name	*Number of QR layers*	*GaAs Cold Cap(nm)*	*GaAs (nm)*	*Spacing (nm)*
1x-XDM364 *(1x)*	1	5	-	-
10x-XDM426 *(10x,10nm)*	10	5	5	10
50x-XDM497 *(50x,10nm)*	50	5	5	10

Table 4.2. Quantum ring stack parameters of photoluminescence samples: 40nm-PJC645 (10x,40nm), 10nm-QDM672 (20x,10nm) and 6nm-QDM693 (20x,6nm), where spacing between QR layers is decreased. Samples are grown on n-type GaAs substrates. The QR stack is deposited after a 300 nm of undoped GaAs buffer layer and is capped by an undoped GaAs of 100 nm. Time resolved photoluminescence of these samples is presented in subsection 6.3.1.

Sample name	*Number of QR layers*	*GaAs Cold Cap(nm)*	*GaAs (nm)*	*Spacing (nm)*
40nm-PJC645 *(10x,40nm)*	10	5	35	40
10nm-QDM672 *(20x,10nm)*	20	5	5	10
6nm-QDM693 *(20x,6nm)*	20	3	3	6

The solar cell devices studied in this thesis contain a QR stack in the intrinsic region, full description of the device structure is shown in Figure 4.7. The main QR stack parameters of the different devices are summarised in tables 4.3 and 4.4, such as number of QR layers, spacing between them as well as total QR stack thickness and density. Table 4.3 shows the different solar cells analysed in chapter 5 and 6, these devices are designed to study the effect on the electrical performance of increasing the amount of QR layers and decreasing the spacing between QR layers. Table 4.2 shows the specific thickness of GaAs cold cap and GaAs layer for a total spacing of 40, 10 and 6 nm. QR solar cell shown in table 4.4 and its correspondent GaAs solar cell were

grown and processed at Lancaster university before I started the PhD, this set of solar cells is analysed in section 6.4. The two sets of QR solar cells were processed at the same time as its correspondent reference GaAs solar cell.

Table 4.3. Quantum ring stack parameters of solar cell devices: A-XDM563 (10x,40nm), B-XDM557 (40x,10nm) and C-XDM571 (10x,6nm). These QRSCs were processed and measured at the same time as reference GaAs solar cell XDM518. Electrical characterization of these devices is shown in chapters 5 and 6.

Device name	*Number of QR layers*	*Spacing (nm)*	*Total QR stack thickness (nm)*	*QR stack density (nm^{-1})*
A-XDM563 *(10x,40nm)*	10	40	400	0.025
B-XDM557 *(40x,10nm)*	40	10	400	0.10
C-XDM571 *(10x,6nm)*	10	6	60	0.17

Table 4.4. Quantum ring stack parameters of solar cell device QRSC-A0503 (10x,40nm), processed and measured at the same time as its correspondent reference GaAs solar cell A0502. The electrical characterization of these devices is shown in section 6.4.

Device name	*Number of QR layers*	*Spacing (nm)*	*Total QR stack thickness (nm)*	*QR stack density (nm^{-1})*
QR SC-A0503 *(10x,40nm)*	10	40	400	0.025

Chapter 5

Growth and Characterization of Type-II GaSb/GaAs Quantum Ring Solar Cells

This chapter is divided into three parts, firstly growth and design of the reference GaAs solar cell (5.1), secondly study of quantum ring (QR) stack growth parameters increasing sub-bandgap light absorption (5.2) and improving hole transport through the QR stack (5.3).

Table 4.3 in section 4.1.4 in *Experimental Techniques* chapter summarizes the growth parameters of the QR stack for the three QRSC studied: number of QR layers, spacing between consecutive QR layers, QR stack thickness and the linear density of the QR stack along the growth direction (no. of QR layers/QR stack thickness). In each case, the QR stack (of 400 or 60 nm) is placed in the middle of the i-region of the device that is 500 nm thick. Figure 5.1(a) shows the distribution of the QR layers within the i-region for the three QRSCs: A-XDM563, B-XDM557 and C-XDM571. The low QR stack density device A, has 10 QR layers and 40 nm spacing. The high QR stack density devices B and C, have 40 QR layers with 10 nm spacing, and 10 QR layers with 6 nm spacing, respectively. In Figure 5.1(b) the band structure of the i-region is sketched for device A-XDM563 (10x, 40 nm), where the QR stack thickness of 400 nm is placed in the depletion region.

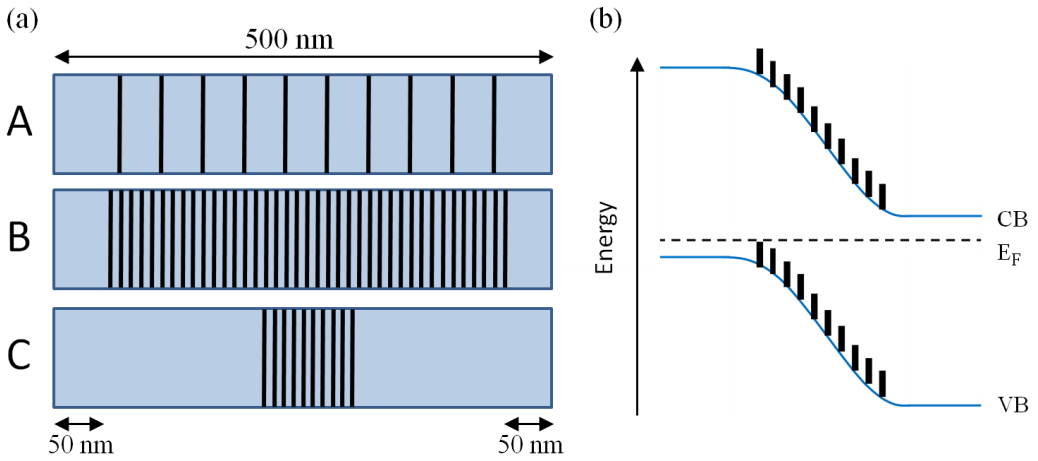

Figure 5.1. (a) Schematic diagram of the distribution of the GaSb layers within the intrinsic region for each QRSC: A-XDM563 (low QR stack density with 10 QR layers spaced by 40 nm), B-XDM557 (high QR stack density with 40 QR layers spaced by 10 nm) and C-XDM571 (high density sample with 10 QR layers spaced by 6 nm). (b) Sketch of the band structure for device A-XDM563 (10x, 40 nm), just the depletion region is shown.

5.1 Solar cell design and MBE growth

Optimizing and evaluating the device structure of the reference GaAs SC is crucial for achieving high efficiency IBSCs. As shown in Figure 5.2(b), the reference GaAs SC consists of a p-i-n structure, with 500 nm i-region, processed using a 0.72 mm^2 Spider Web mask (more details presented in section 4.5 of *Experimental techniques* chapter). In Figure 5.2(a) the band structure of the reference device is simulated using SimWindows [120], showing the AlGaAs window layer placed for avoiding surface recombination. From C-V measurements doping concentration versus depletion region width is obtained, see *Background Theory* chapter section 2.4.1. The background doping is identified as $6x10^{15}$ cm^{-3} from the logarithmic scale shown in Figure 5.2(c). This p-type background doping comes from carbon contamination inside the growth chamber and the obtained value is in agreement with literature values [121], showing low impurity concentration during growth conditions. Figure 5.2(d) shows the voltage dependence of the depletion region width, at zero applied voltage (working conditions for a solar cell) the depletion width of the reference GaAs solar cell device is 560 nm, 12% larger than the grown intrinsic region.

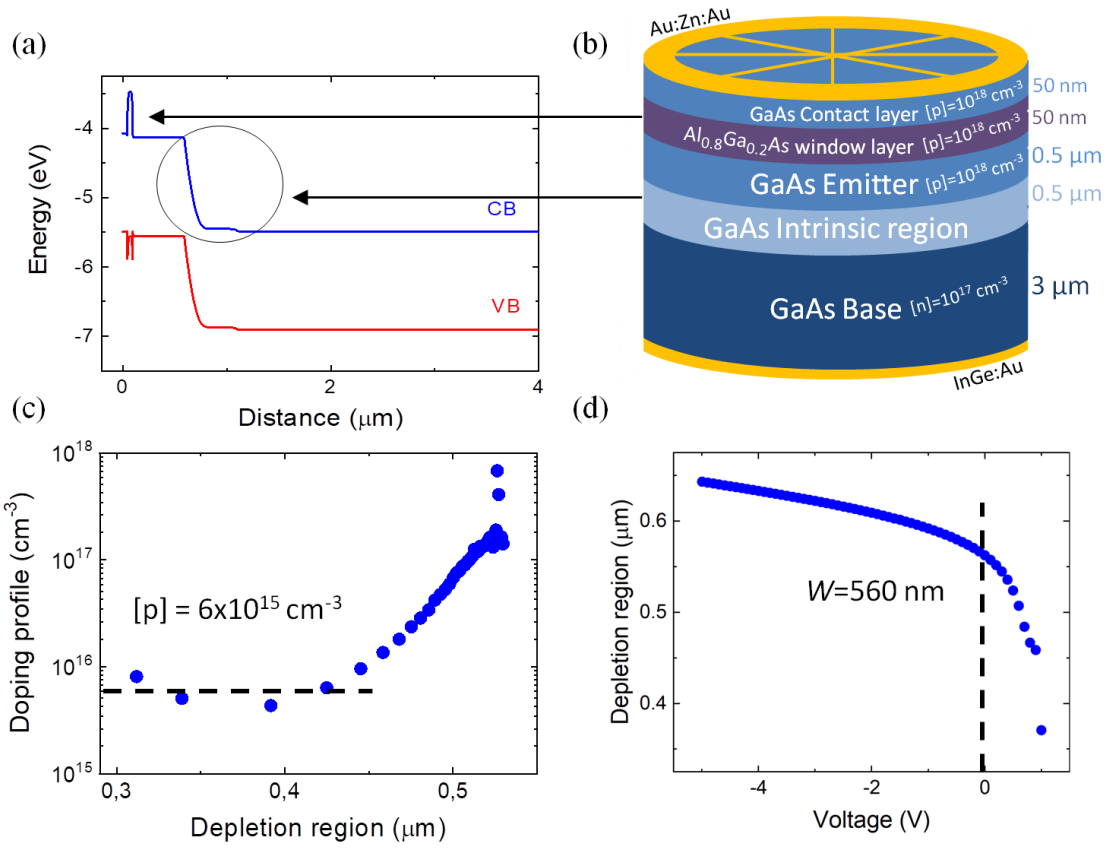

Figure 5.2. (a) Band structure simulation of the reference p-i-n GaAs solar cell containing a $Al_{0.8}Ga_{0.2}As$ window contact layer using Sim Windows. (b) Grown and processed structure of the reference p-i-n GaAs solar cell containing an $Al_{0.8}Ga_{0.2}As$ window layer. (c) Logarithmic scale of doping concentration versus depletion region for the reference cell, showing background p-doping. (d) Depletion region versus voltage, the depletion width at zero voltage (W) is 560 nm.

5.2 Increasing sub-bandgap light absorption

Device B-XDM557 was developed to study the effect of increasing the amount of QR layers up to 40 by keeping the same QR stack thickness (400 nm), increasing therefore the QR stack density to 0.1 nm^{-1} and decreasing the spacing down to 10 nm between consecutive QR layers. In the type-I In(Al,Ga)As/GaAs system strain balance techniques or thick spacers are needed for achieving high crystal quality in highly dense QD SC. Sugaya et al. managed to grow up to 400 QD layers while preserving high material quality. In their study sub-bandgap light and short-circuit current increases while increasing the number of QD layers up to 150 [63]. Here we present for the first time a study on the effect of the amount of QR layers in highly densely packed type-II

GaSb/GaAs QRSC, showing how the crystal quality is preserved and the device performance is enhanced.

5.2.1 Material characterization

In the TEM images shown in Figure 5.3, the GaSb layers can be identified containing GaSb quantum nanostructures with a ring shape. In the inset of Figure 5.3(a) individual GaSb QR are shown, with a size of ~2 nm height, an outer diameter of ~20 nm and an inner diameter of ~10 nm. The spacing is also determined as 10.4 nm, very close to the intended 10 nm. Figure 5.3(a) and (b) show how the two materials grow coherently along the [001] direction, exhibiting good quality material showing pristine interfaces without dislocations or defects. Also, no vertical aligned nanostructures are observed showing negligible accumulated strain in the growth direction. Both features, the absence of dislocations and vertical alignment, show how efficient the quantum rings are at relieving strain making them suitable for ultra-high stack density devices.

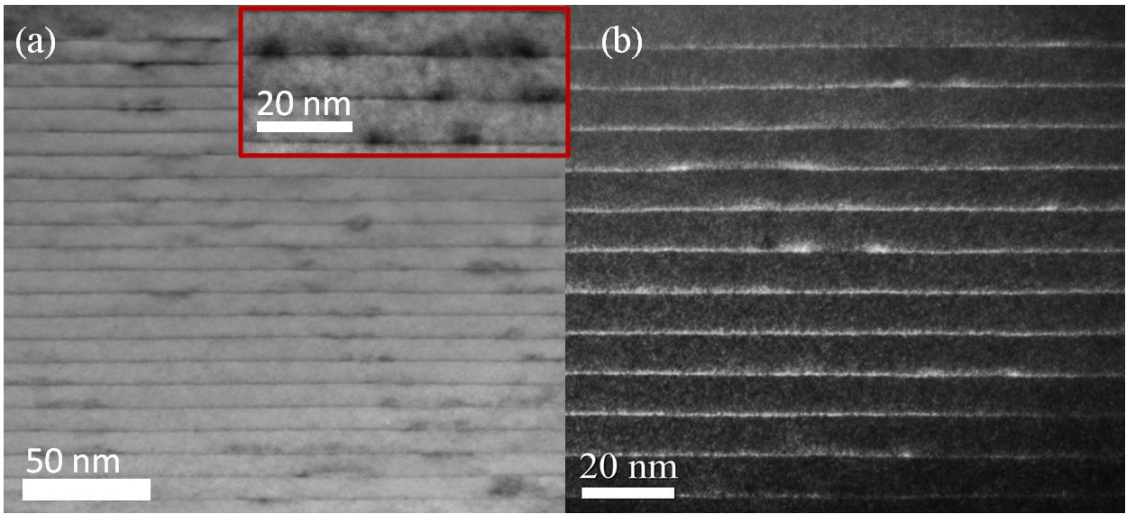

Figure 5.3. Cross-section transmission electron microscopy along the growth direction for device B-XDM557 (40 QR layers spaced by 10 nm). (a) Bright field 002 imaging conditions, GaSb wetting layer and QRs are identified in each layer, vertical alignments are not observed. The inset shows a magnification picture where the two lobes of the QR are clearly shown. (b) Dark field 002 imaging conditions, defects and/or dislocations are not observed indicating good crystalline quality material.

Figure 5.4(a)-(c) shows high resolution x-ray diffraction (XRD) spectra for device A-XDM563 (10x, 40nm) & B-XDM557 (40x, 10nm), the different fringes show GaAs/GaSb interfaces. As shown in Figure 5.4 (a)-(b) the XRD fitting curve is in

agreement with the experimental data, showing less than 10% error between the expected grown spacing and the one obtained from XRD fitting curve. In Figure 5.4(d) the photoluminescence (PL) spectra of the PL samples summarised in table 4.1 is shown, the PL intensity of wetting layer (WL) and QR transition energy is enhanced as the number of QR layers is increased from 1 to 50. The transition energy of the WL and QR are identified as 0.94 and 1.17 µm, respectively, and are the same for the three samples. Increasing the number of layers has no effect on the size and composition of the nanostructures, so that the energy band diagram is equivalent among the samples.

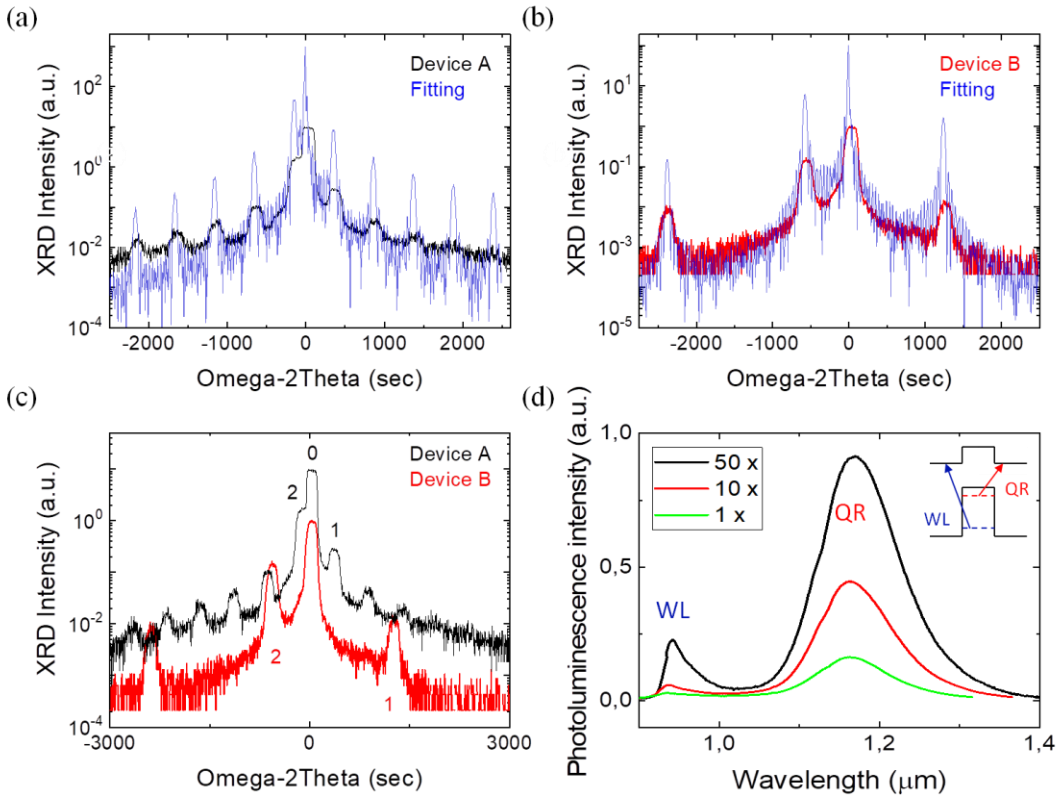

Figure 5.4. (a)-(c) High resolution x-ray diffraction (XRD) for devices A-XDM563 (black) & B-XDM557 (red). (b)-(c) show XRD for each device and its corresponding fitting curve. (c) compares the XRD of the two devices, showing GaAs substrate peak (0) and the first two GaSb satellite peaks (1 & 2). (b) Photoluminescence spectra is measured at 4 K for three samples, where the spacing is 10 nm: 50 QR layers (50x - black), 10 QR layers (10x - red) and 1 QR layer (1x - green). The sketch in the inset shows the two energy transitions, QR at 1.17 µm and WL at 0.94 µm.

5.2.2 Device characterization

Figure 5.5 summarises the main electrical characterisation for devices A-XDM563 (10x, 40nm), B-XDM557 (40x, 10nm) and the reference solar cell (Ref). External quantum

efficiency (EQE) in linear scale is shown in Figure 5(a). QRSC A exhibits the typical reduction in photocurrent from n-region (emitter) in type-II GaSb/GaAs SC, related to hole trapping when migrating to p-region (base) [21]. In the case of QRSC B, in addition to emitter reduction, the photocurrent from the base also decreases, the extra QR layers act as barriers for the carriers migrating toward n-region. Figure 5(b) shows the large enhancement in sub-bandgap light absorption, the contribution of WL and QR to the extracted photocurrent is increased by a factor 4, linearly with the number of layers. The absorption enhancement results in a corresponding EQE increase, from 1.3% to 4.3% for the WL (λ = 0.94 μm), and from 0.04% up to 0.15 % for the QR (λ = 1.16 μm) when increasing the number of QR layers from 10 to 40 while increasing the QR stack density. In spite of the enhancement in sub-bandgap photocurrent, the supra-bandgap contribution is compromised and so the short-circuit current is not enhanced. As shown in Figure 5(c), the maximum current and voltage obtained from both QRSCs, A-XDM563 (10x, 40nm) and B-XDM557 (40x, 10nm), is similar, without any improvement in the device performance tested under 1 Sun illumination and AM1.5g conditions. Table 5.1 summarises the photovoltaic parameters obtained from Figure 5(c), see *Background Theory* chapter section 2.4.2. Electroluminescence (EL) was also measured, to study the radiative emission. Figure 5(d) shows EL spectra at 10 K. The QR transition identified at 1.05 eV is enhanced by a factor 4 for QRSC B-XDM557 (40x, 10nm) with respect to QRSC A-XDM563 (10x, 40nm). The vertical dotted lines indicate deep level emission at 0.92, 1.15 and 1.33 eV believed to be related to donor/acceptor defect complexes within the highly doped regions of the device [122]. GaAs bulk (band-band) transitions correspond to 1.45 eV. The WL transition is expected around 1.3 eV, however it is close to a deep level transition and the peak is not reliably resolved. The increased absorption in sub-bandgap light observed in EQE at room temperature corresponds with the increase in electroluminescence emission

observed at low temperature. In chapter 6, this correspondence will be exploited to obtain information about recombination within the device.

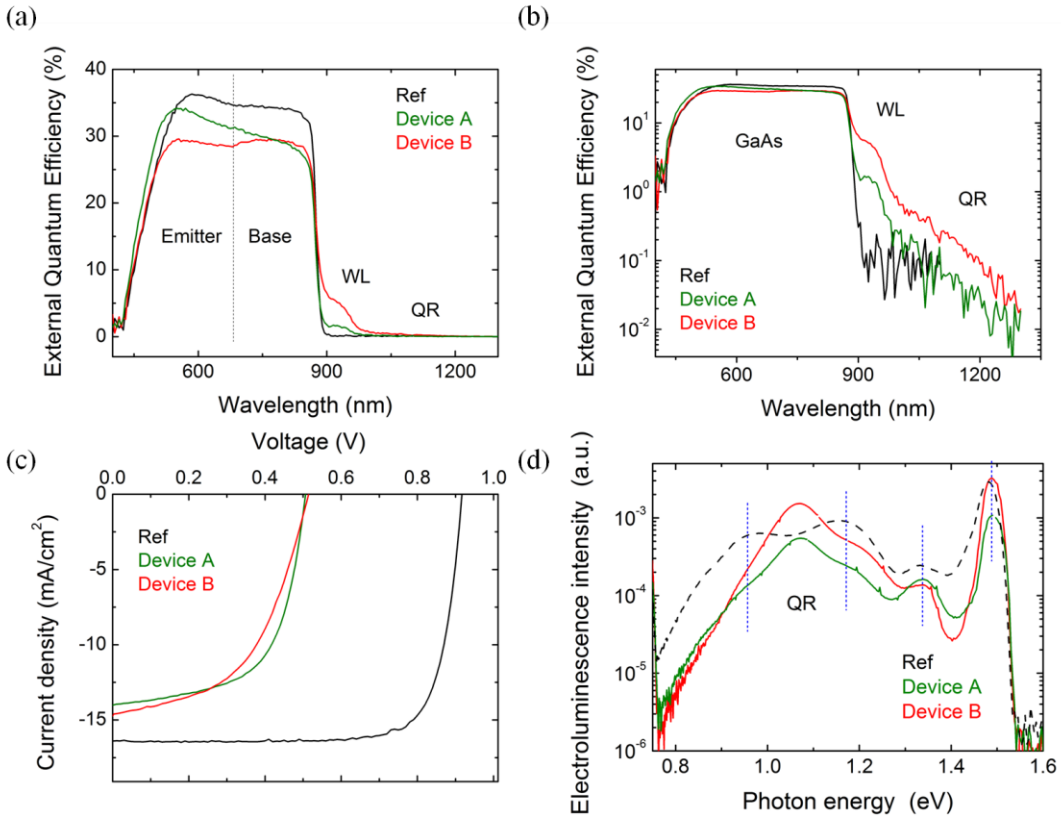

Figure 5.5. Electrical characterization for the reference cell in black, device A-XDM563 (10x 40nm) in green and device B-XDM557 (40x, 10nm) in red. (a) Room temperature external quantum efficiency (EQE) in linear scale. (b) EQE in logarithmic scale. (c) J-V curve under 1 Sun AM1.5g illumination. (d) Electroluminescence spectra measured at 10 K. The dotted blue lines show deep level emission not related to QR energy levels as they are also present in the reference cell.

In Table 5.1 the short-circuit current (J_{SC}), open-circuit voltage (V_{OC}), fill factor (FF), conversion efficiency and series resistance (R_S) are summarised. The reference cell has an efficiency of 11.9% in agreement with literature for GaAs cells without AR coating, FF of 0.79, V_{OC} of 0.92 V (60% of the GaAs energy gap) and J_{SC} of 16.4 mA/cm^2. When adding QRs the FF is reduced to 0.5 - 0.6 due to an increase in R_S, and V_{OC} decreases to ~0.5 Vdue to an increase in dark current from the increased recombination in QRSCs. J_{SC} and consequently, the conversion efficiency, shows different behaviour depending on QR stack parameters (see section 5.3). Between QRSC A-XDM563 (10x, 40nm) and B-XDM557 (40x, 10nm) there is no major difference in the performance

under 1 Sun illumination; both have an efficiency of ~4% and J_{SC} is slightly larger for device B, around 4%.

Table 5.1. Photovoltaic parameters obtained from J-V curve measured under 1 Sun illumination using a filter AM1.5g and in darkness, for reference SC and QRSC devices: A-XDM563 (10x, 40nm) and B-XDM557 (40x, 10nm).

Device	*Short-circuit current (J_{SC}) [mA/cm^2]*	*Open-circuit voltage (V_{0C}) [V]*	*Filling factor (FF)*	*Conversion efficiency [%]*	*Series resistance (R_S) [Ω]*
***Reference**-XDM518*	16.4	0.92	0.79	11.9	30
***A**-XDM563 (10x,40nm)*	14.0	0.50	0.61	4.3	100
***B**-XDM557 (40x, 10nm)*	14.6	0.51	0.51	3.9	170

5.3 Improving hole transport through the QR stack

Device C-XDM571 was developed to study the effect of decreasing the spacing between consecutives QR layers down to 6 nm by keeping the same number of QR layers (10), therefore increasing the QR stack density and decreasing the QR stack thickness down to 60 nm. In the type-I In(Al,Ga)As/GaAs system, a low spacing is avoided in order to conserve the crystal quality and for avoiding tunneling [123, 17]. Here we present for the first time, a study on the effect of spacing in densely packed type-II GaSb/GaAs QRSC, showing how the crystal quality is preserved and the device performance is enhanced.

5.3.1 Structural analysis

In Figure 5.6(a)-(b) the high resolution x-ray diffraction (XRD) for the devices A-XDM563 (10x, 40nm) and C-XDM571 (10x, 6nm) is shown. From the XRD spectra the different GaSb satellite peaks, labelled as 1 and 2, can be distinguished. The XRD fitting curve and the experimental data of device C are in agreement. The obtained spacing is 5.3 nm compared to the expected 6 nm from growth rate calibrations. Figure 5.6(c)-(d) shows the dark and bright-field cross-section HRTEM images of device C-

XDM571 (10x, 6nm). The 10 GaSb layers are identified with a measured spacing of 6.6 nm between them, with each layer containing a GaSb WL, GaSb QRs as well as other nanostructures. The structure is dislocation and defect free, showing good material quality despite some Sb segregation. Nanostructures vertically aligned along the growth direction are not observed, suggesting that quantum rings are efficient at relieving the accumulated strain, and close packed QR layers can be grown without degrading the material quality. From both, TEM and XRD measurements, device C-XDM571 with 6 nm spacing between QR layers shows good crystal quality.

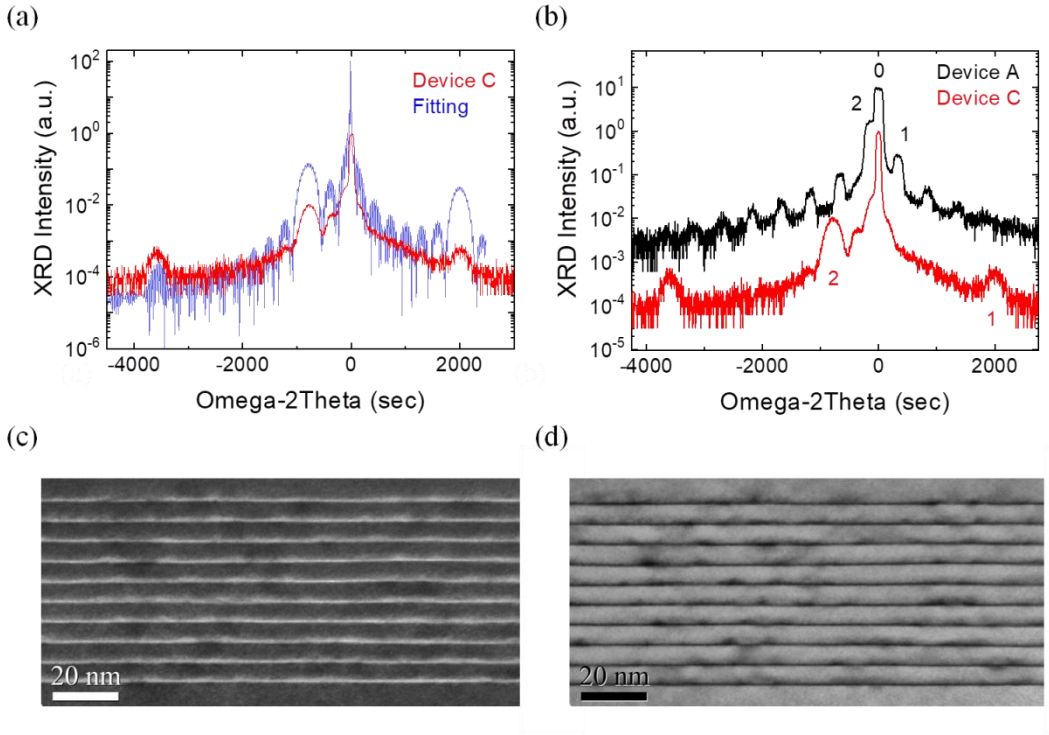

Figure 5.6. (a)-(b) High resolution x-ray diffraction for device A-XDM563 (10x, 40nm) in black and C-XDM571 (10x, 6nm) in red, as well as for fitting curve of device C XRD in blue. Showing GaAs substrate peak (0) and GaSb satellite peaks (1 & 2). (c)-(d) Cross-section high resolution transmission electron microscopy along the growth direction in dark field (c) and bright field (d), for device C-XDM571 (10x, 6nm). GaSb wetting layer and nanostructures are identified.

5.3.2 Device characterization

Figure 5.7(a) shows the External Quantum Efficiency spectra measured at room temperature in linear scale for both the reference and the QRSC A-XDM563 (10x, 40nm) and C-XDM571 (10x, 6nm). The QR stack is 60 nm thick in device C compared

to 400 nm in device A. We believe this is the main parameter responsible for the enhancement observed in the base photocurrent. The EQE increases from 30% to 35% for the wavelength range between 700-900 nm. The QR stack acts as a barrier for holes photogenerated in the base migrating towards the p-side. A thinner stack will therefore increase the probability of a hole to reach the other side. No noticeable increase is observed in sub-bandgap photocurrent, as shown in Figure 5.7(b) in logarithmic scale. The improved hole transport through the QR stack enhances supra-bandgap photocurrent, resulting in an increase in the total current obtained from the solar cell, as shown in Figure 5.7(c). Table 5.2 summarises the photovoltaic parameters obtained from the J-V curve measured under 1 Sun illumination at AM1.5g conditions plotted in Figure 5.7(c). In Figure 5.7(d) the electroluminescence spectra measured at 10 K is shown. As discussed in the previous section, deep level emission is present in all the SCs, reference and QRSCs. The QR peak is enhanced by a factor of 2 for device C-XDM571 (10x, 6nm) compared with A-XDM563 (10x, 40nm), showing an enhancement in radiative recombination when decreasing the spacing and increasing the QR stack density. In chapter 6, a full description of different characterization techniques including electroluminescence is used to explain the origin and the consequences of the radiative recombination enhancement in high QR stack density type-II QRSC.

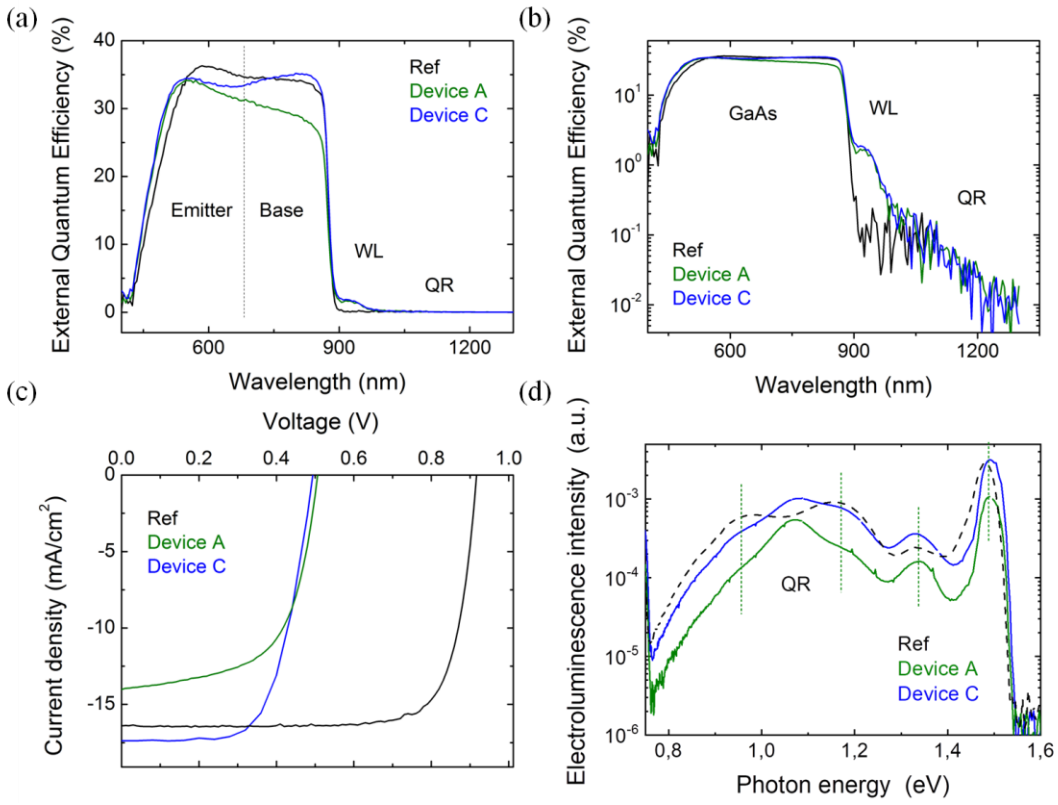

Figure 5.7. Electrical characterization for reference cell (black), device A-XDM563 (10x 40nm) (green) and device C-XDM571 (10x, 6nm) (blue). (a) Room temperature External Quantum Efficiency (EQE) spectra in linear scale. Base, emitter and WL photocurrent contribution are identified. (b) EQE spectra in logarithmic scale, showing the WL and QR transitions up to 1300 nm. (c) J-V curve under 1 Sun AM1.5g illumination. (d) Electroluminescence spectra measured at 10 K from the reference cell (black), device A-XDM563 (10x 40nm) (green) and device C-XDM571 (10x, 6nm) (blue). The dotted blue lines show deep level emission not related to QR energy levels, as they are also present in the reference cell.

As summarised in Table 5.2, device C-XDM571 (10x, 6nm), compared with device A-XDM563 (10x, 40nm), improves the different photovoltaic parameters except for V_{OC}, which remains the same. J_{SC} increases 24 %, reaching 17.4 mA/cm^2 and FF increases 6%, resulting in an increase of 30% in conversion efficiency. The performance is improved in device C, but series resistance is doubled. Comparing with the reference, device C shows an enhancement of 6% in J_{SC}, however FF and V_{OC} are reduced when inserting QR within the device and conversion efficiency is reduced by a factor of 2.

Table 5.2. Photovoltaic parameters obtained from J-V curve measured under 1 Sun illumination using a filter AM 1.5G and in darkness, for reference SC and QRSC devices: A-XDM563 (10*x*, 40nm) and C-XDM571 (10*x*, 6nm).

Device	*Short-circuit current (J_{SC}) [mA/cm^2]*	*Open-circuit voltage (V_{OC}) [V]*	*Filling factor (FF)*	*Conversion efficiency [%]*	*Series resistance (R_S) [Ω]*
***Reference**-XDM518*	16.4	0.92	0.79	11.9	30
***A**-XDM563 (10x,40nm)*	14	0.50	0.61	4.3	100
***C**-XDM571 (10x,6nm)*	17.4	0.49	0.65	5.6	230

5.4 Summary

In summary, both high QR stack density QRSC B-XDM557 (40x, 10nm) and C-XDM571 (10x, 6nm) show high crystal quality, without dislocations even when 40 QR layers are grown and the spacing is reduced to 6 nm. Multi-QR stacks can be grown without engineering strain balance layers in type-II GaSb/GaAs QRSC. Furthermore, the size and composition of the QRs are conserved, without modifying the band structure of the material. When increasing the number of QR layers to 40 while decreasing the spacing to 10 nm, sub-bandgap light absorption at room temperature, and QR radiative recombination at low temperature, are enhanced a factor 4. However, due to reduction in supra-bandgap photocurrent, the short-circuit current is not increased, and neither is the conversion efficiency. When decreasing the spacing to 6 nm while keeping 10 QR layers, hole transport through the QR stack is improved due to tunneling enhancing supra-bandgap photocurrent. Consequently, short-circuit current and conversion efficiency have the highest values among the devices studied in this work. However, the addition of QRs results in large reduction in open-circuit voltage preventing high conversion efficiency as expected in IBSC. This point will be addressed in the next chapter.

Chapter 6

Quantum Ring Hole Dynamics: Charging and Discharging Mechanisms, and Quantum Ring Recombination

This chapter is focused on the main limitations of type-II QRSC working as an IBSC. The devices should fulfill the two working principles of an IBSC: two photon photocurrent (TPPC) and open-circuit voltage (V_{OC}) conservation. TPPC has been detected at low temperature previously [86, 124, 87], here we study in detail which mechanisms prevent its detection at room temperature and its low value at low temperature. V_{OC} recovery has been studied under 2500 sun concentration before [95], however full recovery has not been observed. Here, we address the main limitations for high V_{OC} in type-II QRSC studying recombination within the device. Under two light sources TPPC is detected and analysed (6.1), identifying hole charging and discharging dynamics, yielding the hole cross-section for optical and capture processes (VB to QR), and the temperature dependence of hole emission rate (QR to VB). Under light concentration V_{OC} is partly recovered and investigated (6.2), establishing the dominant recombination mechanisms from photocurrent-voltage behaviour, and highlighting the importance of QR occupancy in the Fermi level. At different injection current (6.3), the limiting recombination processes in the device are determined from the electroluminescence spectra, corresponding with the results obtained via concentration measurements, demonstrating the V_{OC}-EL reciprocity relation [125]. And, under hydrostatic pressure (6.4), V_{OC} increase is studied and compared with the effect of

decreasing temperature, emphasizing the importance of reducing recombination in type-II QRSC.

6.1 Two-Photon Photocurrent (TPPC)

TPPC measurements and analysis were performed at Nelson Mandela University (South Africa) in collaboration with Prof. Magnus C. Wagener. As shown in Figure 6.1, after photogenerating an electron-hole pair the following processes can happen:

1. Hole trapping from VB and WL to QR
2. Radiative recombination between electrons in CB and holes in QR
3. Hole thermionic emission from QR to VB
4. Hole optical generation from QR to VB

The rates of processes 1 to 4 describe the hole dynamics in QR. Referring to the rate of process 1 as (1) and the same for the other processes. If (1) ~ (4) high TPPC is achieved. However, if (1) >> (4) holes are accumulated in QR levels enhancing (2) and reducing V_{OC} if (2) >> (4). And if (3) >> (4) carriers are emitted thermally from QR without absorbing a second photon and then suppressing TPPC.

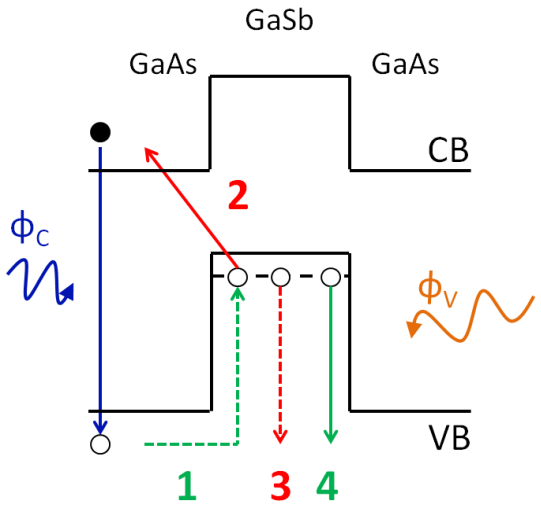

Figure 6.1. Processes involved in hole QR dynamics: hole captured in QR (1) (green dotty line), recombination with electron in CB (2) (solid red line), thermionic emission to VB (3) (red dotty line) and optical emission to VB by absorbing a second photon (4) (green solid line). Green lines indicate the processes required for IBSC behaviour, while red lines show process that degrades the IBSC performance.

Ideally, once the QR energy levels are photo-filled by hole trapping; holes need to be pumped to VB by optical generation, before holes are radiatively recombined with electrons in CB for avoiding V_{OC} reduction, and before holes are emitted to VB by thermionic emission preventing TPPC detection. To achieve IB behaviour and fulfill the two working principles, the trapped hole in the QR energy level should be emitted optically toward the VB by absorbing a second photon (photo-emission source), completing the two transitions and generating TPPC. However, both processes need to be balanced, trapping for photo-filling the QR and optical generation to pump holes to VB. If the hole trapping rate is much larger than the optical emission rate, holes will be lost by recombination with electrons in the CB.

In the experiment, the excess of electron and hole concentrations, Δn and Δp, as well as the QR hole occupation density, *N*, are described by the following set of kinetic equations [119]- developed by Prof. Magnus C. Wagener, Nelson Mandela University, SA,

$$\frac{\partial \Delta n}{\partial t} = \alpha \phi_C - \frac{\Delta n}{\tau} - \frac{\Delta n}{\tau_{QR}} - \mu_e \frac{dE}{dx} \Delta n \tag{6.1}$$

$$\frac{\partial \Delta p}{\partial t} = \alpha \phi_C - \frac{\Delta p}{\tau} + (e_{th} + e_T + \sigma_V^o \phi_V) N - C_h (N_0 - N) \Delta p - \mu_h \frac{dE}{dx} \Delta p \tag{6.2}$$

$$\frac{\partial N}{\partial t} = C_h (N_0 - N) \Delta p - (e_{th} + e_T + \sigma_V^o \phi_V) N - \Delta n / \tau_{QR} \tag{6.3}$$

where α the absorption coefficient, ϕ_C and ϕ_V are the illumination flux of photo-filling source (VB-CB) and photo-emission source (QR-VB), $\tau^{-1} = \tau_{BB}^{-1} + \tau_{SRH}^{-1} + \tau_{Auger}^{-1}$, τ_{QR} is the lifetime of holes localized in QR recombining with electrons in CB, μ_e and μ_h are the electron and hole mobility, e_{th} and e_T the non-radiative rates for thermionic emission and tunneling, $\sigma_V^o \phi_V$ is the optical hole emission rate where σ_V^o is the optical cross-section of sub-bandgap illumination source, C_h the hole capture coefficient is given by $C_h = < v_h > \sigma_h$ where $< v_h >$ is the thermal velocity for holes and σ_h the hole capture cross-section, and $N_0 = N_{QR}/w$ is density of QR hole states where N_{QR}=

(surface state density)*x*(number of QR layers), and w is the width of space-charge region.

From the above equations the optical hole emission current, J_h, is obtained as:

$$J_h = q\left\{\frac{K}{\sqrt{K^2-4bC_h\alpha\phi_C}} - 1\right\}\frac{\sigma_V^o}{2\sigma_h}\phi_V \tag{6.4}$$

where

$$K = a - \{\sigma_V^o\phi_V + e_{th} + e_T\}b \tag{6.5}$$

and

$$a = 1/\tau + C_hN_0 + \left(\mu_h\frac{dE}{dx}\right),\ b = \frac{C_hN_0}{C_h\Delta p + e_{th} + e_T + \sigma_V^o\phi_V}\,. \tag{6.6}$$

Steady-state and time-dependent hole emission measurements at low temperature are shown in Figure 6.2(a) and (b). Figure 6.2(a) shows how J_h saturates at high ϕ_C ~ 10^{17} $cm^{-2}s^{-1}$ and by fitting the experimental data to eq. 6.4 we obtain a σ_h of ~ 10^{-13} cm^2 corresponding to a *hole trapping rate of 10^4 s^{-1} at 17 K* ($\sigma_h\phi_C$). Similar values have been reported by Michigan University (σ_h ~ 10^{-16} - 10^{-13} cm^2 for a bias of 0.8 - 2.3 V) [20] been few orders of magnitude lower than the values reported for type-I InAs/GaAs (σ_h ~ 10^{-12} - 10^{-10} cm^2) [102, 101, 100]. From *room temperature* measurements *hole trapping rate increases up to 10^9 s^{-1}*. Table 6.1 shows the fitting parameters used in eq. 6.4 for the simulation of the photocurrent plot in Figure 6.2(a). Figure 6.2(b) shows the decay time of J_h after suspending the photo-filling source (ϕ_C) for different values of ϕ_V. From the exponential fit to the data carrier lifetime (inverse of rate) is obtained as a function of ϕ_V, as shown in the inset of Figure 6.2(b). From the slope of the emission rate we obtain σ_V^o and from $\phi_V = 0$ intercept we extract the non-radiative emission, e_{nr} ($e_{nr} = e_{th} + e_T$). The obtained σ_V^o is ~ 10^{-16} cm^2, three orders of magnitude lower than σ_h, revealing that hole QR dynamics is dominated by trapping instead of by optical emission, enhancing recombination and limiting TPPC. At low temperature *the optical emission rate ($\sigma_V^o\phi_V$) ~ 10^0 s^{-1}* obtained under a flux of 8.8x10^{15} $cm^{-2}s^{-1}$ is two orders of

magnitude larger than the quantum tunneling emission rate (e_T) ~ 10^{-2} s^{-1}, meaning that holes in QR energy level are pumped to VB by absorbing a second photon hence generating TPPC, instead of escaping to VB through non-radiative process. At low temperature thermionic emission is considered negligible and tunneling dominates non-radiative escape processes.

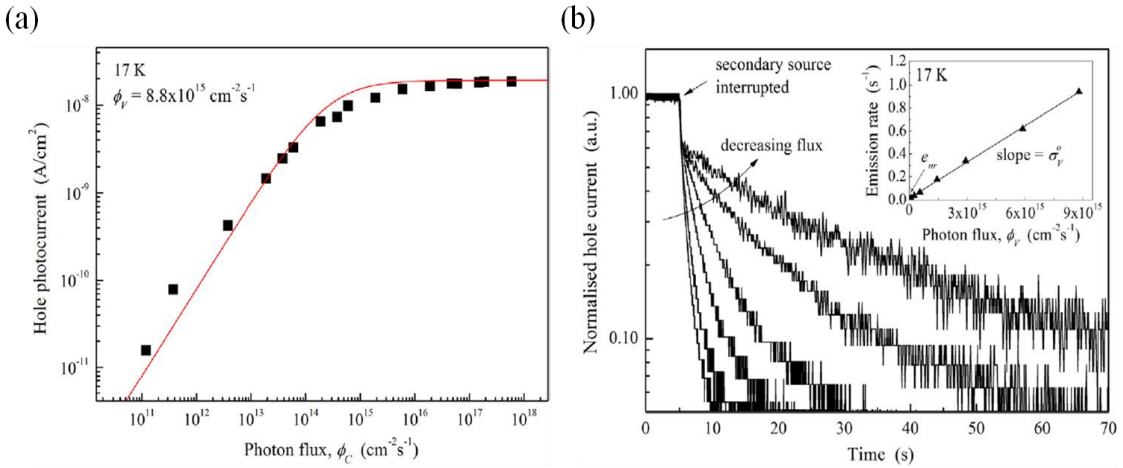

Figure 6.2. (a) Dependence of the optical hole emission current, J_h, of the GaSb/GaAs QRSC on the photo-filling intensity, ϕ_C. The solid red line represents the best fit of eq. 6.4. (b) Normalized plot of J_h, after suspending photo-filling source. Photo-emission flux density, ϕ_V, was decreased gradually. The inset shows the emission rates from the initial exponential decay of each transient. The optical cross-section and non-radiative hole escape rates were determined from the slope and the $\phi_V = 0$ intercept, respectively [119].

Table 6.1. Fitting parameters used in eq. 6.4 for the simulation of the photocurrent plot in Figure 6.2(a) measured at 17 K [119].

Parameter	*Value*
N_{QR}	*1.2 x 10^{11} cm^{-2}*
σ_h	*(1.2±0.3) x 10^{-13} cm^2*
σ_V^0	*(1.0±0.1) x 10^{-16} cm^2*
e_{th}	Neglected
e_T	*(0.010±0.006) s^{-1}*
α	900 cm^{-1}
dE/dx	1.4x10^7 V/cm^2

Figure 6.3 shows temperature dependence of emission rate. By measuring time-dependent photocurrent shown in Figure 6.2(b) at different temperatures we obtain σ_V^o

and e_{nr} temperature dependence. The optical hole emission rate is obtained by multiplying σ_V^o by the optical flux ϕ_V. *At low temperature* the rate is 10^4 s^{-1} compared to *10^0 s^{-1} for tunneling emission*, and optical generation dominates generating TPPC. However, *at room temperature the optical rate drops down to 10^0 s^{-1}* and the *thermionic emission* increases exponentially reaching a rate of *10^4 s^{-1}*, suppressing TPPC at high temperatures. From Fig. 6.3 the activation energy for thermionic emission is obtained as 150 meV, in good agreement with 220 meV obtained by Michigan university [90].

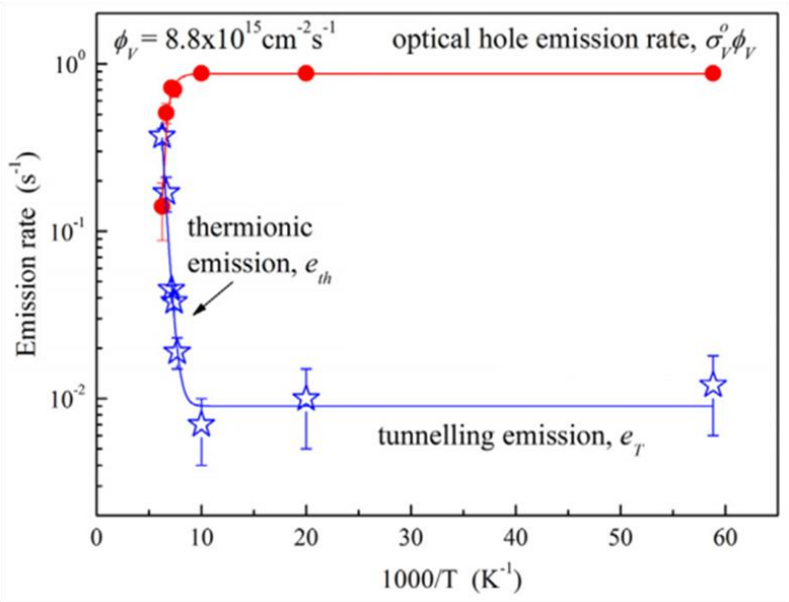

Figure 6.3. Arrhenius plot for hole emission rate from the QR ground level to the VB. At low temperature the main emission process is optical excitation (red dots). As the temperature increases the contribution of non-radiative process (blue stars) increases rapidly. At temperatures above 100 K, thermionic emission (e_{th}) dominates over quantum tunneling (e_T) and optical emission. [119]

In summary, the two non-radiative recombination processes studied at *room temperature are hole trapping with a rate of 10^9 s^{-1}*, and *hole thermionic emission with a rate of 10^4 s^{-1}* (under 4000 suns flux). Both processes determine QR hole occupancy and the quenching temperature of TPPC. Trapping increases recombination within the device, and thermionic emission prevents holes from being pumped optically, suppressing two-photon photocurrent that is essential for achieving IB behaviour. Both non-radiative process need to be addressed before obtaining high electrical performance in type-II GaSb/GaAs QRSCs.

6.2 High Light Concentration

Under high concentration, carrier thermalization (thermionic emission) is expected to be overcome by optical excitation (optical emission). In this case, hole lifetime in QR states increases, allowing optical absorption and not thermal escape to dominate the transition QR-VB. Consequently, two photons can be absorbed creating an electron hole pair, generating two-photon photocurrent and therefore recovering V_{OC}. Measurements were performed at the Instituto de Energia Solar at Universidad Politecnica de Madrid (Spain) under the supervision of Dr. P.G. Linares as described in the *Experimental Techniques* chapter section 4.10. By applying to the diode equation, eq. 2.40 in section 2.4.2, open-circuit condition ($J=0$) we obtain:

$$J_L = J_{01}\left[\exp\left(\frac{qV_{OC}}{n_1 kT}\right) - 1\right] + J_{02}\left[\exp\left(\frac{qV_{OC}}{n_2 kT}\right) - 1\right] + \frac{V_{OC}}{r_p} \quad (6.7)$$

where J_{01} and J_{02} are the saturation reverse current or dark current, q the electron charge, kT the thermal energy in eV, n_1 and n_2 the ideality factors, and r_p the parallel resistance. Eq. 6.7 shows that J_L-V_{OC} curve does not depend on series resistance, which can be typically high in QD/QR based devices. The first of the two exponential terms dominates at low voltage, and the second one at high voltage. The dominant recombination mechanisms can be obtained by calculating the ideality factor from the slope of the linear plot V_{OC} vs log (concentration), or by directly fitting a J_L-V_{OC} curve to the diode equation. The parallel resistance is considered high enough, with values ~10^9 **Ω** in the QRSCs under study, therefore the third term is neglected. By substituting J_L for J and V_{OC} for V, eq. 6.7 becomes equivalent to the dark *J-V* without series resistance. Figure 6.4(a) shows the experimental J_L-V_{OC} curve, measured at room temperature in the concentration range of 0,01 to 4000 suns. The dark *J-V* curve is also shown for comparison. Both overlap at low voltage where the series resistance effect is negligible. Figure 6.4(b) shows V_{OC} dependence with concentration (log scale), the ideality factor (n) is obtained from the slope of the linear fit using eq. 6.7.

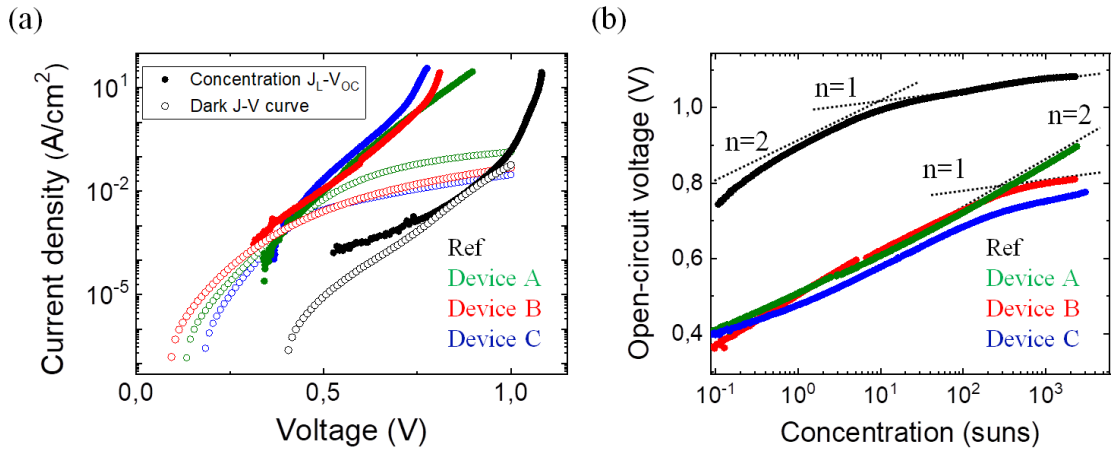

Figure 6.4. The four solar cells measured are: reference-XDM518 (black), device A-XDM563 (10x, 40nm) (green), device B-XDM557 (40x, 10nm) (red) and device C-XDM571 (10x, 6nm) (blue). (a) Illumination current density (J_L) vs open-circuit voltage (V_{OC}) (solid dots), measured under different concentration, and dark current density (J) – voltage (V) curve (open dots) plotted are analogous at low concentration, where the effect of series resistance is negligible- y axis is in logarithmic scale. (b) Open-circuit voltage vs concentration in logarithmic scale. Ideality factor (dotted lines) changes from n equals 2 to 1 at different concentration for each solar cell. In device C, n is 2 for the measured range (0,01-4000 suns).

Table 6.2 summarises the values obtained from the linear fits. All the devices present an ideality factor of 2 at low concentration. As the concentration increases, *n* turns to 1 in the reference cell at 4 suns and in the high QR stack density QRSC [device B-XDM557 (40x, 10nm) and device C-XDM571 (10x, 6nm)] at 150 suns. However, the low QR stack density QRSC [device A-XDM563 (10x, 40nm)] gives *n*=2 until 4000 suns. The diode ideality factor represents current transport mechanisms – a value of *n*=1 indicates diffusion current (which can be correlated with radiative recombination), while *n*=2 indicates generation-recombination current originating via SRH traps. Figure 6.5(a) summarises the values of *n* for high and low QR stack density QRSCs for the experimental data (maximum of 4000 suns), and for the simulated data up to 3 million suns. Figure 6.5(b) represents the different recombination taking place in high QR stack density QRSC as the concentration increases. Firstly, SRH traps in the GaAs bulk dominates. Extra traps are created when growing GaSb QR layers, consequently in QRSCs SRH is expected to dominate over a larger concentration range. Secondly, if the

QR stack density is high enough, the radiative recombination process overtakes (band-to-band transitions attributed to QR-CB, CB-VB could also be presented).

Table 6.2. Ideality factor (*n*) for reference, device A, device B and device C. *n* is obtained from J_L-V_{OC} plot under different concentration ranges (0,01-4 suns, 4-150 suns and 150-4000 suns). The dominant recombination process is also shown.

Concentration range (suns)	**0,01 - 4**	**4 - 150**	**150 - 4000**
Reference XDM518	n=2 **SRH**	n=1 **Radiative**	
Device A XDM563 (10x, 40nm)	n=2 **SRH**		
Device B XDM557 (40x, 10nm)	n=2 **SRH**		n=1 **Radiative**
Device C XDM571 (10x, 6nm)	n=2 **SRH**		n=1 **Radiative**

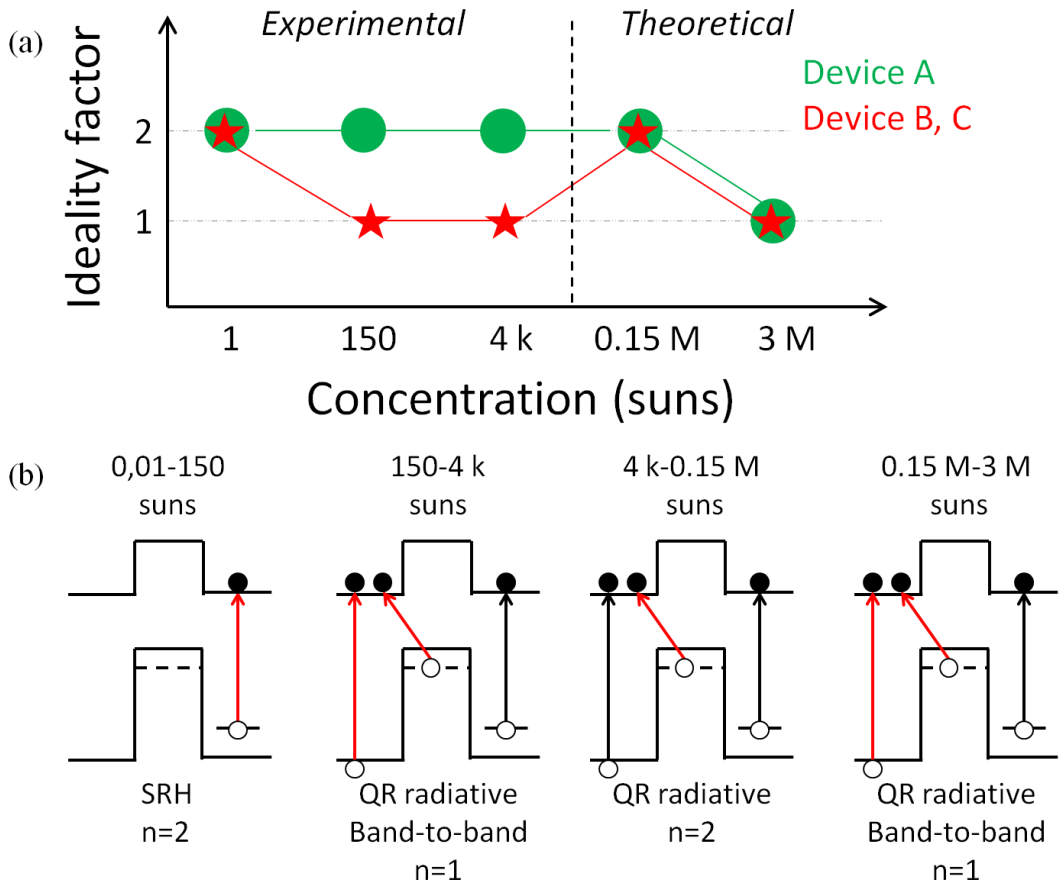

Figure 6.5. (a) Ideality factor as a function of concentration, for low QR stack density QRSC, device A-XDM563 (10x, 40nm) (green circle) and high QR stack density QRSCs, device B-XDM557 (40x, 10nm) and device C-XDM571 (10x, 6nm) (red star). (b) Sketch of recombination processes for high QR stack density QRSCs under concentration. At low concentration (0,01 to 150 suns), SRH (n=2) via traps is dominant. As the concentration increases (150 to 4k suns) radiative recombination from QR and band-to-band (n=1) becomes dominant. According to the mathematical model, at ultra-high concentration recombination will be dominated by QR radiative processes with n equals 2, and finally will tend towards 1 with band-to-band recombination.

By applying the previous kinematic equations [119] to high light concentration experiments we obtain:

$$\frac{\partial \Delta n}{\partial t} = \alpha \phi_C - \frac{\Delta n}{\tau_{eff}} - B_Q N \Delta n \tag{6.8}$$

$$\frac{\partial \Delta p}{\partial t} = \alpha \phi_C - \frac{\Delta p}{\tau_{eff}} + (e_{th} + e_T)N - C_h(N_0 - N)\Delta p \tag{6.9}$$

$$\frac{\partial \mathrm{N}}{\partial t} = C_h(N_0 - N)\Delta p - (e_{th} + e_T)N - B_Q N \Delta n \tag{6.10}$$

where Δn and Δp are the excess electron and hole concentrations, N the QR hole occupation density, α the absorption coefficient, ϕ_C the illumination flux, B_Q the QR recombination coefficient, $\tau_{eff}^{-1} = \tau_{BB}^{-1} + \tau_{SRH}^{-1}$, e_{th} and e_T the non-radiative rates for thermionic emission and tunneling, C_h the hole capture coefficient, and $N_0 = N_{QR}/w$ is density of QR hole states where N_{QR}= (surface state density)*x*(number of layers), and w is the width of space-charge region.

The chemical potential, μ given by $\mu = \mu_e + \mu_h = qV_{OC}$ (6.11), is determined from $pn/n_i^2 = \exp(\mu/KT)$ (6.12). By substituting the values of *n* and *p* derived from eq. 6.8 - 6.10 combined with eq. 6.11 and 6.12, the final expression for V_{OC} as a function of ϕ_C is obtained. Two cases can be considered, **Case I** in which the Fermi level is determined solely by VB hole occupancy, and **Case II** where the Fermi level also depends on QR hole occupancy. As shown in Figure 6.6(a) and (b) for high and low QR stack density QRSC, respectively, Case II fits the experimental data, revealing that the QR energy level and VB are not independent, showing that QR hole occupancy is crucial in type-II GaSb/GaAs QRSC and needs to be controlled. By fitting to experimental data, the QR stack density is identified to be the main parameter responsible for the change towards 1 in the ideality factor. The simulation is used to obtain the behaviour under ultra-high concentration (not possible experimentally), and as shown in the second part of Figure 6.6(a), both types of QRSCs approach n=2, which is identified with QR radiative recombination. For concentration higher than 0.15

Msuns, both tend toward 1 (band-to band transitions) recovering fully V_{OC} of the reference cell.

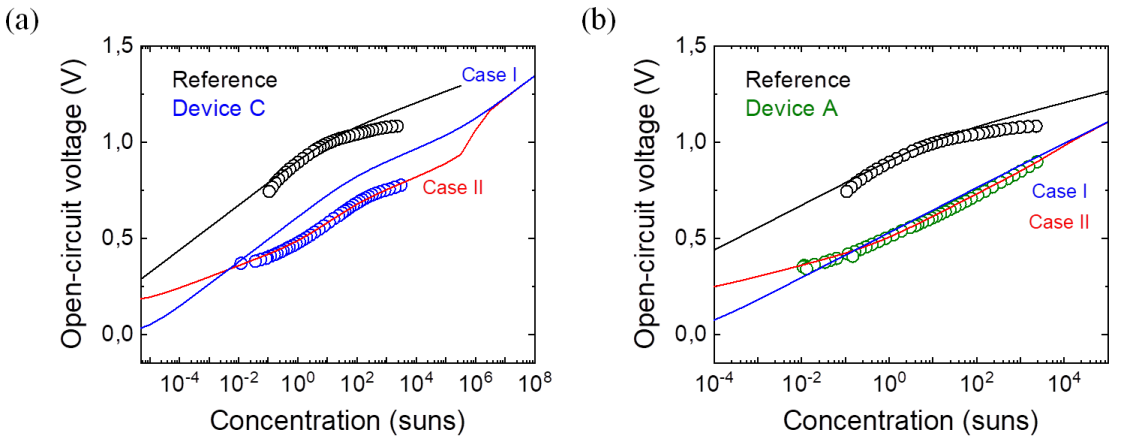

Figure 6.6. Open-circuit voltage vs concentration, comparing experimental (open dots) and simulation (lines) results. According to the model, QRSC are simulated using Case I (blue line), where Fermi level is determined solely by VB occupancy; and Case II (red line), where Fermi level determined by VB and QR occupancy. Reference cell is also simulated (black line). (a) Reference (black open dots) and device C-XDM571 (10x, 6nm) (blue open dots) are shown. Theoretical simulation fits experimental data for reference, and device C using Case II. Device B-XDM557 (40x, 10nm) is not shown as it follows the same trend with concentration as device C. (b) Reference (black open dots) and device A-XDM563 (10x, 40nm) (green open dots) are shown. For low QR stack density there is almost no difference between Case I and II, however at low concentration Case II fits the experimental data better.

From previous studies in type-II GaSb/GaAs IBSC [20], optical generation was expected to overcome thermionic emission under an illumination of 1000 suns. However, we found that the process is more complex than a balance between thermal and optical processes. From the fitting of the simulation to the experimental data, the QR states concentration in low QR stack QRSC (device A) is found to be a factor 30 lower than in high QR stack density (device B and C) and, there is almost no change in SRH lifetime from device A to B (C), with values of 3 to 5 ns respectively. The reason for SRH dominating in device A, is the lower QR radiative contribution, rather than poor quality material.

In conclusion, experimentally it is not possible to fully recover V_{OC} at room temperature even under 4000 suns. The voltage is still limited by the absorption threshold QR-CB ($V_{OC} \leq (E_{CB}-E_{QR})/e$) as shown in the literature, but a partial recovery is observed as the concentration increases. The low density device has a V_{OC} of 0.51 V under 1 sun, which

increased up to 0.91 V at 4000 suns, where the V_{OC} of the reference device is 1.09 V, meaning a recovery of 56% for this device. The high density devices show lower V_{OC} recovery of 27%, reaching a maximum V_{OC} of 0.79 V under 4000 suns. This result shows that because of the fast thermionic emission rate at 300 K, a flux of 4000 suns is not high enough to separate the quasi-Fermi levels sufficiently to recover V_{OC}. Consequently, IB behaviour can only be observed at low temperature. The simulation shows full V_{OC} recovery for QRSC at ultra-high concentration not possible due to thermal limitations (46500 suns is the maximum concentration). This study illustrates the recombination processes in QR under ultra-high flux illumination.

6.3 Electroluminescence (EL)

In this chapter, radiative and non-radiative recombination in type-II GaSb/GaAs QRSC is obtained from electroluminescence (EL) measurements and compared with high light concentration results, highlighting the importance of reducing radiative recombination for avoiding V_{OC} drop. Measurements and analysis were performed at Nelson Mandela University (South Africa) in collaboration with Prof. Magnus C. Wagener. In section 6.3.1, time-resolved photoluminescence is included showing QR recombination rates crucial to understand the limiting processes in type-II GaSb/Gas QRSC.

Following on from the paper in Rau´s paper [125], the radiative open-circuit voltage has a limiting value described by:

$$V_{OC}^{rad} = \frac{KT}{q} \ln \frac{Jsc}{J_{em,0}} \tag{6.11}$$

where Jsc is the short-circuit current under illumination and $J_{em,0}$ short-circuit current in dark conditions. The EQE of the solar cell electroluminescence is defined as:

$$EQE_{LED} = \frac{J_{em}}{J_{inj}} \tag{6.12}$$

where J_{em} is the radiative flux emitted and J_{inj} the injection current.

Grouping together the radiative and non-radiative contributions to V_{OC} we have:

$$V_{OC} = \frac{KT}{q}\left(\ln\frac{J_{SC}}{J_{em,0}} + \ln(EQE_{LED})\right) \quad (6.13)$$

where $EQE_{LED} \leq 1$. If all injected carriers recombine radiatively, then $EQE_{LED} = 1$, and V_{OC} is in the radiative limit. Assuming that EQE_{LED} has some other injection dependence $EQE_{LED}\alpha\left(J_{inj}\right)^{p}$,and considering that Jsc depends linearly on the illumination concentration (ϕ), we have:

$$V_{OC}\,\alpha\frac{KT}{q}\left(\ln\phi + \ln\left(J_{inj}\right)^{p}\right) \rightarrow\ V_{OC}\,\alpha\frac{KT}{q}\ln(\phi)^{1+p}\ \ ,if\ J_{inj} \equiv \phi \quad (6.14)$$

Then, in the case of carriers injected by a high illumination concentration we have:

$$V_{OC}\,\alpha\,(1+p)\frac{KT}{q}\ln\phi \quad (6.15)$$

A similar expression is obtained from the diode equation, considering *1 + p* equals the ideality factor (*n*). When EQE_{LED} is 1 (p = 0, n = 1), and V_{OC} depends linearly on concentration. When EQE_{LED} depends linearly on the injection current, V_{OC} has a supra-linear dependence on concentration. Figure 6.7 shows the analysis of the QR peak electroluminescence, identified around 1.2 μm for the different devices studied: device A-XDM563 (10x, 40nm), device B-XDM557 (40x, 10nm) and device C-XDM571 (10x, 6nm). *m* is the slope between $\ln(J_{em})$ and $\ln(J_{inj})$, following the previous discussion $p = m - 1$, and therefore $n = m$, meaning that the ideality factor (*n*) obtained from V_{OC} vs concentration (ϕ) is equivalent to *m*, slope of the electroluminescence intensity and injection current for the QR peak.

Electroluminescence was measured at low temperature and the injection current was changed from 0.2 to 100 mA. The QR peak blueshifts by increasing injected carriers as expected from band-bending and capacitive charging [83]. The maximum intensity of the QR peak is proportional to J_{em}. Figure 6.7(a) shows the behaviour of the low density QR stack QRSC [device A-XDM563 (10x, 40nm)] measured at 30 K. The slope is larger than 3, showing that non-radiative recombination is dominant for holes in the

QR, where SRH contributes (and probably also defects in the mesa perimeter) [126] explaining the large value. Instead, device B-XDM557 (40x, 10nm) measured at 19 K shows a slope of 0.96, revealing that at low temperature radiative recombination dominates in Figure 6.7(b). Figure 6.7(c) shows the dependence for device C-XDM571 (10x, 6nm) at 40 K, where there is a transition from supra-linear behaviour to linear between 4 - 10 mA. At low concentration/injection current, non-radiative centres like SRH traps contribute to QR recombination. And, at high concentration/injection current radiative processes overtakes. This transition is also observed under high illumination flux, around 150 suns for both high QR stack density QRSCs, devices B and C. For completeness, in Figure 6.7(d) the corresponding EL spectra of device C is shown, where the GaAs peak is identified at 0.85 µm, the WL at 0.95 µm and QR at 1.2 µm.

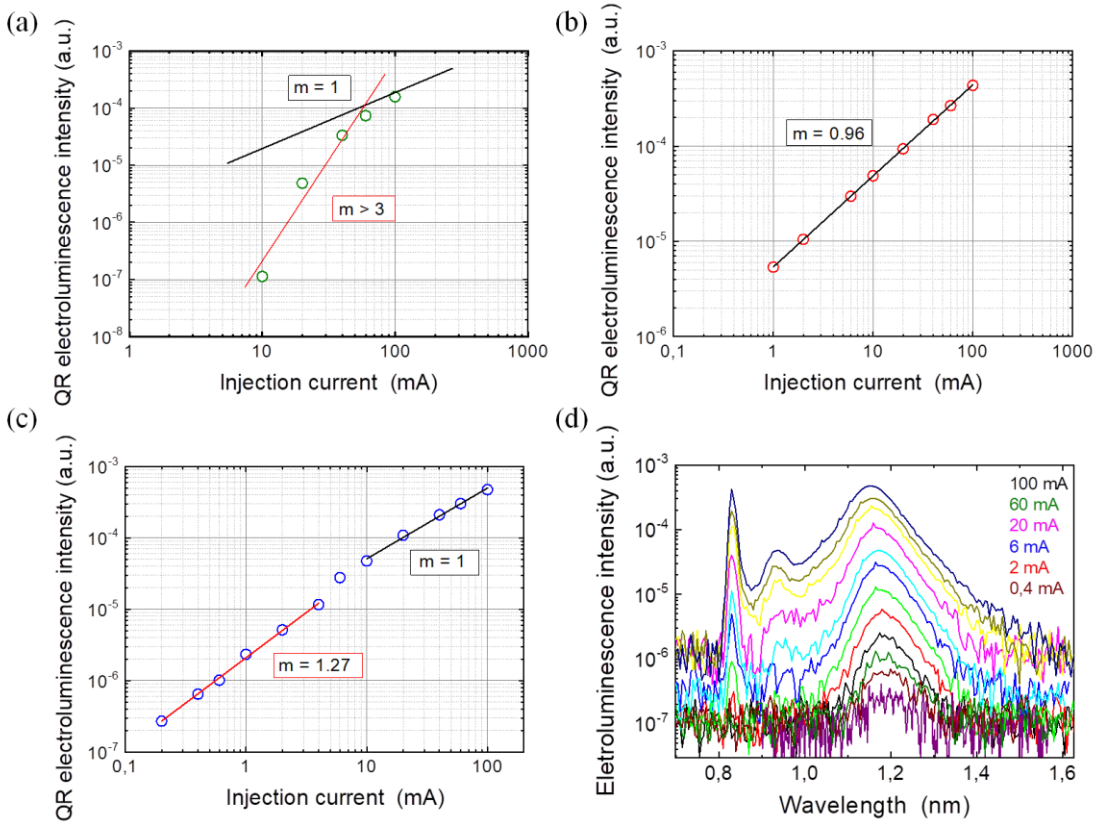

Figure 6.7. Electroluminescence intensity for QR peak at 1.2 µm vs the injection current, measured between 19 and 40 K. (a) Device A-XDM563 (10x, 40nm) (green open dots) measured at 30 K, has a slope (*m*) larger than 3. (b) Device B-XDM557 (40x, 10nm) (red open dots) measured at 19 K, has a slope of *m*=0.96. (c). Device C-XDM571 (10x, 6nm) (red open dots) measured at 40 K, presents a transition between supra-linear behaviour (*m*=1.27) and linear (*m*=1).

For the sake of comparison and for demonstrating the applicability of the electroluminescence-concentration theorem in type-II GaSb/GaAs SC, the slope values obtained under concentrated light and by injecting carriers are summarised in table 6.3 for the different QRSCs. There is definitely a correspondence between the two characterization techniques, for the high QR stack density devices (device B & C) it is clear that radiative recombination dominates under high carrier population (injected or photogenerated). The opposite can be said for the low QR stack density device (device A). For device A, it is clear that SRH dominates from the concentration characterization, however the agreement with the electroluminescence results is not as clear. The disagreement can come from the EL spectra itself (not shown), where QR peak is almost as intense as the deep centre levels and the peak cannot be completely deconvoluted from them. From EL we measure directly the QR – CB transition and its limiting recombination mechanisms. However, from J_L-V_{OC} curve we measure the total photocurrent generated in the base, emitter and i-region (where the QR stack is placed). As stated in the literature review, adding nanostructures in the device strongly limits V_{OC} due to the increased recombination, so we can assume that the recombination from the sub-bandgap transition QR - CB dominates recombination within the device. This equivalence is a powerful tool when characterizing solar cells, as concentration measurements require a more complex set up than electroluminescence.

Table 6.3. Slope between electroluminescence intensity vs injection current (*m*) and ideality factor (*n*) from J_L-V_{OC} under light concentration. *m* and *n* are shown for the different regimes: low and high injection current, and low and high light concentration.

Characterization technique	**Electroluminescence**			**Light concentration**	
Temperature	20 - 40 K			300 K	
Range	Low injection current (J_{inj} < 5 mA)	High injection current (5 mA < J_{inj})		Low concentration (Con < 150 suns)	High concentration (150 suns < Con)
Device A XDM563 (10x, 40nm)	m=3 **SRH + defects**			n=2 **SRH**	
Device B XDM557 (40x, 40nm)	m=1 **Radiative**			n=2 **SRH**	n=1 **Radiative**
Device C XDM571 (10x, 6nm)	m=1.3 **SRH + radiative**		m=1 **Radiative**	n=2 **SRH**	n=1 **Radiative**

6.3.1 Time-Resolved Photoluminescence (TR-PL)

The results described in this sub-section were presented in the paper *'Carrier dynamics of type-II GaSb/GaAs quantum rings for solar cells' at SPIE Photonics West 2018, San Francisco, USA.* Measurements and analysis were performed at Tyndall National Institute (Ireland) in collaboration with Shumithira Gandan. The photoluminescence samples characterized in this section are summarised in table 4.2: 40nm-PJC645 (10x,40nm), 10nm-QDM672 (20x,10nm) and 6nm-QDM693 (20x,6nm). Time-resolved photoluminescence allow us to identify the radiative and non-radiative recombination rates in GaSb/GaAs QR stacks by measuring the decay time of the photoluminescence intensity after a pulsed light beam.

Figure 6.8(a) shows the photoluminescence (PL) spectra measured at 10 K for the samples with spacing 6 and 10 nm. The measurements were performed using a 770 nm laser with 2.5 mW power. Three peaks are identified, corresponding to wetting layer (WL), clusters and quantum ring (QR). QR peak blueshifts for the low spacing sample, the wavelength of the transition increases ~20 nm when decreasing the spacing from 10 to 6 nm. Figure 6.8(b) shows time-resolved photoluminescence (TR-PL) measured at 10 K for QR peak (λ ~1100-1300 nm) for both samples, with 6 and 10 nm spacing. TR-PL were performed using a 780 nm pulsed laser with a frequency of 3 MHz and a power of 0.6 mW, equivalent to a flux of 10^{17} $cm^{-2}s^{-1}$. Radiative (τ_{rad}) and non-radiative (τ_{nr}) decay times (emission rates) are obtained from the exponential fit to the experimental data, the vertical line in Figure 6.8 (b) shows the start of the double exponential fit. The values obtained for carrier lifetime and emission rate are summarized in table 6.4. For 6 and 10 nm spacing the values are τ_{rad} is 11-12 ns (~10^8 s^{-1}) for both samples and τ_{nr} is 97 and 66 ns (~10^7 s^{-1}), respectively. The non-radiative lifetime enhancement for low spacing sample can be due to a larger transition energy, as reported by Y.D. Jang [127], Tyndall is still looking at other possible explanations. Table 6.4 summarises τ_{rad} and τ_{nr}

for the three samples studied (plot is not shown for large spacing sample (10x, 40nm).

The average *radiative recombination rate (QR-CB) for the different samples is ~10^8 s^{-1}*.

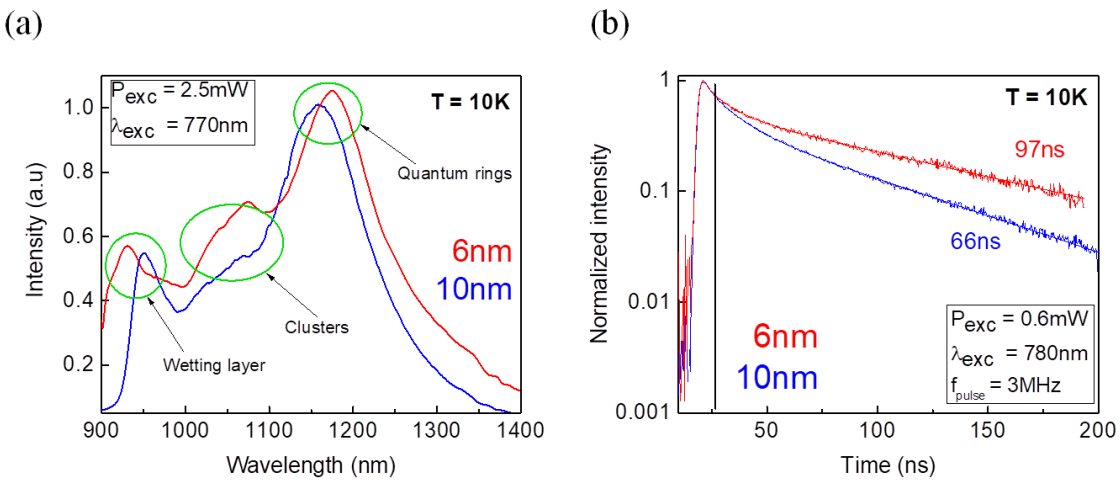

Figure 6.8. (a) Photoluminescence (PL) measured at 10 K, with an excitation power of 2.5 mW with a 770 nm laser. 6 and 10 nm spacing samples (with 20 QR layers) in red and blue, respectively, show three peaks: wetting layer (WL), clusters, and quantum rings (QR). For 6 nm there is slight blueshift of QR peak of ~20 nm, together with a redshift for WL. (b) Time-resolved PL for QR peak (1.1 – 1.3 µm) for 6 (red) and 10 nm (blue) spacing, with a non-radiative decay time of 97 and 66 ns, respectively.

Table 6.4. Radiative and non-radiative recombination (between holes in QR energy levels and electrons in CB) lifetime and emission rates for photoluminescence samples summarized in table 4.2: 40nm-PJC645 (10x,40nm), 10nm-QDM672 (20x,10nm) and 6nm-QDM693 (20x,6nm).

Sample	*Radiative recombination*		*Non-radiative recombination*	
	Lifetime (ns)	*Emission rate (s^{-1})*	*Lifetime (ns)*	*Emission rate (s^{-1})*
40nm-PJC645 *(10x,40nm)*	16	$6x10^7$	85	$1x10^7$
10nm-QDM672 *(20x,10nm)*	12	$8x10^7$	66	$2x10^7$
6nm-QDM693 *(20x,6nm)*	11	$9x10^7$	97	$1x10^7$

6.4 Hydrostatic Pressure

The results described in this section are published in *"Open circuit voltage increase of GaSb/GaAs quantum ring solar cells under high hydrostatic pressure", Solar Energy Materials and Solar Cells, 187 (2018).* Measurements were performed at the Advanced

Technology Centre at Surrey University under the supervision of Dr. Igor P. Marko as described in *Experimental Techniques* chapter in section 4.11.

The devices characterized in this section are summarised in table 4.4, a low QR stack density QRSC-A0503 (10x, 40nm) and reference GaAs SC-A0502. The two solar cells are compared to understand the effect of pressure on the band structure and on recombination within the device. Figure 6.9(a) shows the energy shift for each transition (GaAs bulk, WL and QR) in the QRSC as the hydrostatic pressure is increased from 0 to 8 kbar. From the linear fit of the data plotted in Figure 6.9(b) the pressure coefficient (*PC*) is identified to be ~10.5 ± 0.5 meV/kbar for each transition. This value corresponds to GaAs bulk [128], indicating that the GaAs CB dominates the energy shift under pressure in the different transitions taking place in the QRSC. Figure 6.9(c) sketches the band diagram under 0 kbar and 8 kbar of applied hydrostatic pressure. In a semiconductor under hydrostatic pressure, the CB shift upwards and VB downwards with increasing pressure. The induced shift in the CB under certain range of pressure (ΔP), depends on the deformation potentials (a_C, a_V) of the material, and is given by

$$\Delta E_C = \Delta P \frac{a_C}{a_C + a_V} PC \tag{6.16}$$

where the valence band shift is obtained using a similar expression, substituting a_C for a_V [129]. Using the experimental PC and the tabulated values for a_C and a_V in GaAs, we obtain ΔE_C~72 meV and ΔE_V~12 meV, indicating a total increase of 84 meV under the maximum applied pressure of 8 kbar. In GaSb/GaAs QRSC, the conduction band offset increases 30 meV and a negligible effect is found in the valence band offset and QR confinement energy, so that we expect no change in thermionic emission of holes from QR to VB under illumination at 300 K. Following the dependence of intrinsic carrier density (n_i) with the bandgap, $n_i \propto \exp(-E_G/2KT)$, we expect a decrease in dark current and an increase in open-circuit voltage with pressure.

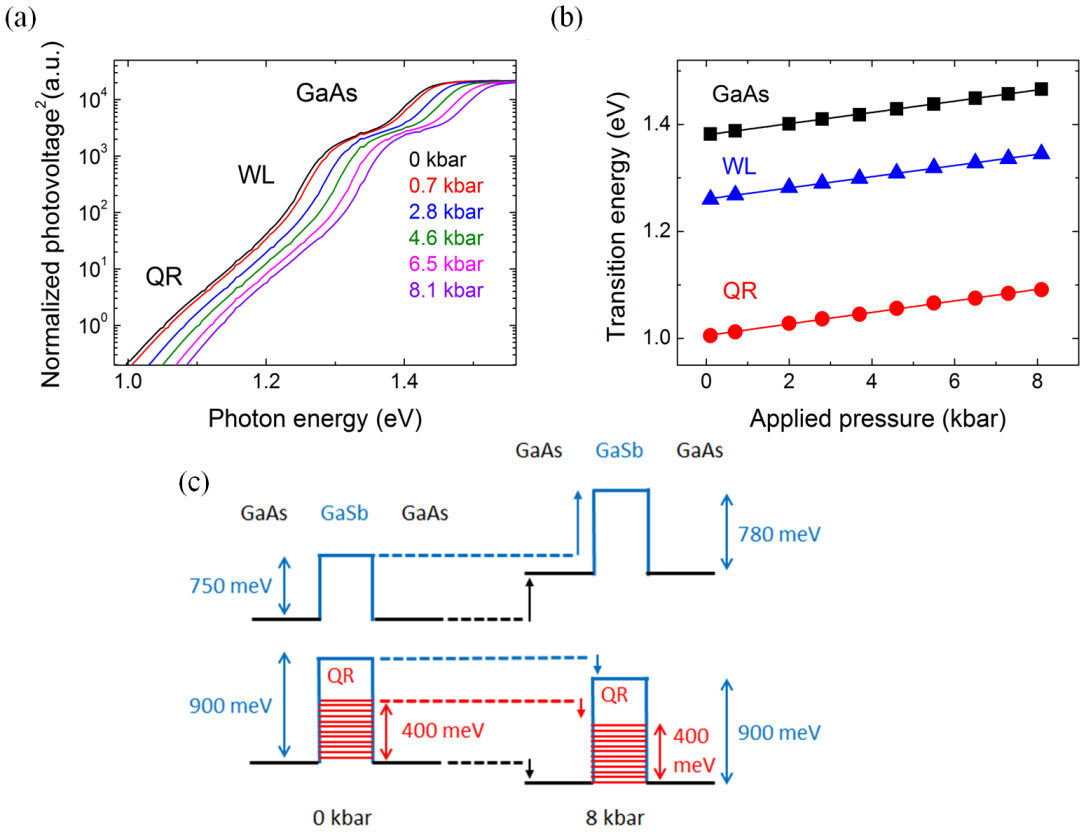

Figure 6.9. (a) Square of the normalized photovoltage versus incident photon energy for the GaSb/GaAs QRSC for different applied pressures measured at 300 K. Three absorption features can be identified corresponding to: GaAs bulk layer, GaSb wetting layer (WL) and GaSb quantum ring (QR). (b) Transition energy versus applied pressure for the GaAs bulk layer (black squares), GaSb WL (blue triangles) and QR (red circles). The pressure coefficients are obtained from the linear fits (solid lines). (c) A schematic energy band diagram for GaSb/GaAs QR at 300 K under 0 and 8 kbar of hydrostatic pressure. Wetting layer energy levels are not shown for simplicity.

Figure 6.10 shows the pressure data from our study - using a QH lamp (~0.01 sun) - and the temperature data from a previous paper of our group [95] - using a lens to concentrate the light up to 19 suns - . From *J-V* curve in Figure 6.10(a), V_{OC} vs pressure is obtained for the QRSC and it is compared with the GaAs SC dependence, as shown in Figure 6.10(b). For QRSC, V_{OC} increases 15 % under 8 kbar, at a rate of 8.5 ± 0.5 mV/kbar. The GaAs SC has a rate of 9.5 ± 0.5 mV/kbar, and V_{OC} is increased by 9 %. In both cases, the V_{OC} rate is lower than *PC* (bandgap change with pressure). In Figure 6.10(c) and (d), temperature and pressure effect are compared for QRSC and GaAs SC. By decreasing temperature down to 90 K and by increasing pressure up to 8 kbar, the bandgap is increased by approximately 100 meV (~4 KT). By using pressure we can

isolate the bandgap change from carrier thermal energy and phonon population. The experimental results show that reducing temperature has the strongest influence and is more effective at increasing V_{OC} in the QRSC than in the GaAs SC. Table 6.5 summarises the V_{OC} relative increase (ΔV_{OC}) for both devices.

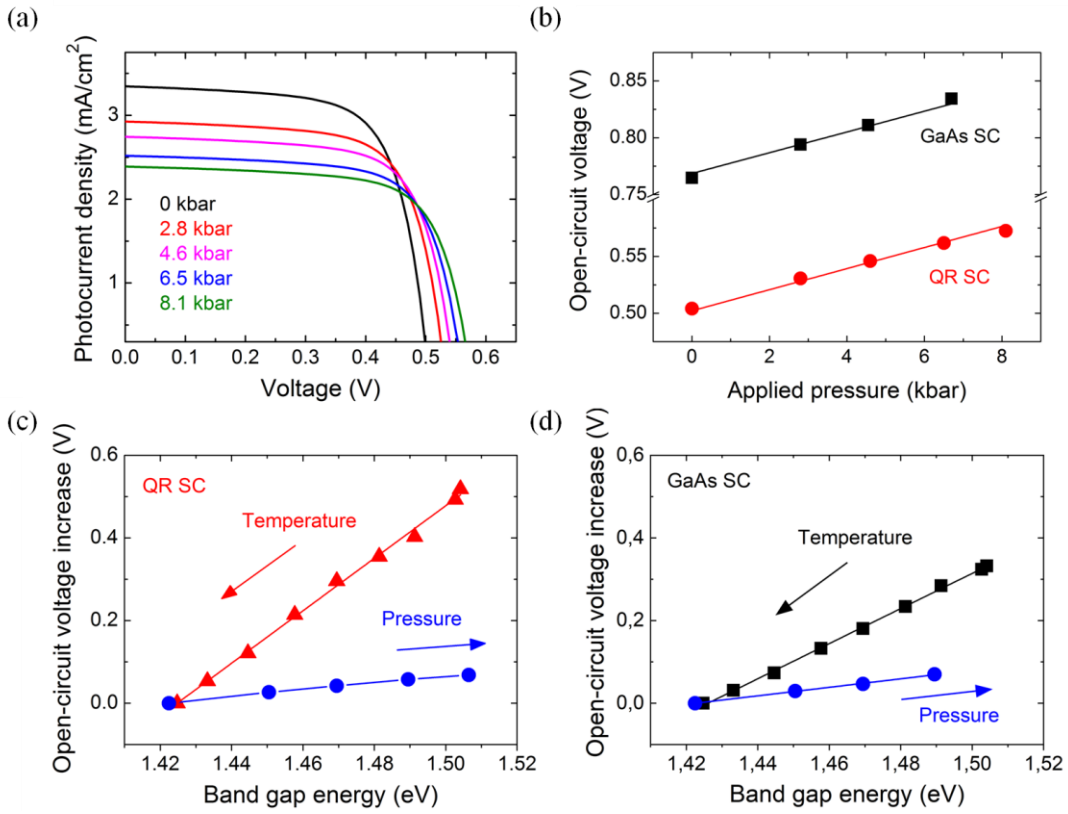

Figure 6.10. (a) *J-V* characteristics of the QRSC under QH lamp illumination as the hydrostatic pressure increases up to 8 kbar. (b) Open-circuit voltage versus pressure for the two cells. (c) The open-circuit voltage increase of the GaAs reference cell; dependence on temperature (black squares) and pressure (blue circles). (d) The corresponding changes in open-circuit voltage for the QR SC with temperature (red triangles) and pressure (blue circles).

Table 6.5. Open-circuit voltage relative increase as hydrostatic pressure increases (from 0 to 8 kbar) and as temperature decreases (from 300 to 90 K) for QR SC-A0503 (10x,40nm) and GaAs SC-A0502.

Devices	*Increasing Pressure* *(ΔP=0-8 kbar)*	*Decreasing Temperature* *(ΔT=300-90 K)*
QR SC-A0503 *(10x,40nm)*	ΔV_{OC} = 15 %	ΔV_{OC} = 80 %
GaAs SC-A0502	ΔV_{OC} = 9 %	ΔV_{OC} = 40 %

In summary, by reducing n_i the recombination through confined holes within the GaSb quantum rings reduces, resulting in an increase of V_{OC} by 15% under 8 kbar and a recovery of 80% at 90 K.

6.5 Summary

Table 6.6 summarises the rates for each process involved in QR hole dynamics, sketched in Figure 6.1: hole trapping (1), radiative recombination (2), hole thermionic emission (3) and hole optical generation (4). As pointed at the beginning of the chapter 6, process (4) must dominate over (3) and (2) while (1) must be similar to (4). In this ideal situation (1) photofills QR energy levels with holes and (4) pumps holes optically to VB generating TPPC. However, as shown in table 6.6 QR hole dynamics in type-II GaSb/GaAs QRSC is far from the ideal situation. The results from two photon photocurrent and time-resolved photoluminescence show that our system is strongly limited by radiative recombination as its rate is few orders of magnitude higher than the rates for the other processes. The high thermionic emission rate compared with optical generation explains the excessive high light concentration needed for achieving V_{OC} recovery (from the mathematical model). V_{OC} recovery ultimately requires: a low QR hole trapping rate; fast optical emission of holes from QR to VB; slow optical QR recombination.

Table 6.6. Rates for the 4 processes involved in hole QR dynamic: (1) hole trapping, (2) radiative recombination, (3) hole thermionic emission, and (4) hole optical absorption. Characterization technique used for obtaining each rate are specified together with the section (and Figure) were the value was derived.

Section	*Figure*	*Characterization technique*	*Process*	*Rates (s^{-1})*	
				Low temperature	*Room temperature*
6.1	Fig.6.2(a)	TPPC	1	10^4	10^9
6.3.1	Fig. 6.8	TR-PL	2	10^8	-
6.1	Fig.6.3	TPPC	3	10^0	10^4
6.1	Fig.6.2(b)	TPCC	4	10^4	10^0

Non-radiative recombination limits device performance in low QR stack density SC and radiative recombination in high QR stack density SC. High light concentration measurements and luminescence reveals how *Voc* is limited by radiative recombination instead of non-radiative recombination.

Hydrostatic pressure is for first time applied to IBSC, showing that thermal carrier and phonon population has a stronger effect on recombination than widening the bandgap, and highlights the importance of reducing recombination in type-II GaSb/GaAs QRSC.

Chapter 7

Summary and conclusions

This thesis focused on the IBSC approach, pursuing high conversion efficiency in solar cells. The specific aim of this research was the study of type-II GaSb/GaAs QRSC working as an IBSC, to understand the potential and the main limitations of the system. Type-II GaSb/GaAs QRSCs were developed at Lancaster University. MBE growth, material characterization, device fabrication in Cleanroom, and solar cell characterization was all done in house. Specific characterization techniques were carried out in collaboration with different research centres and universities: Nelson Mandela Metropolitan University (South Africa), Universidad Politecnica de Madrid (Spain), University of Surrey (United Kingdom) and Tyndall National Institute (Ireland). In this thesis, the effect of modifying the QR stack growth parameters is studied for first time in type-II QRSC, and the results obtained from the different specific characterization techniques bring deep understanding of carrier dynamics in GaSb/GaAs QR. The main achievements of this work are summarised below.

7.1 Summary of main achievements

- High density stack of type-II GaSb/GaAs QR of high crystalline quality were successfully grown and characterized as QRSC. The stacks consisted of up to 50 QR layers with a linear density of the QR of 0.17 nm^{-1} along the growth direction, which is the highest reported to date for a type-II quantum dot/ring IBSC.
- Enhancement of sub-bandgap light absorption was achieved by adding extra QR layers and increasing the QR stack density. EQE and EL were enhanced by a factor of 4 for WL and QR transitions by increasing the number of QR layers from 10 to 40.

- Hole transport through the intrinsic region of the device was improved for photogenerated holes originating in the base region of the cell. Decreasing the QR stack thickness from 400 to 60 nm resulted in an enhancement of 15% in short-circuit current and 30% in conversion efficiency.
- Two-photon photocurrent was studied in type-II QRSC using two-colour spectroscopy at 17 K. Hole Trapping was identified as the mechanism controlling the QR (hole) charging, and above 100 K hole thermionic emission dominates QR discharging over hole optical emission.
- QR non-radiative and radiative decay times were obtained at 10 K. Values of 10-100 ns, equivalent to rates of 10^{8}-10^{7} s^{-1}, were obtained under a peak flux of 10^{17} $cm^{-2}s^{-1}$.
- Partial V_{OC} recovery under solar concentration was demonstrated in type-II QRSC under 4000 suns at RT. QR state concentration is identified as the main parameter dominating QR recombination, as illumination increases SRH is overtaken by radiative band-to-band recombination.
- Electroluminescence and V_{OC} relation is demonstrated for type-II QRSC. Showing that QR radiative recombination limits V_{OC}.
- Hydrostatic pressure was applied to IBSC for the first time, to characterize type-II GaSb/GaAs QRSC. Under 8 kbar at room temperature, the bandgap increased by 100 meV without modifying the carrier thermal energy. Consequently, V_{OC} improves by 15% in QRSC. V_{OC} recovers but just at low temperature, by minimizing recombination.

7.2 Impact of growth parameters

The epitaxial growth was modified to enhance the optical absorption by increasing the QR stack density. The two approaches carried out were: (i) increasing number of QR layers and (ii) decreasing the spacing between consecutive QR layers. In both cases, the material exhibits high crystalline quality without dislocations propagating through the

structure (TEM images) and uniform GaSb layers (XRD spectra). WL and QR are preserved in high QR stack density, having equivalent size and composition compared to low density samples, without modifying the energy band diagram of type-II GaSb/GaAs QR.

Firstly, *the number of QR layers was increased from 10 up to 40* (inside the intrinsic region) reducing the spacing between the layers from 40 down to 10 nm (with a QR stack thickness of 400 nm for both cases). By adding extra QR layers, the extracted sub-bandgap photocurrent from the device is increased proportionally by a factor 4. The absorption enhancement results in a corresponding EQE increase, from 1.3% up to 4.3% for the WL (λ=0.94 μm), and from 0.04% up to 0.15% for the QR (λ=1.16 μm). However, unfortunately the photocurrent from carriers generated in the base and emitter regions is compromised by recombination, so that the overall short-circuit current is not enhanced. This approach enhances sub-bandgap light absorption increasing emission from WL and QR, but it does not increase the conversion efficiency of the cell.

Secondly, *the spacing between QR layers was reduced from 40 to 6 nm* (10 QR layers in both samples), and therefore QR stack density in the i-region is increased from 0.025 up to 0.17 nm^{-1}. Consequently, the QR stack thickness was decreased from 400 to 60 nm (6.7 times smaller), which increased photogenerated hole diffusion from base to emitter. Furthermore, EQE was enhanced from 30 to 35% for wavelengths 700-900 nm (base region) increasing short-circuit current up to 16 mA/cm^2 - a relative increase of 15%. Decreasing the spacing to 6 nm improves the conversion efficiency to 6%, but this is low compared with the reference device (12%).

In summary, decreasing the QR stack thickness and increasing the number of QR layers improved the sub band gap solar cell performance, however the addition of QRs degrades the overall efficiency contrary to expectations for IBSC.

7.3 Dynamics of QR hole charging and discharging

Type-II GaSb/GaAs QRSCs are characterized under specific characterization techniques to study the IB operation principles (TPPC and V_{OC} conservation). *Two photon illumination* was used to study two photon photocurrent, *high light concentration* measurements were done to analyse open-circuit voltage recovery. *Electroluminescence* spectra were measured to establish the dominant recombination mechanism, while *hydrostatic pressure* was used to isolate bandgap widening effects in respect of the thermal carrier distribution. These measurements reveal different aspects of carrier dynamics, fundamental to understanding of the limiting factors for achieving IB behaviour in our type-II QR system. In the following the main results are summarised.

Two photon photocurrent measurements were performed in Nelson Mandela Metropolitan University (SA), analysed and compared with a mathematical model by Prof. Magnus C. Wagener. The hole capture cross-section and hole optical emission cross-section were determined at low temperature from steady-state and time dependent hole emission measurements at 17 K, with values of $\approx 10^{-13}$ and 10^{-16} cm^2, respectively. The emission rate is temperature dependent; at low temperature the optical emission dominates with a rate of $\approx 10^{0}$ s^{-1} (under a certain light intensity) and as the temperature increases thermionic emission increases exponentially, dominating hole emission above 100 K with a similar rate of $\approx 10^{0}$ s^{-1}. The activation energy for thermionic hole emission was found to be 150 meV. Consequently, QR hole occupancy is determined by the quenching temperature of TPPC, given by non-radiative recombination processes involving hole trapping and thermionic emission.

High light concentration measurements were carried out at the Instituto de Energia Solar of Universidad Politecnica de Madrid (Spain) under the supervision of Dr. Pablo G. Linares. The SCs were characterized under a maximum concentration of 4000 suns at room temperature. In QRSC under high concentration, V_{OC} is expected to recover

towards the reference cell value, and full recovery should be achieved in an ideal IBSC. Under 1 Sun the low QR stack density device exhibits a V_{OC} of 0.51 V, increasing by 78% under 4000 suns, up to 0.91 V. In contrast, the high QR stack density devices show a lower increase of 55%, with a V_{OC} of 0.79 V. The reference cell reaches a maximum of 1.09 V, meaning that the low density device recovers by 56% and the high density device by 27%, at 4000 suns. From J_L-V_{OC} curve characterization, the recombination process mechanisms were identified in each cell. In the low density QRSC, SRH recombination (n=2) dominates through all the illumination range. Instead, in the high density QRSC, the higher QR concentration enhances the radiative band-to band QR recombination, overtaking SRH recombination (n=1) above 4 suns. Following the mathematical discussion developed by Dr. Magnus C. Wagener, under ultra-high solar concentration both types of QRSC should fully recover the reference V_{OC}. The experimental data fits the model according with a hole quasi Fermi level is dictated by QR and VB occupation, and not solely by the VB. Consequently, radiative recombination dominates in high QR density stack solar cells, however V_{OC} is limited by QR occupation and ultra-high illumination levels which are non-achievable experimentally would be needed to obtain full open-circuit voltage recovery.

Electroluminescence measurements were performed in Nelson Mandela Metropolitan University (SA) and analysed by Dr. Magnus C. Wagener. According to the reciprocity relation between EQE and EL emission [125], V_{OC} dependence with light concentration and EL dependence with injection current are equivalent. The recombination mechanisms identified from each method are in agreement, proving EL to be an alternative technique to characterize IBSC. The correspondence between V_{OC} and EL implies that high sub-bandgap EL intensity limits cell voltage. High EL intensity indicates efficient radiative recombination in the SC, and consequently holes recombine before being emitted optically to the VB contributing to the output current and voltage.

From EL measurements the origin of V_{OC} reduction in type-II QRSC was demonstrated, showing that radiative recombination is also a limiting factor for achieving IB behaviour.

Hydrostatic pressure measurements were performed in the Advanced Technology Centre at the Surrey University under the supervision of Igor P. Marko. This technique was applied for first time to the solar cell field and compared with temperature. Under 8 kbar spectral photocurrent, dark and illumination I-V curves were measured out at RT. The pressure coefficient of each transition was identified as 10.5 meV/kbar, and found to be dominated by the pressure dependence of the host GaAs. The bandgap is increased by 100 meV under 8 kbar of pressure and at a temperature of 90 K. By applying pressure the bandgap widens without affecting the carrier thermal distribution, reducing n_i by a factor of 5, resulting in a V_{OC} increase of 15% for the QRSC. However, decreasing temperature has the strongest effect minimizing n_i, and consequently increasing and recovering V_{OC} by 50%. Hydrostatic pressure measurements again highlight the importance of recombination limiting V_{OC} and solar cell performance in type-II QRSC.

In summary, trapping and thermionic emission are the key mechanisms which charge and discharge the QRs at room temperature, limiting solar cell performance. Hole capture enhances recombination through QR limiting V_{OC}, and the fast thermionic emission rate prevents hole escape via optical absorption degrading TPPC.

7.4 Suggestions for further work

In the introduction we addressed the main problems of type-I QDSC and in the literature we reviewed each of them. Some of the problems are solved with type-II approach but other ones still remain, like low J_{SC} and low V_{OC}, without obtaining high conversion efficiency:

i. **Low QR absorption coefficient.** With type-II GaSb/GaAs QRSC sub-bandgap light absorption is enhanced by growing high QR stack density, however J_{SC} and conversion efficiency are not improved. The QR in-plane density could be improved by changing the growth conditions. The shape of the QR is not optimum, the rectangular shape behaves more like a QW and not like a 0D structure. However, from the point of view of the epitaxial growth it is difficult to control size, shape and density in the self-assembly process, and new growth techniques are needed.

ii. **Carrier lifetime.** QR radiative and non-radiative recombination decay times are in the order of 10 to 100 ns, measured at 10 K and using laser power of 0.6 mW, carrier lifetime is highly dependent on power and temperature. For probing an increase in decay time in type-II compared with type-I, both structures must be measured exactly under the same conditions – in the literature review an increase of a factor 2 was observed when comparing properly the two types of structure. Even when type-II enhances carrier lifetime reducing recombination rate, *Voc* is ultimately still limited by radiative recombination, as shown for type-II GaSb/GaAs QRSC. One possibility is to reduce hole trapping by adding barriers of a wider bandgap material like AlGaAs, or by growing the QD/QR directly on a wider host material. There is already some preliminary work reported on this matter - theoretical and experimental [130, 131, 132]. At Lancaster we started some preliminary investigation growing 10 QR layers with a narrow $Al_{0.35}Ga_{0.65}As$ of 2 nm between them, giving successful PL and XRD. Further work needs to be done, modifying Al composition and well thickness, and testing the device as an IBSC, measuring TPPC and V_{OC} recovery.

iii. **Thermal coupling between IB and CB/VB.** The high hole thermionic emission rate can be reduced by increasing hole confinement. Growing QRs in a wider gap matrix or using barriers will benefit the thermionic rate as well. The mathematical model that

simulates QRSC behaviour under solar concentration can be used to predict which structure will be limited solely by VB occupation, without the effect of QR occupancy.

iv. **Recombination.** Non-radiative recombination is overtaken by radiative at high solar concentration, when QR concentration is high enough in the device. GaSb/GaAs QR relieves the strain efficiently, as no defects or dislocations are shown in high density devices, neither an increase in dark current nor an increase in SRH recombination. The high crystal quality of the system prevents non-radiative recombination from degrading QRSC performance. Reducing radiative recombination is the key to increase V_{OC}. It is possible by decreasing the overlap between electron and hole wavefunction, however it will also reduce the absorption coefficient of the QR-CB transition. QR radiative recombination and absorption cannot be modified independently. Hole optical emission rates needs to be faster than radiative recombination (and thermionic emission). This is possible by using different materials, with higher absorption coefficient for the transition IB-VB than CB-IB, in the case of a type-II alignment. And by engineering the bands, like in the case of a quantum rachet [133].

In conclusion, absorption coefficient, and consequently the cross-section of the optical transition needs to be enlarged by using different materials or controlling size, shape and density of the nanostructures. However, the optical rates need to be engineered, hole optical emission rate needs to be faster than hole recombination. And thermionic emission needs to be addressed as well, - it can be reduced by using AlGaAs barrier or host material for isolating QR localised states and achieving three separate Fermi levels.

References

[1] International Energy Agency, International Energy Agency, Paris.

[2] International Energy Agency, "Global energy & CO2 status report 2017," 2018.

[3] M.Pidwirny, "Surface area of our planet covered by oceans and continents," University of British Columbia, Okanagan, 2007.

[4] J.Tester et. al., "MIT Energy Initiative report: The Future of Geothermal Energy," MIT Energy, 2006.

[5] "Global Rural-Urban Mapping Project, Version 1 (GRUMPv1): Urban Extents Grid. Palisades, NY: NASA Socioeconomic Data andApplications Center (SEDAC), Center for International Earth Science Information Network," CIESIN - Columbia University.

[6] M.Perez and R.Perez, *IEA-SHCP-Newsletter,* vol. 62, 2015.

[7] National Renewable Energy Laboratory, 2015. [Online]. Available: https://www.energy.gov/eere/solar/downloads/research-cell-efficiency-records.

[8] W.Shockley, and H.J.Queisser, "Detailed Balance Limit of Efficiency of pn Junction Solar Cells," *J. App. Physics,* vol. 32, no. 510, 1961.

[9] M.A.Green et al, "Solar cell efficiency tables (version 52)," *Prog Photovolt Res Appl.,* vol. 26, p. 427–436, 2018.

[10] *Fraunhofer Institute for Solar Energy Systems ISE,* 2014.

[11] M.A.Green, "Third generation photovoltaics: ultra-high conversion efficiency at low cost," *Prog. Photovoltaics,* vol. 9, no. 123, 2001.

[12] Bloomberg New energy finance, 2015.

[13] G.Conibeer, "Third-generation photovoltaics," *Materials today,* vol. 10, no. 11, 2007.

[14] A.Luque, and V.Andreev, Multijunction Concentrator Solar Cells: An Enabler for Low-Cost Photovoltaic Systems., Springe, 2007.

[15] A.Luque, and A.Marti, "Increasing the efficiency of ideal solar cells by photon induced transition at intermediate levels," *Phys. Rev. Lett.,* vol. 78, no. 26, 1997.

[16] Y.Okada, N.J.Ekins-Daukes, T.Kita, R.Tamaki, M.Yoshida, A.Pusch, O.Hess, C.C.Phillips, D.J.Farrell, K.Yoshida, N.Ahsan, Y.Shoji, T.Sogabe, and J.-F.Guillemoles, "Intermediate band solar cells: Recent progress and future directions," *App. Phy. Rev.,* vol. 2, no. 021302, 2015.

[17] E.Antolin, A.Marti, C.D.Farmer, P.G.Linares, E.Hernandez, A.M.Sanchez, T.Ben, S.I.Molina, C.R.Stanley, and A.Luque, "Reducing carrier escape in the InAs/GaAs quantum dot intermdeicate band solar cell," *J. Appl. Phys.,* vol. 108, pp. 064513-1-064513-7, 2010.

[18] P.G. Linares, A. Marti, E. Antolin, C.D. Farmer, I. Ramiro, C.R. Stanley, and A. Luque, "Voltage recovery in intermediate band solar cells," *Sol. Energ. Mat. & Sol. Cell,* vol. 98,

pp. 240-244, 2012.

[19] L.Cuadra, A.Marti, and A.Luque, "Type II broken band heterostructure quantum dot to obtain a material for the intermediate band solar cell," *Phys. E,* vol. 14, pp. 162-165, 2002.

[20] J.Hwang, A.J.Martin, J.M.Millunchick, and J.D.Phillips, "Thermal emission in type-II GaSb/GaAs quantum dots and prospects," *J. Appl. Phys.,* vol. 111, p. 074514, 2012.

[21] P.J. Carrington, M.C. Wagener, J.R. Botha, A. M. Sanchez, and A. Krier, "Enhanced infra-red photo-response from GaSb/GaAs quantum ring solar cells," *Appl. Phys. Lett.,* vol. 101, no. 231101, 2012.

[22] D.Long, Energy bands in semiconductors, New York: John Wiley and Sons, 1968.

[23] H.Y.Fan, "Temperature Dependence of the Energy Gap in Semiconductors," *Phys. Rev.,* vol. 82, no. 900, 1951.

[24] C.Kittel, "Chap. 7," in *Quantum Theory of Solids*, New York, Wiley, 1963.

[25] Y.P. Varshni, "Temperature dependence of the energy gap in semiconductors," *Physica,* vol. 34, no. 1, pp. 149-154, 1967.

[26] J.W.Matthews, and A.E.Blakeslee, "Defects in epitaxial multiplayers. I. Misfit dislocations," *J. Crystal Growth,* vol. 27, no. 118, 1974.

[27] M.P.C.M.Krijin, "Heterojunction band offsets and effective masses in III-V quaternary alloys," *Semicond.Sci.and Tech.,* vol. 6, no. 1, 1991.

[28] R.A.Smith, Semiconductors, 1978.

[29] S.M.Sze, and K.K.Ng, Physics of semiconductors devices, John Wiley & Sons, 2006.

[30] E.F.Shubert, Light-Emitting Diodes, New York: Cambridge Univerity Press, 2006.

[31] C.E.Webb, and J.D.C.Jones, Handbook of Laser Technology and Applications, Bristol: Institute of Physics, 2004.

[32] W.Shockley, and W.T.Read, " Statistics of the Recombinations of Holes and Electrons," *Phys. Rev.,* vol. 87, pp. 835-842, 1952.

[33] R.J.Young, E.P.Smakman, A.M.Sanchez, P.Hodgson, P.M.Koenraad, and M.Hayne, "Optical observation of single-carrier chargingin type-II quantum ring ensembles," *App. Phys. Lett.,* vol. 100, no. 082104, 2012.

[34] P.D.Hodgson, R.J.Young, M.A.Kamarudin, P.J.Carrington, A.Krier, Q.D.Zhuang, E.P.Smakman, P.M.Koenraad, and M.Hayne, "Blueshifts of the emission energy in type-II quantum dot and quantum ring nanostructure," *J. Appl. Phys.,* vol. 114, no. 073519, 2013.

[35] P.D.Hodgson, The Optical Properties os Self-Assembled Quantum Dots, Rings and Posts, Lancaster: University of Lancaster, 2014.

[36] Z.Szczepaniak, and B.Galwas, Photo-devices for optical controlling of microwave circuits, 2019.

[37] L.C.Hirst and N.J.Ekins-Daukes, "Fundamental losses in solar cells," *Prog. Photovolt: Res. Appl.,* vol. 19, pp. 286-293, 2011.

[38] M.A. Green, Third Generation Photovoltaics: Ultra-High Efficiency at Low Cost, Berlin: Springer-Verlag, 2003.

[39] P.Würfel, "The chemical potential of radiation," *J. Phys. C,* vol. 15, 1982.

[40] A. Brown, Thesis: Ultimate Efficiency Limits of Multiple Energy Threshold Photovoltaic Devices, Sydney: University of New South Wales, 2003.

[41] W.Shockley, and H.J.Queisser, "Detailed Balance Limit of Efficiency of pn Junction Solar Cells," *J. App. Physics,* vol. 32, no. 510, 1961.

[42] M.A.Green, "Third generation photovoltaics: solar cells for 2002 and beyond," *Phys. E,* vol. 14, pp. 65-70, 2002.

[43] T.Takamoto, M.Kaneiwa, M.Imaizumi, and M.Yamaguchi, "InGaP/GaAs-based multijunction solar cells," *Prog. Photovoltaics,* vol. 13, pp. 495-511, 2005.

[44] R.R.King, D.C.Law, K.M.Edmondson, C.M.Fetzer, G.S Kinsey, H.Yoon, R.A.Sherif, and N.H.Karam, "40% efficient metamorphic GaInP⁄GaInAs⁄Ge multijunction solar cells," *Appl. Phys. Lett.,* vol. 90, no. 183516, 2007.

[45] F.Dimroth, M.Grave, P.Beutel et.al., "Wafer bonded four-junction GaInP/GaAs//GaInAsP/GaInAs concentrator solar cells with 44.7% efficiency," *Prog. Photovolt,* vol. 22, p. 277–282, 2014.

[46] A.Luque, and A.Marti, "Limiting efficiency of coupled thermal and photovoltaic converters," *Sol. Energy Maters. Sol. Cells,* vol. 58, no. 2, pp. 147-165, 1999.

[47] W.Shockley, and W.T.Read, "Statistics of the recombination of holes and electrons," *Phys. Rev.,* vol. 87, no. 5, p. 835–842, 1952.

[48] R.N. Hall, "Electron-hole recombination in germanium," *Phys. Rev.,* vol. 87, no. 2, 1952.

[49] A.Luque, A.Marti, E.Antolin, and C.Tablero, "Intermediate bands versus levels in non-radiative recombination," *Physica B,* vol. 382, p. 320–327, 2006.

[50] W.Walukiewicz, W.Shan, K.M.Yu, J.W.Ager, E.E.Haller, I.Miotkowski, M.J.Seong, H.Alawadhi, and A.K.Ramdas, "Interaction of Localized Electronic States with the Conduction Band: Band Anticrossing in II-VI Semiconductor Ternaries," *Phys. Rev. Lett.,* vol. 85, no. 7, p. 1552, 2000.

[51] W.Shan, W.Walukiewicz, J.W.Ager, E.E.Haller, J.F.Geisz, D.J.Friedman, J.M.Olson, and S.R.Kurtz, "Band Anticrossing in GaInNAs Alloys," *Phys. Rev. Lett.,* vol. 82, p. 1221, 1999.

[52] N.Lopez, A.Reichertz, K.M.Yu, K.Campman, and W.Walukiewicz, "Engineering the Electronic Band Structure for Multiband Solar Cells," *Phy. Rev. Lett.,* vol. 106, p. 028701, 2011.

[53] K.Zelazna, R.Kudrawiec, A.Luce, K.-M.Yu, Y.J.Kuang, C.W.Tu, and W.Walukiewicz, "Photoreflectance studies of optical transitions in GaNPAs intermediate band solar cell absorbers," *Sol. Energy Materials and Solar Cells,* vol. 188, pp. 99-104, 2018.

[54] T.Tanaka, K.Saito, Q.Guo, K.-M.Yu, and W.Walukiewicz, "Improved photovoltaic properties of ZnTeO-based intermediate band solar cells," *Proceedings SPIE,* vol. 10527, 2018.

[55] I.Ramiro, A.Marti, E.Antolin, and A.Luque , "Review of Experimetnal Results Related to the Operation of Intermediate Band Solar Cells," *IEEE J. Photovolt.,* vol. 4, no. 2, 2014.

[56] Z.Zheng, H.Ji, P.Yu, and Z.Wang, "Recent Progress Towards Quantum Dot Solar Cells with Enhanced Optical Absorption," *Nanoscale Research Letters,* vol. 11, no. 266, 2016.

[57] A.Luque, A.Marti, and C.Stanley, "Understanding intermediate-band solar cell," *Nat. Phot.,* vol. 5, 2012.

[58] R.Strandberg, and T.Reenaas, "Optimal filling of the intermediate band in idealized intermediate-band solar cells," *IEEE T. Electron Dev.,* vol. 58, p. 2559–2565, 2011.

[59] A.Marti, E.Antolin, E.Canovas, N.Lopez, P.G.Linares, A.Luque, C.R.Stanley, and C.D.Farmer, "Elements of the design and analysis of quantum dot intermediate band solar cells," *Thin Solid Films,* vol. 516, pp. 6716-6722, 2008.

[60] K.Yamaguchi, and T.Kanto, "Self-assembled InAs Quantum Dots on GaSb/GaAs(001) Layers by Molecular Beam Epitaxy," *J. Cryst. Growth,* vol. 275, pp. 2269-2273, 2005.

[61] N.Kakuda, T.Yoshida, and K.Yamaguchi, "Sb-mediated growth of high-density InAs quantum dots and GaAsSb embedding growth by MBE," *Appl. Surf. Sci.,* vol. 254, no. 4, pp. 8050-8053, 2008.

[62] E.Saputra, J.Ohta, N.Kakuda, and K.Yamaguchi, "Self-Formation of In-Plane Ultrahigh-Density InAs Quantum Dots on GaAsSb/GaAs(001)," *Appl. Phys. Express,* vol. 5, no. 125502, 2012.

[63] T.Sugaya, O.Numakami, R.Oshima, S.Furue, H.Komaki, T.Amano, K.Matsubara, Y.Okano, and S.Niki, "Ultra high stacks of InGaAs/GaAs quantum dots for high efficiency solar cells," *Energy Environ. Sci.,* vol. 5, p. 6233–6237, 2012.

[64] S.M.Hubbard, C.D.Cress, C.G.Bailey, R.P.Raffaelle, S.G.Bailey, and D.M.Wilt, "Effect of strain compensation on quantum dot enhanced GaAs solar cells," *App. Phys. Lett.,* vol. 92, p. 123512, 2008.

[65] C.G. Bailey, D.V. Forbes, R.P. Rafaelle and S.M. Hubbard, "Near 1 V open circuit voltage in InAs/GaAs quantum dot solar cell," *Appl. Phys. Lett.,* vol. 98, p. 163105, 2011.

[66] C.G.Bailey, D.V.Forbes, S.J.Polly, Z.S.Bittner, Y.Dai, C.Mackos, R.P.Raffaelle, and S.M.Hubbard, "Open-Circuit Voltage Improvement of InAs/GaAs Quantum Dot Solar Cells Using Reduced InAs Coverage," *IEEE J. Photovolt.,* vol. 2, no. 3, pp. 269-275, 2012.

[67] S.A. Blokhin, A.V.Sakharov, A.M.Nadtochy, A.S.Pauysov, M.V.Maximov, N.N.Ledentsov, A.R.Kovsh, S.S.Milkhrin, V.M.Lantratov, S.A.Mintairov, N.A.Kaluzhniy, and M.Z.Shvarts , "AlGaAs/GaAs photovoltaic cells with an array of InGaAs QDs," *Semiconductors,* vol. 43,

pp. 514-518, 2009.

[68] N.N.Ledentsov, V.A.Shchukin, M.Grundman, N.Kirstaedter, J.Bohrer, O.Schmidt, D.Bimberg, et al, "Direct formation of vertically coupled quantum dots in Stranski-Krastanow growth," *Phy. Rev. B,* vol. 54, no. 12, 1996.

[69] K.A.Sablon, J.W.Little, K.A.Olver, W.ZhM, V.G.Dorogan, Y.I.Mazur, G.J.Salamo, and F.J.Towner, "Effects of AlGaAs energy barriers on InAs/GaAs quantum dot solar cells," *J.Appl.Phys.,* vol. 108, no. 074305, 2010.

[70] A.Marti, E.Antolin, C.R.Stanley, C.D.Farmer, N.Lopez, P.Diaz, E.Canovas, P.G.Linares, and A.Luque, "Production of Photocurrent due to Intermediate-to-Conduction-Band Transitions: A Demonstration of a Key Operating Principle of the Intermediate-Band Solar Cell," *Phys. Rev. B,* vol. 97, no. 247701, 2006.

[71] R.Tamaki, Y.Shoji, Y.Okada, and K.Miyano, "Spectrally resolved intraband transitions on two-step photon absorption in InGaAs/GaAs quantum dot solar cell," *App. Phys. Lett.,* vol. 105, no. 073118, 2014.

[72] I.Ramiro, E.Antolin, P.G.Linares et. al., "Two-photon photocurrent and voltage up-conversion in a quantum dot intermediate band solar cell," *Proceeding of the IEEE 40th Photovolatic Specialist (PVSC),* no. 3251, 2014.

[73] A.Datas, E.Lopez, I.Ramiro, E.Antolin, A.Marti, and A.Luque , "Intermediate Band Solar Cell with extreme broadband Spectrum Quantum Effiiciency," *Phys. Rev. Lett.,* vol. 114, no. 157701, 2015.

[74] A.Scaccabarozzi, S.Adorno, S.Bietti, M.Acciarri, and S.Sanguinetti, "Evidence of two-photon absorption in strain-free quantum dot GaAs/AlGaAs solar cells," *Phys. Status Solidi (RRL),* vol. 7, no. 3, pp. 173-176, 2013.

[75] Y.Okada, T.Morioka, K.Yoshida, R.Oshima, Y.Shoji, T.Inoue, and T.Kita, "Increase in photocurrent by optical transitions via intermediate quantum states in direct-doped InAs/GaNAs strain-compensated quantum dot solar cell," *J. Appl. Phys.,* vol. 109, no. 024301, 2011.

[76] K.Sakamoto, Y.Kondo, K.Uchida, and K.Yamaguchi, "Quantum-dot density dependence of power conversion efficiency of intermediate-band solar cells," *J. Appl. Phys.,* vol. 112, no. 124515, 2012.

[77] I.Tobias, A.Luque, E.Antolin, P.Garcia-Linares, I.Ramiro, E.Henandez, and A.Marti, "Realistic performance prediction in nanostructured solar cells as a function of nanostructure dimensionality and density," *J. Appl. Phys.,* vol. 112, no. 124518, 2012.

[78] P.G.Linares, A.Marti, E.Antolin, I.Ramiro, E.Lopez, C.D.Farmer, C.R.Stanley, and A.Luque, "Low temperature concentrated light characterization applied to intermediate band solar cells," *IEEE J. Photovolt.,* vol. 3, no. 2, 2013.

[79] K.Nishikawa, Y.Takeda, T.Motohiro, D.Stao, J.Ota, N.Miyashita, and Y.Okada, "Extremely long carrier lifetime over 200 ns in GaAs wall-inserted type II InAs quantum dots," *Appl. Phys. Lett,* vol. 100, no. 113105, 2012.

[80] A.Luque, P.G.Linares, A.Mellor, V.Andreev, and A.Marti, "Some advantages of intermediate band solar cells based on type II quantum dots," *Appl. Phys. Lett.,* vol. 103, no. 123901, 2013.

[81] K.Susuki, R.A.Hogg, and Y.Arakawa, "Structural and optical properties of type II GaSb/GaAs self-assembled quantum dots grown by molecular beam epitaxy," *J. Appl. Phys.,* vol. 85, p. 8349, 1999.

[82] D.Alonso-Álvarez, B.Alén, J.M.García, and J.M.Ripalda, "Optical investigation of type II GaSb/GaAs self-assembled quantum dots," *Appl. Phys. Lett.,* vol. 91, p. 263103, 2007.

[83] P.D.Hodgson, R.J.Young, M.A.Kamarudin, P.J.Carrington, and A.Krier, "Blueshifts of the emission energy in type-II quantum dot and quantum ring nanostructures," *J. App. Phys.,* vol. 114, p. 073519, 2013.

[84] R.J.YYoung, E.P.Smakman, A.M.Sanchez, P.D.Hodgson, P.M.Koenraad, and M.Hayne, "Optical observation of single-carrier charging in type-II quantum ring ensembles," *App. Phys. Lett.,* vol. 100, p. 082104, 2012.

[85] M.P.Young, C.S.Woodhead, J.Roberts, Y.J.Noori, M.T.Noble, A.Krier, E P.Smakman, P.M.Koenraad, "Photoluminescence studies of individual and few GaSb/GaAs quantum rings," *AIP Advances,* vol. 4, p. 117127, 2014.

[86] I.Ramiro, E.Antolin, J.Hwang, A.Teran, A.J.Martin, P.G.Linares, J.Millunchick, J.Phillips, A.Marti, and A.Luque., "Three-bandgap absolute quantum efficiency in GaSb/GaAs quantum dot intermediate band solar cells," *IEEE J. Photovol.,* vol. 7, no. 2, 2017.

[87] I.Ramiro, J.Villa, C.Tablero, E.Antolin, A.Luque, A.Marti, J.Hwang, J.Phillips, A.J.Martin, and J. Millunchick, "Analysis of the intermediate band absorption properties of type-II GaSb/GaAs quantum-dot photovoltaics," *Phys. Rev. B,* vol. 96, p. 125422, 2017.

[88] A.J.Martin, J.Hwang, E.A.Marquis, E.Smakman, T.W.Saucer, G.V.Rodriguez, A.H.Hunter, V.Sih, P.M.Koenraad, J.D.Phillips, and J.Millunchick, "The disintegration of GaSb/GaAs nanostructures upon capping," *App. Phys. Lett.,* vol. 102, p. 113103, 2013.

[89] E.S.Zech, A.S.Chang, A.J.Martin, J.C.Canniff, Y.H.Lin, J.M.Millunchick, and R.S.Goldman, "Influence of GaAs surface termination on GaSb/GaAs quantum dot structure and band," *Appl. Phys. Lett.,* vol. 103, p. 082107, 2013.

[90] J.Hwang, K.Lee, A.Teran, S.Forrest, J.D.Phillips, A.J.Martin, and J.Millunchick, "Multiphoton sub-band-gap photoconductivity and critical transition temperature in type -II GaSb quantum-dot intermediate band solar cells," *Phys. Rev.:Appl.,* vol. 1, p. 051003, 2014.

[91] J.Hwang, A.J.Martin, K.Lee, S.Forrest, J.Millunchick, and J.Phillips, "Preserving Voltage and Long Wavelength Photoresponse in GaSb/GaAs Quantum Dot Solar Cells," in *IEEE 39th Photovoltaic Specialists Conference (PVSC)*, Tampa, FL, USA, 2013.

[92] P.J.Carrington, R.J.Young, P.D.Hodgson, A.M.Sanchez, and M.Hayne, "Long wavelength photoluminescence from stacked layers of high quality type-II GaSb/GaAs quantum rings," *Cryst. Growth Des.,* vol. 13, p. 1226−1230, 2013.

[93] M.C.Wagener, P.J.Carrington, J.R.Botha, and A.Krier , "Photocapacitance study of type-II GaSb/GaAs quantum ring solar cells," *J. Appl. Phys.,* vol. 115, no. 014302, 2015.

[94] H.Fujita, J.James, P.J.Carrington, A.R.J.Marshall, A.Krier, M.C.Wagener, and J.R.Botha, "Carrier extraction behaviour in type II GaSb/GaAs quantum ring solar cells," *Semicond. Sci. Technol.,* vol. 29, 2014.

[95] H.Fujita, P.J.Carrington, M.C.Wagener, J.R.Botha, A.R.J.Marshall, J.James, A.Krier, K.-H.Lee, and N.J.Ekins-Daukes, "Open-circuit voltage recovery in type II GaSb/GaAs quantum ring solar cells under high concentration," *Prog. Photov.: Res. Appl.,* vol. 23, pp. 1896-1900, 2015.

[96] Y.Shoji, R.Tamaki and Y.Okada, "Multi-stacked GaSb/GaAs type-II quantum nanostructures for application to intermediate band solar cells," *AIP Adv.,* vol. 7, no. 065305, 2017.

[97] M.C.Wagener, P.J.Carrington, J.R.Botha, and A.Krier, "Evaluation of the two-photon absorption characteristics of GaSb/GaAs quantum rings," *J. Appl. Phys.,* vol. 116, no. 044304, 2014.

[98] M.Geller, C.Kapteyn, L.Muller-Kirsch, R.Heitz, and D.Bimberg , "450 meV hole localization in GaSb/GaAs quantum dots," *Appl. Phys. Lett.,* vol. 82, pp. 2706-2708, 2003.

[99] Y.Shoji, K.Akimoto, and Y.Okada, "InGaAs/GaAsSb type-II quantum dots for intermediate band solar cell," *Proceedings of the 38th IEEE Photolt. Specialists Conf.,* vol. 2, pp. 1-4, 2012.

[100] C.M.A.Kapteyn, M.Lion, R.Heitz, D.Bimberg, P.N.Brunkov, B.V.Volovik, S.G.Konnikov, A.R.Kovsh and V.M.Ustinov, "Hole and electron emission from InAs quantum dots," *Appl. Phys. Lett.,* vol. 76, no. 1573, 2000.

[101] T.Müller, F.F.Schrey, G.Strasser and K.Unterrainer, "Ultrafast intraband spectroscopy of electron capture and relaxation in InAs/GaAs quantum dots," *Appl. Phys. Lett.,* vol. 83, no. 3572, 2003.

[102] O.Engström, M.Kaniewska, Y.Fu, J.Piscator, and M.Malmkvist, "Electron capture cross sections of InAs/GaAs quantum dots," *Appl. Phys. Lett.,* vol. 85, no. 2908, 2004.

[103] G.Wei, and S.R.Forrest, "Intermediate-band solar cells employing quantum dots embedded in an energy fence barrier," *Nano Letters,* vol. 7, no. 218, 2007.

[104] E.H.C.Parker, The technology and physics of molecular beam epitaxy, New York: Plenum Press, 1985.

[105] B. J. P. D. J.J. Harris, *Surf. Sci.,* vol. 103, 1981.

[106] V.P.LaBella, M.R.Krause, Z.Ding, and P.M.Thibado, "Arsenic-rich GaAs(0 0 1) surface structure," *Surface Science Reports,* vol. 60, p. 1–53, 2005.

[107] M.Ohring, The Material Science of Thin Films, New York: Academic Press, 1992.

[108] K.Oura, V.G.Lifshits, A.A.Saranin, A.V.Zotov, and M.Katayama, Surface Science: An Introduction., Berlin: Springer, 2003.

[109] A.Pimpinelli, and V.Jacques, Physics of Crystal Growth, Cambridge: Cambridge University Press, 1998.

[110] J.Venables, Introduction to Surface and Thin Film Processes, Cambridge: Cambridge University Press, 2000.

[111] E.P.Smakman, J.K.Garleff, R.J.Young, M.Hayne, P.Rambabu, and P.M.Koenraad, "GaSb/GaAs quantum dot formation and demolition studied by cross-sectional scanning tunneling microscopy," *App. Phys. Lett.,* vol. 100, no. 142116, 2012.

[112] J.Nelson, The physics of the solar cell, London (UK): Imperial College Press, 2003.

[113] Microchemicals GmbH, [Online]. Available: https://www.microchemicals.com/technical_information/photoresist_baking.pdf.

[114] CRC Handbook of Chemistry and Physics, 2008.

[115] A.R.Clawson, "Guide to references on III–V semiconductor chemical etching," *Materials Science and Engineering,* vol. 31, no. 1-438, 2001.

[116] V.Gottschalch, "Structural Etching of {001} and {110} Faces of Various AIIIBV Compounds," *Crystal Research and Technology,* vol. 14, no. 8, 1979.

[117] Bentham, "Bentham PVE300 photovoltaics," [Online]. Available: https://www.bentham.co.uk/products/systems/systems-search/pve300-photovoltaic-eqe-ipce-and-iqe-solution-16/.

[118] S.R.Jin, S.J.Sweeney, C.N.Ahmad, A.R.Adams, and B.N.Murdin, "Radiative and Auger recombination in 1.3μm InGaAsP and 1.5μm InGaAs quantum-well lasers measured under high pressure at low and room temperatures," *Appl. Phys. Lett.,* vol. 85, no. 3, p. 357, 2004.

[119] M.C.Wagener, D. Montesdeoca, Q. Lu, A.R.J.Marshall, A.Krier, J.R.Botha, P.J.Carrington, "Hole capture and emission dynamics of type-II GaSb/GaAs quantum ring solar cells," *Sol. Energ. Mat. Sol. Cell,* vol. 189, pp. 233-238, 2019.

[120] "Sim Windows," [Online]. Available: http://simwindows.wixsite.com/simwindows.

[121] "Ioffe," [Online]. Available: http://www.ioffe.ru/SVA/NSM/Semicond/GaAs/bandstr.html.

[122] M.Kaniewska, O.Engström, "Deep traps at GaAs/GaAs interface grown by MBE-interrruption growth technique," *Mat. Sci. Eng. C,* vol. 27, p. 1069, 2007.

[123] A.Marti, N.Lopez, E.Antolin, A.Luque, C.R.Stanley, C.D.Ffarmer, and P.Diaz, "Emitter degradation in quantum dot intermediate band solar cells," *App. Phys. Lett.,* vol. 90, no. 233510, 2007.

[124] M.C.Wagener, P.J.Carrington, J.R.Botha, A.Krier, "Simulation of the enhanced infrared photoresponse of type-II GaSb/GaAs quantum ring solar cells," *App. Phys. Lett.,* vol. 103, p. 063902, 2013.

[125] U.Rau, "Reciprocity relation between photovoltaic quantum efficiency and

electroluminescent emission of solar cells," *Phys. Rev. B,* vol. 76, no. 085303, 2007.

[126] W.N.Carr, "Characteristics of GaAs spontaneous infrares source with 40 percent efficiency," *IEEE Tr. Elect. Dev.,* vol. 12, no. 10, 1965.

[127] Y.D.Jang, T.J.Badcock, D.J.Mowbray, M.S.Skolnick, J.Park, D.Lee, H.Y.Liu, M.J.Steer, and M.Hopkinson , "Carrier lifetimes in type-II InAs quantum dots capped with a GaAsSb strain reducing layer," *App.Phys.Lett.,* vol. 92, no. 251905, 2008.

[128] S.H.Wei, A.Zunger, "Predicted band-gap pressure coefficients of all diamond and zinc-blende semiconductors: Chemical trends," *Phys. Rev. B,* vol. 60, no. 8, p. 5404, 1991.

[129] W.Paul, High Pressure in Semiconductors Physics II, Academic Press, 1998.

[130] R.Tamaki, Y. Shoji, and Y. Okada, "Efficient Two-Step Photon Absoprtion in Type-II GaSb Quantum Dot Soalr Cells," Colorado (USA), 2017.

[131] T.H.Loeber, J.Richter, J.Strassner, C.Heisel, C.Kimmle, H.Fouckhardt , "Efficient Ga(As)Sb quantum dot emission in AlGaAs by GaAs intermediate layer," vol. 8634, no. 86340, 2013.

[132] A.Kechiantz, A.Afanasev, J.-L.Lazzari, "Enhancement of GaAs solar cell efficiency by type-II GaSb quantum dots located outside of the depletion region," vol. 3, 2013.

[133] A.Pusch, M.Yoshida, N.P.Hylton, A.Mellor, C.C.Phillips, O.Hess and N.J. Ekins-Daukes, "Limiting efficiencies for intermediate band solar," *Prog. Photovolt: Res. Appl.,* 2016.

[134] L.Morresi, Basics of Molecular Beam Epitaxy (MBE) technique, Bentham Science Publishers, 2013.

[135] C. Kittel, Introduction to Solid State Physics, Berkeley: John Wiley & Sons, 2005.

[136] C.G.van der Walle, and J.Neugebauer, "Universal alignment of hydrogen levels in semiconductors, insulators and solutions," *Nature,* vol. 423, no. 626, 2003.

[137] P.J.Carrington, R.J.Young, P.D.Hodgson, A.M.Sanchez, M.Hayne, and A.Krier, "Long-Wavelength Photolumminescence from Stacked Layers of High-Quality Type-II GaSb/GaAs Quantum Rings," *Crys. Growth & Design,* vol. 13, pp. 1226-1230, 2013.

[138] G.Conibeer, "Third-generation photovoltaics," *Materialstoday,* vol. 10, no. 11, 2007.

[139] Z.Zheng, H.Ji, P.Yu, and Z.Wang, "Recent Progress Towards Quantum Dot Solar Cells with Enhanced Optical Absorption," *Nanoscale Res. Lett.,* vol. 11, no. 266, 2016.